Correlations of Structure and Magnetism in Perovskite Thin films

Ph.D. Thesis

By

FOZIA AZIZ

DISCIPLINE OF PHYSICS

INDIAN INSTITUTE OF TECHNOLOGY INDORE

MAY, 2014

Correlations of Structure and Magnetism in Perovskite Thin films

A THESIS

Submitted in partial fulfillment of the
requirements for the award of the degree
of
DOCTOR OF PHILOSOPHY

by
FOZIA AZIZ

DISCIPLINE OF PHYSICS
INDIAN INSTITUTE OF TECHNOLOGY INDORE
MAY, 2014

INDIAN INSTITUTE OF TECHNOLOGY INDORE

CANDIDATE'S DECLARATION

I hereby certify that the work which is being presented in the thesis entitled **"Correlations of Structure and Magnetism in Perovskite Thin films"** in the partial fulfillment of the requirements for the award of the degree of **DOCTOR OF PHILOSOPHY** and submitted in the **DISCIPLINE OF PHYSICS, Indian Institute of Technology Indore**, is an authentic record of my own work carried out during the time period from March 2010 to May 2014 under the supervision of Dr. Krushna R. Mavani, Associate Professor, Discipline of Physics, IIT Indore

The matter presented in this thesis has not been submitted by me for the award of any other degree of this or any other institute.

Signature of the student with date
(FOZIA AZIZ)

This is to certify that the above statement made by the candidate is correct to the best of my/our knowledge.

Signature of Thesis Supervisor with date
(Dr. KRUSHNA R. MAVANI)

Ms. FOZIA AZIZ has successfully given his/her Ph.D. Oral Examination held on _______________________________________.

Signature(s) of Thesis Supervisor(s)
Date:

Convener, DPGC
Date:

Signature of PSPC Member #1
Date:

Signature of PSPC Member #1
Date:

Signature of External Examiner
Date:

Dedicated to Ammi and Papa....

ACKNOWLEDGEMENT

"For, each soul enters with a mission……we all have a mission to perform"- Edgar Cayce

With blend of gratitude, pleasure and great satisfaction I convey my indebtedness to all those who have directly or indirectly contributed to the successful completion of my thesis.

First and foremost I thank God almighty for the blessings, wisdom and perseverance that he has bestowed upon me during my research work, and indeed, throughout my life.

I express my deepest sense of gratitude to my supervisor Dr. Krushna R. Mavani for all the encouragement, guidance and constructive criticism throughout my work. I am extremely thankful to our collaborator Dr. D. S. Rana, IISER Bhopal, who supported me during the tough times when we had no established lab at IIT Indore for sample synthesis and for providing all the measurement facilities, making it possible to complete my work in time.

I am highly grateful to Director Sir, Prof. Pradeep Mathur for his persistent encouragement and valuable suggestions. I thank Prof. P. N. Puntambekar for his blessings, perpetual motivation and moral support throughout my work. I thank my PSPC members Dr. Amod Umarikar and Dr. Ankhi Roy for their insightful comments during each of my seminars.

I convey my sincere thanks to my labmate Mahesh Chandra for all the encouragement, critical comments and support during my entire tenure at IIT Indore.

I thank Dr. D. M. Phase and Dr. Ramjanay Choudhary for all the knowledge that I gained from them while working at IUC-DAE Indore. I am thankful to Dr. Mukul Gupta for providing XRD measurements so promptly.

I am thankful to Parul Pandey and Rakesh Rana for all their help and support during my stay at IISER Bhopal. I thank Shivendra Tripathi, Manoj Prajapat and Chetanya Prakash for their timely help in making all the measurements. I thank Kinny Pandey for his help in AFM measurements.

I sincerely wish to express my gratefulness to all the faculty members of the department who have extended their cooperation at all times and have contributed in their own way.

Last but not the least, my heartfelt thanks to my parents, my sisters Sufia, Rafia, my friends Gireesh, Shambhavi and Piki, Asha aunty and Narmada aunty, whose unconditional love and prayers have sustained me thus far.

Fozia Aziz

LIST OF PUBLICATIONS

- "Surface Morphology, Ferromagnetic Domains and Magnetic Anisotropy in $BaFeO_{3-\delta}$ Thin Films: Correlated Structure and Magnetism" **Fozia Aziz**, Parul Pandey, Mahesh Chandra, Amit Khare, D. S. Rana and K. R. Mavani, *Journal of Magnetism and Magnetic Materials*, **356,** 98–102 (2014)
- "Effects of Ti-doping on Evolution of Coexisting Magnetic Phases in $BaFeO_{3-\delta}$ Thin Films at Room Temperature", **Fozia Aziz**, *Journal of Applied Physics,* 115, 223907-1-7 (2014).
- "Structural Transformations, Magnetic Correlations and Effect of Strain on Ce-doped $Pr_{0.5}Ca_{0.5}MnO_3$ thin films", **Fozia Aziz** *et. al*. Journal paper under preparation.
- "Effect of Ion Irradiation on the Structural and the Magnetic Properties of $BaFeO_{3-\delta}$ Thin Films", **Fozia Aziz** *et. al*. Journal paper under preparation.
- "Effect of Interfaces and Strain on $BaFeO_{3-\delta}$ /$BaTiO_3$ Bilayers and Composites ", **Fozia Aziz** *et. al*. Journal paper under preparation

Contributory papers as coauthor:

- "Contrasting Effects of Doping on Insulating and Metallic States of $NdNi_{1-x}Mn_xO_3$ Thin Films", Mahesh Chandra, **Fozia Aziz**, Shivendra Tripathi, Rakesh Rana, D. S. Rana and K. R. Mavani , *Journal of Applied Physics* **115**, 93701 (2014)
- "Structure-mediated competing effects of Mn-doping and epitaxial strain on electrical transport of $NdNi_{1-x}Mn_xO_3$ ($0 \leq x \leq 0.10$) thin films", Mahesh Chandra, Rakesh Rana, **Fozia Aziz**, Amit Khare, D. S. Rana and K. R. Mavani, *Journal of Physics D: Applied Physics* **46**, 415305 (2013)
- "Charge Transport in $NdNiO_3$ Thin Films: Effects of Mn-doping versus Tensile Strain", Mahesh Chandra, **Fozia Aziz**, Rakesh Rana, Ravikiran Late, D. S. Rana, K. R. Mavani, *AIP Conf. Proc.* (2013)

- “Contrasting effects of compressive and tensile strain and doping-induced opening of charge-transfer gap in $NdNi_{0.9}Mn_{0.1}O_3$ thin films” Mahesh Chandra, Amit Khare, **Fozia Aziz**, Rakesh Rana, D. S. Rana et al., *AIP Conf. Proc.* **1512**, 986, (2012)
- “Sharp metamagnetic and correlated electronic transitions in manganites: A systematic effect of cation disorder”, K. R. Mavani, **Fozia Aziz**, Mahesh Chandra, and P. L. Paulose, *AIP Conf. Proc.* **1447**, 141, (2011)

Conferences/Seminars attended:

- Oral presentation on “Oxygen-Annealing-induced Magnetic Anisotropy and Enhancement in Magnetization of $BaFe_{0.9}Ti_{0.1}O_{3-x}$ Thin Film”, **Fozia Aziz**, Amit Khare, Mahesh Chandra, Parul Pandey, D. S. Rana, K. R. Mavani, in the7th *International conference on materials for Advanced Technology* (ICMAT 2013), held at Suntec Singapore.
- Poster presentation on “Enhanced magnetization and magnetic anisotropy of oxygen annealed BaFeO3-δ thin film”, Fozia Aziz, Parul Pandey, Mahesh Chandra, Amit Khare, D. S. Rana and K. R. Mavani, International conference on Magnetic materials and Applications, MagMa 2013, held at IIT Guwahati.

TABLE OF CONTENTS

Chapter 4: Interface Influenced Magnetism in $BaFeO_{3-\delta}$ /$BaTiO_3$ Multilayers and the Effects of Swift Ion Irradiation on structure and Magnetism of $BaFeO_{3-\delta}$ Thin Films

Chapter 5: Structural and Magnetic Correlations in Tensile and

Compressive Strained Epitaxial Thin Films of $\mathbf{Pr_{0.5-\mathit{x}}Ce_{\mathit{x}}Ca_{0.5}MnO_3}$ Manganites

LIST OF FIGURES **Page No.**

LIST OF TABLES

Page No.

Chapter 1

Introduction and Motivation

1.1 Introduction

During last 2-3 decades, a plethora of studies have been performed on the complex oxides, filled with interesting physics, existing in diverse crystalline structures and finding a variety of applications. Manipulating the structure or chemistry of oxides can give rise to novel properties, making it possible to engineer new functional materials. Particularly, transition metal oxides (TMO), due to the ability of transition elements to exist in different valence states with different charge, spin and orbital degrees of freedom, offer a variety of electrical and magnetic phases. TMOs exhibit a wide range of physical phenomena like, ferroelectricity, ferromagnetism, ferrimagnetism, high temperature superconductivity, piezoelectricity and multiferroicity (coexisted ferroelectricity and magnetism) [1]. In addition, these materials show a variety of electrical behaviors, which can be insulating (*e.g.* $BaTiO_3$), semiconducting (*e.g.* $SmNiO_3$) or metallic (*e.g.* $SrRuO_3$).

TMOs provide possibilities for designing multifunctional behavior by combining magnetic and ferroelectric properties or by combining magnetic and piezoelectric properties, forming a family of compounds called multiferroics. Multiferroics are materials which possess more than one ferroic ordering: ferromagnetism, ferroelectricity, ferroelasticity and/or ferrotroidicity. Multiferroics with coexisting electric and magnetic coupling are called as magnetoelectric multiferroics. The scientific community is working to tap the potential of these materials for fabrication of a new type of memory device wherein data can be written electrically and read magnetically, giving much higher processing speed as compared to conventional memories. Using an electric field instead of a magnetic one in the writing procedure will allow a reduction in power consumption, increase in speed, and miniaturization of memory devices. However, magnetoelectric multiferroics are rare to find; the ones known presently are $BiFeO_3$ and $YMnO_3$ which are antiferromagnetic or weakly ferromagnetic [2,3]. Such multiferroic materials hold potential for spintronics applications.

Magnetic oxides, a subclass of complex oxides, have been the most applicable oxides for decades [4]. As the associated physics became known with time, plenty of applications of magnetic materials came into existence like permanent magnets, cores of inductors and transformers, electromagnets in electric motors, discs-tapes-cassettes for information storage, microwave devices, antennas, and refrigeration magnets. Magnetic oxides form a vital part of modern computer technology. With the invention and development of thin film technology, the size of computers has become smaller and processing speed has become faster. The discoveries of phenomena like colossal magnetoresistance in manganese oxides and high temperature superconductivity in copper oxides have allured the interest of scientists all over the world to magnetic oxides. The past half-century has seen exponential growth in research on magnetic oxide based devices such as nonvolatile magnetic random access memories, magnetic tunnel junctions and magnetic field sensors.

As compared to semiconductors and metals, oxides are difficult to fabricate [5]. Owing to the lack of proper synthesis techniques they did not draw much attention of researchers for years. 1980s saw the boom in thin film fabrication technique when high transition temperature (T_c) superconductors were grown as thin films. Certain oxides which cannot be formed in bulk form could be stabilized in the form of thin films. Since then, there has been a tremendous increase in research on complex oxides and they now constitute an integral part of various facets of present technology. For example, high dielectric constant oxides find application in CMOS technology; ferroelectric oxides are used for a wide range of applications such as sensors and capacitors, and recently oxides like lead zirconate titanate $PbZr_{1-x}Ti_xO_3$ (PZT) and barium strontium titanate

$Ba_xSr_{1-x}TiO_3$ (BST) have been investigated due to their applicability in non-volatile ferroelectric random access memories which will be faster and have longer endurance [6].

For device based applications, the oxides must show Curie temperature well above room temperature. This quest for room temperature ferromagnetic or multiferroic materials has lead to intensive studies on materials like dilute magnetic oxides, ferrites, perovskites, spinels and mixed-valence manganites. Researchers have tried various ways to tailor the magnetic properties by impacting the structure of material via epitaxial strain or by combining them in the form of multilayers and superlattices. There have been numerous reports recently where these processes are found to induce or mould the magnetic properties of materials.

As Chapter 1 proceeds, the background or basis will be formed, which would be required for understanding the results of our study. The core of this thesis is to explore correlation of magnetism with structure in different oxides. Therefore, we will start with the description of basic structure of the oxides under study. Later, we will describe various magnetic phenomenon involved followed by other basic essential for understanding the work presented ahead.

1.2 Perovskite Oxides

Perovskite oxides form one of the most intriguing and probably the best studied class of transition metal oxides. Perovskite originally is a mineral $CaTiO_3$, discovered by Gustav Rose in 1839 and named after Russian mineralogist Count Lev Aleksevich von Perovski. They have several features of fundamental and technological interest. The greatest advantage of this class of oxides lies in the ease with which they form compatible heterostructures with compounds of the same or different class. This gives rise to multitude of novel physical properties which may not be present in the parent compounds.

I. Crystal Structure

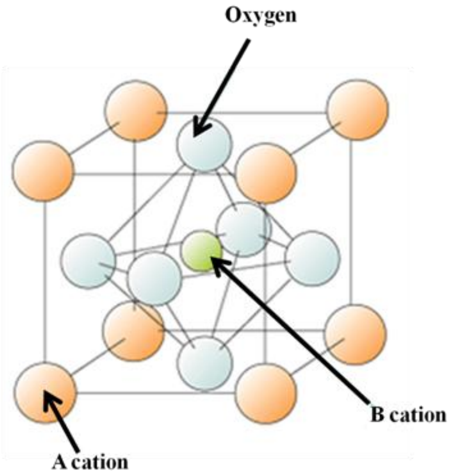

Figure 1.1: Perovskite oxide crystal structure.

Perovskite oxides have a stoichiometric formula of ABO_3 where, ‘A’ stands for alkali, alkaline earth or rare earth metal ion and ‘B’ stands for a transition metal ion. The oxidation states of A-cations can be +2 or +3 and of B-cation can be +4 or +3 forming two categories of compounds with formula $A^{+2}B^{+4}O_3$ or $A^{+3}B^{+3}O_3$ and sometimes a mixed valance state of the type $A^{+2/+3}B^{+4/+3}O_3$. The ideal perovskite structure is cubic with eight corner-centered BO_6 octahedra and A-cation at the center with 12-fold coordination with oxygen ions (Figure 1.1). However, various members of this family have distorted structure, deviating from ideal cubic structure to orthorhombic, rhombohedral or hexagonal. A constant, *t*, known as the tolerance factor [7] defined as,

$$t = \frac{r_A + r_O}{\sqrt{2}(r_B + r_O)} \qquad (1)$$

r_A – radius of A-cation; r_B – radius of B-cation; r_O- radius of Oxygen ion. ‘t’ is a measure of degree of distortion of a perovskite from ideal cubic structure. A perovskite oxide will have cubic symmetry if $0.9 < t < 1$, orthorhombic symmetry if $0.75 < t < 0.96$ and will exhibit hexagonal symmetry if $1.0 < t < 1.13$. An ideal cubic structure will be acquired for $t = 1$ with B-O-B bond angle equal to 180°. To adjust $t < 1$, BO_6 octahedra undergoes rotation resulting in change of B-O-B bond angle and B-O bond length. B-cation exchange interactions occur via oxygen, therefore any change in B-O-B bond angle would alter these interactions affecting the physical properties of perovskite oxides.

The octahedral rotations arise due to following three main factors:

1. Cation Size Effect

$SrTiO_3$ has ideal cubic structure with $t = 1$, $r_A = 1.44$ Å; $r_B = 0.605$ Å; $r_O = 1.40$ Å. When the size of A-site cation is smaller than the above value, t will be less than 1. Thus, the BO_6 octahedra will tilt to fill the space resulting in orthorhombic symmetry, *e.g.* in $GdFeO_3$ ($r_A = 1.107$ Å and $r_B = 0.78$ Å). As A-site cation decreases in size the symmetry of the system will also reduce. For A-cations with size larger than the above value $t > 1$ leads to close packed structures stacked in hexagonal symmetry rather than cubic. Manipulating A-site cation radius can lead to changes in the physical properties of the perovskite oxides as it has been observed in A-site doped manganites $R_xA_{1-x}MnO3$ [R = La^{3+}, Pr^{3+}, Sm^{3+}, Pm^{3+} and Nd^{3+} and A = Ca, Sr and Ba]. From this point of view, few parameters which need to be defined are as follows:

One parameter is the average A-site cationic radius $\langle r_A \rangle$, as given by the formula:

$$\langle r_A \rangle = \sum_i x_i r_i \qquad (2)$$

where, r_i is the ionic radii of i^{th} cation and x_i is the fractional occupancies of the different i cations. Thus, any change in $\langle r_A \rangle$ would cause a bending of B-O-B bond angle thereby resulting in tilting of BO_6 octahedra. $\langle r_A \rangle$ has a linear relationship with T_C (Curie Temperature) while both $\langle r_A \rangle$ and T_C exhibit inverse correlation with magnetoresistance (MR) (to be defined later).

Another parameter is ion size variance (or cation disorder) at A-site, which gives a measure of the ionic mismatch. This arises due to doping of divalent alkali and alkaline earth cations or trivalent rare earth cations at the A-site. It is defined as follows:

$$\sigma_A^2 = \sum_i x_i r_i^2 - \langle r_A \rangle^2$$

The variance in size is ascribed to the displacements of the oxygen atoms due to the A-site cation disorder, as shown by the simple model of manganites in Figure 1.2. The structural disorder which occurs due to change in size of A-site cation leads to local displacement of oxygen. This results in fluctuations of B-O-B bond angle and alterations in B-O bond length leading to carrier localization, thereby affecting the electrical transport and magnetic properties [8].

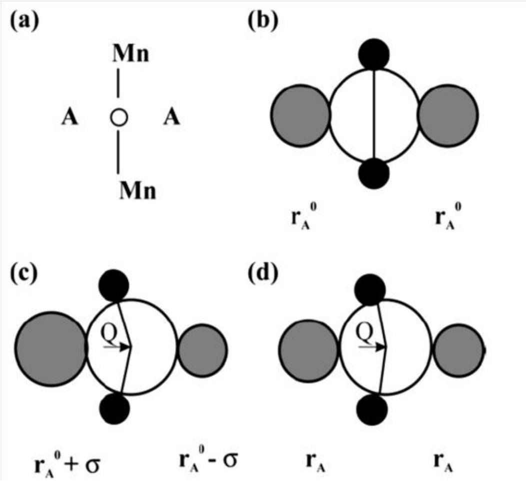

Figure 1.2: Model for local oxygen displacements in $AMnO_3$ perovskites. A fragment of ideal cubic structure with A cations of radii r_A^0 is shown schematically in (a) and as spherical ions in (b) Cation size disorder in (c) gives rise to random oxygen displacements $Q = \sigma$ and a reduction in the A site radius in (d) leads to ordered oxygen displacements $Q = r_A^0 - r_A$. [from reference 9]

2. Changing Chemical Composition from Ideal ABO_3

Certain compounds of this stoichiometry can have oxygen deficiency leading to variation in stoichiometry to $ABO_{3-\delta}$ ($0 < \delta < 0.5$). The oxygen vacancies are found to have critical impact on the physical properties of oxides. For examples, oxygen vacancies in $Eu_{0.5}Ba_{0.5}TiO_{3-\delta}$ induce antiferromagnetic to ferromagnetic transitions [10], an increase in oxygen vacancies lead to disappearance of six-wedge ferroelectric domain walls in $YMnO_3$ by changing the *4p-2p* hybridization and structural distortion [11]. Also, ordering of oxygen vacancies can to give rise to change in the physical properties of compound. A well known example of it is $SrFeO_{3-\delta}$, where oxygen vacancy ordering gives rise to spin and charge ordering leading to different magnetic structures within the system [12].

3. Jahn-Teller (JT) Distortion

According to the crystal field theory, in octahedral symmetry the 5 degenerate d levels split into three t_{2g} and two e_g orbitals.

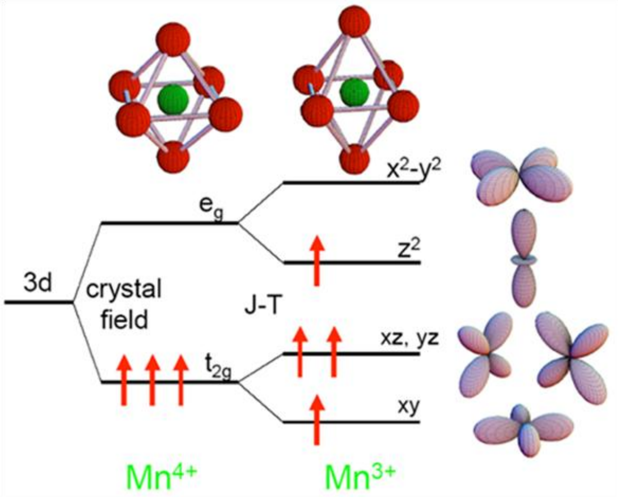

Figure 1.3: Energy level splitting of the 3d-electron orbitals in an octahedral crystal field (Mn^{4+}) and due to the Jahn-Teller effect (Mn^{3+}). [from reference 14]

In molecules with octahedral symmetry, if the degenerate orbitals are occupied asymmetrically, then octahedron distorts to remove this degeneracy. This process is known as Jahn-Teller distortion [13]. Now asymmetry is associated with higher energy and a system always tends to occupy minimum energy or eliminate this extra energy. To understand how asymmetry arises let us look at the following example: in octahedral symmetry d^1 configuration is asymmetric because the lone electron can reside in any one of the d_{xy}, d_{yz} and d_{zx} orbitals. On the other hand d^3 configuration is symmetric and non-degenerate because according to the Hund's rule, there is only one way in which these three electrons can be distributed in three t_{2g} orbitals. Electronic degeneracy in octahedral environment is not found for d^3, d^8, d^{10}, high spin d^5 and low spin d^6 configurations, whereas, considerable distortions usually take place in high spin d^4, low spin d^7 and d^9 configurations in the octahedral environment. Jahn-Teller distortion is significant for asymmetrically occupied e_g orbitals than for t_{2g} orbitals. Asymmetrically occupied e_g orbitals lie along the ligand direction and hence increase in energy is considerably more, while t_{2g} orbitals lie away from the ligand direction having lower energy gain. To remove the degeneracy of orbitals, th symmetry of a molecule is lowered either by elongation or contraction of octahedra along the Z-axis.

There are three types of JT effects [15] which can occur in oxides:

i) Static Jahn-Teller effect – When the distortion occurring in a molecule is fixed along a particular axis, then it is termed as static JT effect. The distortion is strong and permanent, due to which the molecule has a tendency to stay in one particular shape under all conditions (*i.e.* with respect to temperature, pressure, *etc.*)

ii) Dynamic Jahn-Teller effect – In a molecule when the distortions fluctuate from one axis to another then they are termed dynamic JT effect. These fluctuations are so random and fast that they cannot be observed spectroscopically. The molecule thus appears to be undistorted.

iii) Cooperative Jahn-Teller effect- In certain materials, complexes can undergo a distortion collectively throughout the crystal. This is known as a cooperative JT distortion. Spinels (AB_2O_4) with octahedrally coordinated B-site favor cooperative distortion resulting in the phase transformation from one crystalline structure to another [16].

1.3 Magnetism

Electrons in an atom revolve in an orbit and rotate about their axis. A charge in motion is associated with a magnetic moment. Thus, an electron possesses orbital and spin magnetic moments. The fundamental unit of magnetic moment is the Bohr magneton [17] defined as:

$$\mu_B = \frac{e\hbar}{2m_e}$$

The net magnetic moment of an ion or atom is the vector sum of moment due to orbital and spin motion. There are a variety of types of magnetism existent in different materials like: diamagnetism, paramagnetism, ferromagnetism, antiferromagnetism, ferrimagnetism, magnetic glasses and metamagnetism. Diamagnetism is inherently present in all the materials. This sections describes in brief some of these types of magnetism which take place in the materials under study.

1.3.1 Ferromagnetism

The property of a material to exhibit spontaneous magnetism *i.e.* possesses a net magnetic moment, even in absence of external magnetic field is called as ferromagnetism. Origin of ferromagnetism is due to exchange interactions, a quantum mechanical effect between the quantized spins of electrons governed by *Pauli's exclusion principle*. In an applied magnetic field $\vec{B}$, the Hamiltonian for a ferromagnet is given by [15]:

$$\hat{H} = -\sum_{ij} J_{ij}\boldsymbol{S_i} \cdot \boldsymbol{S_j} + g\mu_B \sum_{j} \boldsymbol{S_j} \cdot \boldsymbol{B}$$

J_{ij} is the exchange integral between the spins $\boldsymbol{S_i}$ and $\boldsymbol{S_j}$ and g is the Landé factor. Interaction between the spins are ferromagnetic when $J_{ij} > 0$.

Though ferromagnetic materials possess spontaneous magnetization yet these materials as a whole often exist in unmagnetized states. This is due to the fact that a ferromagnetic material consists of small regions, which possess local magnetic moments. They are called domains. Each domain in a ferromagnet is like a small magnet individually but randomly oriented thus adding up to no net magnetization. In presence of high enough magnetic field, each of these domains gets aligned in the direction of applied magnetic field and the system acquires a net magnetization called saturation magnetization (M_s).

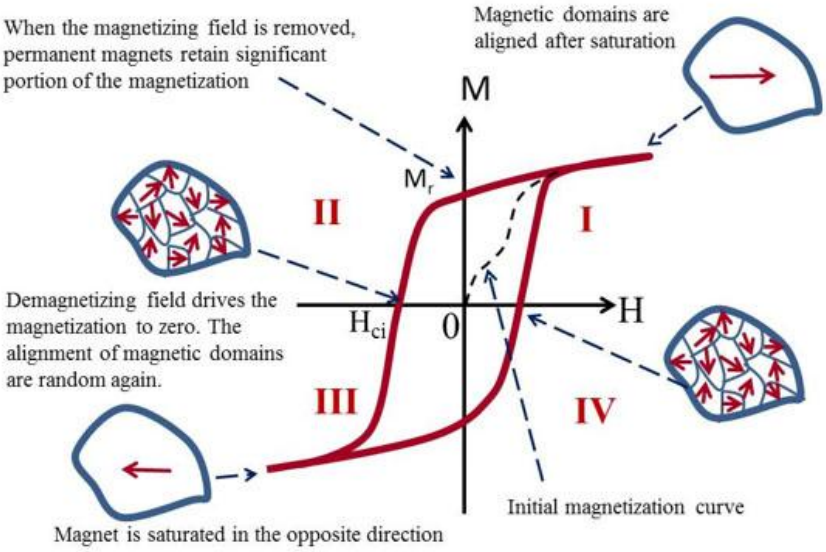

Figure 1.4: Typical hysteresis loop and magnetic domain morphology of ferromagnetic materials. [source of figure: reference 18]

Once the system acquires M_s the magnetization remains nearly constant with any further increase in magnetic field. When the field is removed magnetization of the material does not reduce back to zero but has some finite value known as remanence. To reduce the magnetization to zero a field in the opposite direction must be applied. The amount of field required to reduce the magnetization back to zero is called as coercive field (H_c). If the field applied in opposite direction is increased further, then the material again acquires saturation magnetization but in opposite direction. When the same process is further continued the ferromagnet returns to the original M_s state thus forming a closed loop called as hysteresis loop (Figure 1.4).

Ferromagnetic Domains

In ferromagnetic material there exist small regions in which all the magnetic dipoles are aligned in the same direction, these are called as ferromagnetic domains [19]. There can now be a question: *why do domains form in a ferromagnetic material?* The answer is to minimize the total internal energy of system. The magnetic exchange energy of the material should be minimal if it existed in form of a single domain with large magnetic field around it. This will result in large magnetostatic energy being stored in the system, to minimize it the material breaks into smaller domains. Other contributors to the total magnetic energy of the system are magnetocrystalline and magnetostrictive energies which also influence the size and shape of domains. A ferromagnetic material therefore splits into domains of smaller sizes to minimize the total magnetic energy of the entire system

Ferromagnetic domains can be observed using different techniques like:

i. Bitter's method

ii. Magneto-optic techniques

iii. Magnetic Force Microscopy

We have used magnetic force microscopy for observing magnetic domain on the surface of our films. This technique is described in Chapter 2.

Soft ferromagnetic materials

The ferromagnetic materials which have low values of coercivity (H_c) and require a very small field to acquire saturation magnetization are called as soft ferromagnet. They have very low values of remanent magnetization (M_r) almost approaching zero value around zero magnetic field producing a narrow hysteresis loop.

Hard ferromagnetic materials

The ferromagnetic materials which have large coercivity and require higher fields to attain saturation magnetization are known as hard ferromagnets. The hysteresis loop is wider for these materials. The remanence of hard ferromagnet is generally around 50% of the M_s for randomly oriented samples and the ratio $M_r/M_s \sim 1$ for perfectly oriented samples. In such a case the loop would almost look like a square and is therefore called as square loop.

Exchange springs magnets

The maximum energy product $(BH)_{max}$ gives the figure of merit of permanent magnets. This product increases by increase in coercivity (H_c) and saturation magnetization (M_s). For high coercivity materials the energy product is limited by M_s and is given by $(BH)_{max} \leq (2\pi M_s)^2$. To overcome this limitation one proposed approach was nanocomposites of exchange coupled soft and hard magnetic phases. Such magnets are known as exchange spring magnets. The hard magnetic component would provide high anisotropy and high coercivity, and the soft component would provide high saturation magnetization. Due to this they prove to be good candidates for permanent hard magnets.

Antiferromagnetism

An antiferromagnet is the material in which the adjacent magnetic moments are aligned antiparallel to each other. It can be viewed as a combination of two interpenetrating magnetic sublattice which are spontaneously magnetized in opposite direction so that there is no net magnetization of the material. The behavior of an antiferromagnet is similar to that of a paramagnet at higher fields. The antiferromagnets are characterized by Neel temperature (T_N), which is the temperature below which the spins of the system order antiferromagnetically. There are various types of antiferromagnetisms as shown in figure.

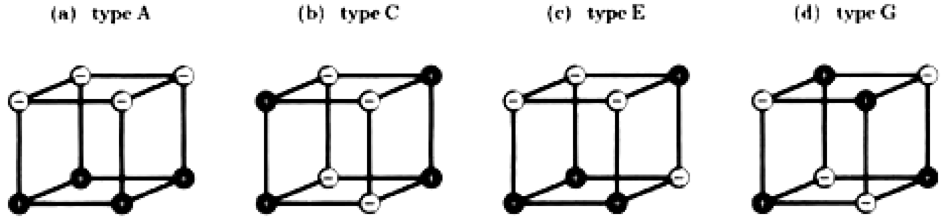

Figure 1.5: Different types of antiferromagnec states.'+' in black ball indicate 'spin up' and '-' in white balls indicate 'spin down'in ions [from reference 15].

Weak Ferromagnetism

An ideal antiferromagnet will have zero spontaneous magnetization because the two sublattices cancel the magnetic contribution. However, deviations from this ideal behavior can exist. In some antiferromagnetic materials spins of the two sublattices may not be perfectly antiparallel but are canted or tilted by certain angle with respect to each other giving rise to small ferromagnetic component in the material. This is termed as weak ferromagnetism or parasitic ferromagnetism or spin canted antiferromagnetism. Magnetization (σ) of such a material is given by [20]:

$$\sigma = \sigma_0 + \chi H$$

where, $\boldsymbol{\sigma_0}$ is the spontaneous magnetization of the ferromagnetic part and $\boldsymbol{\chi}$ is the antiferromagnetic susceptibility. The interactions which give rise to weak ferromagnetism are called as Dzyaloshinsky-Moriya interaction and are expressed by the following equation [20]:

$$W_D = D \cdot (S_1 \times S_2)$$

S_1 and S_2 are the canted spins and D is a vector coefficient which vanishes when the system has point inversion symmetry between two magnetic ions. When D is non-zero it will lie parallel or perpendicular to the spins forcing them to cant at certain angle with respect to each other giving rise to net magnetic moment.

Weak ferromagnetism is found to originate due to different reasons. Rare earth orthoferrites $RFeO_3$ (R = Sm-Lu) are all found to show parasitic ferromagnetism, which was proposed to be originating due to B-cation movement from uniaxial direction [21]; Louis Néel showed in his paper that weak ferromagnetism could arise due to defects of stoichiometry or crystallization [22]; $BiFeO_3$ shows weak ferromagnetism at room temperature due to spin canting [2]; cation disorder induced octahedral distortion is found to induce weak ferromagnetism in otherwise paramagnetic $CaRuO_3$ [23]. $BaFeO_3$ shows weak ferromagnetism at room temperature which can be manipulated by chemical substitution or by changing the oxygen stoichiometry [24, 25].

Metamagnetism

In antiferromagnetic materials, when the magnetic ground state becomes metastable and shows a transition to ferromagnetic state is called a metamagnetic transition. Sometimes, due to inhomogenity, when antiferromagnets are placed in high magnetic field, clusters are found to orient spontaneously in the field direction giving rise to large increase in magnetism, followed by a metamagnetic transition. Many perovskite oxides with Mn at the B-site are found to show metamagnetic transitions.

Magnetoresistance

The change in resistance of a material on application of magnetic field is called as Magnetoresistance. It arises due to field dependence of the mean free path of conduction electrons. It is defined as the ratio of change in resistance of material on application of magnetic field as compared to the resistance at zero field,

$$MR = \frac{R_H - R_0}{R_0}$$

Where, R_H – resistance at magnetic field H and R_0 – resistance at zero magnetic field

If, $R_H > R_0$ the material is said to have positive Magnetoresistance

$R_H < R_0$ the material is said to have negative Magnetoresistance

Magnetoresistance is a phenomenon widely studied now owing to its commercial applicability in magnetic sensor and read heads of magnetic memory. Colossal magnetoresistance (CMR) is a huge (orders of magnitude) change of electrical resistivity of a material under an applied magnetic field, which is observed mostly in manganese-based perovskite oxides near the Curie temperature in high magnetic fields. Due to the CMR effect these oxides are considered as promising candidates for technological applications in magnetic devices.

Magnetocrystalline Anisotropy:

In ferromagnetic crystals magnetization has a tendency to acquire certain preferred crystallographic directions. These preferred directions are called as easy axes of magnetization. It is easier to magnetize a demagnetized ferromagnetic material along these axes as it requires lower field and hence lower energy to attain saturation magnetization. The energy required to magnetize material along hard axes

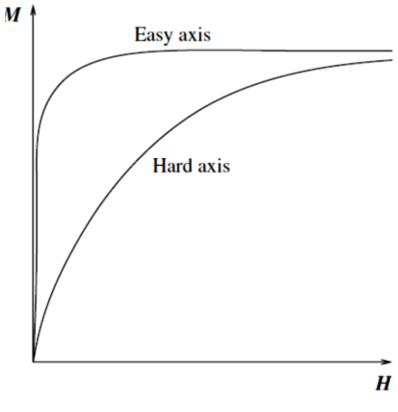

Figure 1.6: Magnetocrystalline Anisotropy.

is much larger. Figure 1.6 shows the schematic of how the curves of ferromagnetic crystal would look like for easy and hard axes. Different materials have different easy and hard axes. For *e.g.* body centered cubic Fe crystal has (100) crystallographic directions as the easy axes and (111) directions as the hard axes [17].

Exchange interactions

When the two magnetic ions are present close to each other the interaction between them is through direct overlap of spin orbitals. However, in oxides and other ionic compounds for the non-neighbouring magnetic ions since the orbitals lie far away from each other the interactions between them are mediated via non-magnetic anion. These are called as indirect exchange interactions. There are two types of indirect exchange interactions which are described below:

Super-exchange Interactions

In transition metal oxides there is no direct overlap of $3d$-$3d$ orbitals, however, they interact via hybridization with oxygen $2p$ orbitals. Thus, oxygen ion mediates the interaction between the two magnetic ions. Figure 1.7 shows a typical superexchange bond. For half filled or singly occupied d-orbitals e.g. Fe^{3+} or Mn^{2+} the configuration (b) is lower in energy as compared to configuration (a) as both the electrons in oxygen 2p orbitals can then spread into unoccupied d-orbitals. Superexchange interactions do not involve actual movement of electrons. When the M-O-M bond angle is between 120˚-180˚ the exchange interactions are strong and antiferromagnetic because the 3d orbital lobes are having larger overlap. When M-O-M bond angle is 90˚ the exchange is ferromagnetic and weak.

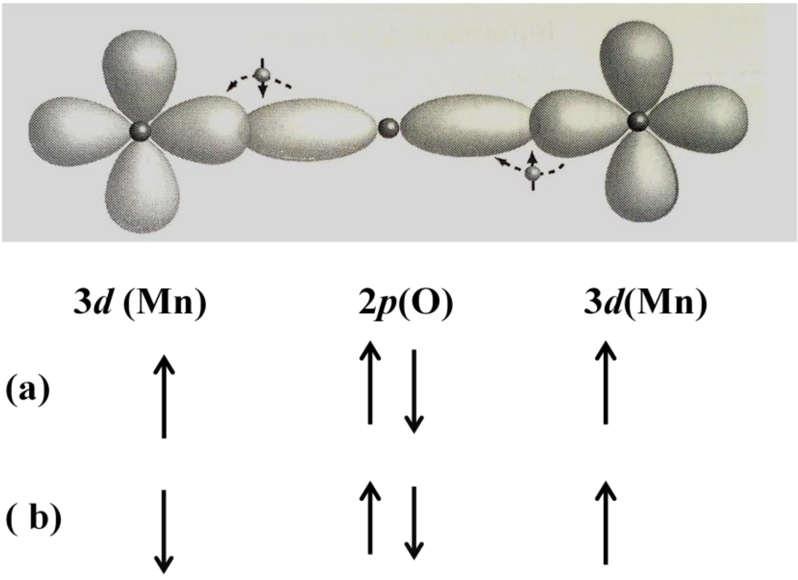

Figure 1.7: Schematic showing mechanism of Superexchange.

Double-exchange interactions

Double exchange interactions occur between 3*d* orbitals when they have both the localized and itinerant electrons. In mixed valence compounds where cations are present in more than one oxidation state like half doped manganite, Mn is present in 3+ and 4+ state it is possible to have ferromagnetic interactions via a non magnetic anion. These interactions involve the actual movement of electron. Thus if we consider the figure shown below, where Mn^{3+} ions are coupled to Mn^{4+} ions via oxygen anion then electron hopping from e_g shell of Mn^{3+} ions take place only when empty e_g orbitals are present in the Mn^{4+} ions.

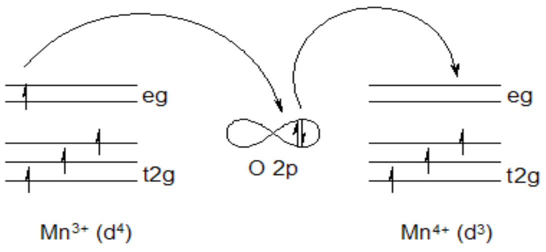

Figure 1.8: Schematic showing mechanism of double-exchange.

Following the Hund's rule the occupancy of the t_{2g} orbital must be high spin which therefore promotes the ferromagnetic coupling and electrical transport in doped manganites (Figure 1.8).

1.4 Electronic Property: Charge ordering

Strongly correlated mixed valent transition metal oxides show an ordered arrangement of cations. This ordering can be in the form of horizontal or vertical stripe like pattern, checkerboard type or charge exchange type extending three dimensionally. When charge ordered state collapses, it results in breaking of symmetry leading to phenomena like high conductivity (colossal Magnetoresistance), superconductivity or ferroelectricity. Half-doped manganites like $Pr_{0.5}CaMnO_3$ exhibit charge-exchange type charge ordering. In this state, cations get arranged in zig-zag chains and the ions in chains are ferromagnetically coupled to each other but having antiferromagnetic coupling with the neighbouring chains.

1.5 Motivation

In the present thesis, there are two classes of materials on which our study was focused: i) Ferrites and ii) Manganites.

Ferrites

Richard Feynman once stated that ferrites are one of the most intricate areas for theoretical description [from Feynmann lecture series 2], but very interesting for studies and practical applications. During past 50 years, ferrites have emerged as an important class of magnetic materials [4]. They constitute the backbone of modern technology with a plethora of applications in almost every sector; such as automobile industry, semiconductor industry, electrical appliances, power supplies, telecommunications, microwave devices and storage media [26]. Ferrites are found to exist broadly in four crystal structures, namely, s*pinels* (cubic structure with general formula of the form MFe_2O_4 with M-divalent metal ion), *garnets* (dodecahedral or 12-sided structure with general formula $3M_2O_3.5Fe_2O_3$ or $M_3Fe_5O_{12}$ where M is generally Yittirium or a rare earth ion), *hexagonal ferrites* (magnetoplumbite structure, $MFe_{12}O_{19}$ or $MO.6Fe_2O_3$, where M can be Ba, Sr, or Pb) and *orthoferrites* (perovskite structures of the form $MFeO_3$ where M is alkali, alkaline earth or rare earth ion) [4, 27]. Ferrites with the other structures are the derivatives of the above mentioned crystalline forms.

Since the advent of hexagonal ferrites or hexaferrites in 1950s, they have attracted tremendous interest of the research community. This is reflected from an exponential growth in the number of research papers in this field [26]. One subclass of these ferrites is constituted by Barium ferrites widely used as a raw material for permanent magnets, magnetic recording media and microwave devices. Particularly, the barium ferrite with stoichiometry $BaFe_{12}O_{19}$ has numerous applications owing to its large coercivity, large saturation magnetization, large magnetic anisotropy and high chemical stability against corrosion [26, 28, 29]. The greatest advantage of this material is that it is cheaper and lighter as compared to other metallic alloys (Co-Ni) and rare-earth magnets. Due to its stability against corrosion, this material does not require surface coating. This, in turn would mean lower cost, long term storage without loss of data over time and higher signal to noise ratio. Moreover, barium ferrite particles are small in size as compared to metal particles resulting in higher packing density of tapes and, thus, higher storage capacity. In 2006, researchers of IBM used FujiFilm Nanocubic technology and demonstrated that up to 6.6 billion bits per square inch of data tape can be stored using barium ferrite particles [30], 15 times greater than the current storage media.

Hexagonal rare earth orthoferrites (h-$RFeO_3$, R- Sc, Y, and Ho–Lu), a family of canted antiferromagnets, are expected to show ferroelectric behavior owing to their polar structure. This makes them good candidates for multiferroicity. Recently, there have been reports on multiferroic ordering in orthoferrites like $YbFeO_3$ [31], $LaFeO_3$ [32] and room temperature multiferroicity in $LuFeO_3$ [33].

Manganites

'Manganites' is one of the most extensively studied classes of perovskite oxides, with diverse magnetic and electronic properties and fascinating phase-diagrams exhibiting structure-property correlations. The general stoichiometry of manganites is $R_{1-x}A_{1-x}MnO_3$ (R is trivalent cation, A is divalent cation). Basically, $RMnO_3$, is antiferromagnetic-insulating system, but when doped by divalent ions at R-site, the valence state of Mn changes from trivalent to tetravalent in order to balance the charge without changing oxygen stoichiometry. In this manner, divalent doping actually controls the $Mn^{3+/4+}$ ratio at B-site. This change in valence state initiates double-exchange of electrons and thereby shows a doping dependent conductivity in these materials. The electronic state of manganites is strongly correlated to the magnetic ground state; for example, metallic manganites show ferromagnetic state and insulating manganites exhibit antiferromagnetic state. These manganites with optimal divalent ion doping (x =0.3), tend to show maximum colossal magnetoresistance and hence these manganites have large potential for variety of application [34, 35].Therefore, the manganites with $x = 0.3$ have been studied extensively in recent past.

The half-doped manganites (with $x = 0.5$ in $R_{1-x}A_{1-x}MnO_3$) show insulating state due to charge-orbital-ordering phenomenon. Most of the half-doped manganites are antiferromagnetic-insulators and show drastic drop in resistance simultaneous to metamagnetic transitions on application of high magnetic fields [36]. Some of half-doped manganites tend to show sharp multiple step-like metamagnetic transitions at very low temperatures, simultaneous to transition in resistivity from insulating to metallic state [37]. Thus, these sharp transitions bring colossal magnetoresistance simultaneous to first-order metamagnetic transition at low temperatures [37, 38]. Some of well known half-doped manganites include $Pr_{0.5}Ca_{0.5}MnO_3$, $La_{0.5}Ca_{0.5}MnO_3$ $Pr_{0.5}Sr_{0.5}MnO_3$, $Nd_{0.5}Sr_{0.5}MnO_3$, *etc.* Also, these manganites are further doped and studied in order to investigated ground-state properties and structure-property correlations [39].

The manganites are studied in bulk forms (single-crystals or polycrystalline pellets) to understand the physical properties from point of view of fundamental science and also, there is plethora of reports on thin films, studied in order to investigate potential of manganites in applications.

Present study

The work presented in the thesis focuses on the study of magnetic and structural correlations in two exotic varieties of complex perovskite oxides, namely ferrites [$BaFeO_{3-\delta}$ (BFO)] and manganites [$Pr_{0.5-x}Ce_xCa_{0.5}MnO_3$]. BFO in bulk and thin film form shows intriguing variety of structural and magnetic properties. BFO is room-temperature ferromagnet with rarely occurring ‘tetravalent’ state of Fe. However, BFO shows a complex magnetic behavior which is not yet fully explored. Also the reports show inconsistencies in the results. Thus, there is plenty of scope for investigations in order to unravel novel physics in the form of thin films, as thin films are best known for tuning physical properties by epitaxial-strain.

As mentioned earlier too, BFO has potential for applications as permanent magnet and microwave devices in insulating state. Oxygen annealing of BFO results into modifications of magnetism. The changes in magnetization are large and correlated with structural transformations. In order to explore the complex magnetic properties of BFO and establish the structural and magnetic correlations in thin films, we have synthesized thin films and investigated the materials using three different approaches: namely, *i)* effect of strain, *ii)* effect of chemical modification and *iii)* effect of oxygen annealing. We have prepared several series of undoped and doped (Ti- and Ru- doped) films, with tensile and compressive strain and studied the effects of strain, doping and oxygen annealing. Our study show strong correlations between the structure and magnetism of BFO. The ground state of BFO is delicately balanced and when the balance is perturbed by even small changes, we observed large effects on the magnetic properties.

To further engineer the magnetic ground state, we prepared several multilayers in combination of $BaTiO_3$ and found that, by restricting degrees of freedom of BFO, the magnetic properties can be actually controlled/modified.

Apart from deposition techniques, we used *MeV* ion irradiation as a tool to probe the properties of BFO films. Swift ion irradiation creates defects (of nanometer size), relaxes strain and modifies oxygen stoichiometry in a controlled way. BFO films were irradiated with 150 *MeV* Ag^{+15} ions and 100 *MeV* O^{+7} ions. We observed systematic variations in structure and magnetism of irradiated BFO thin films.

Last part of the thesis is devoted to the study of manganite thin films. Half-doped $Pr_{0.5}Ca_{0.5}MnO_3$ (PCMO), when doped with cerium, shows interesting phase-diagram with doping dependent structural transitions, accompanied by equally wide variety of magnetic properties ranging from metamagnetism to spin-glass state. There are reports that the manganites attain different structures in antiferromagnetic and ferromagnetic state. Thus, the metamagnetic transition from antiferromagnetic to ferromagnetic state should also cause a structural transformation of the system. It suggests that the multiple sharp metamagnetic transitions acquired in Ce-doped PCMO system must be taking place simultaneous to structural transformation of the first-order at low temperature. However, there have been no studies on thin films of these materials. Hence, with a motivation to explore how the magnetic and structural properties of Ce-doped PCMO would evolve in thin films, we have prepared and studied these films with different thicknesses and different epitaxial strain. Here, we report metamagnetic and structural transitions in epitaxial thin films as a function of Ce-doping in PCMO system.

References

1. Rao C. N. R. (1989), Transition Metal Oxides, Annu. Rev. Phys. Chern., 40, 291.
2. Catalan G. (2009), Physics and Applications of Bismuth Ferrite, Adv. Mater., 21, 2463 (doi: 10.1002/adma.200802849).
3. Zhang Q. *et al* (2013), Direct Observation of Multiferroic Vortex Domains in $YMnO_3$Scien. Rep., 3: 2741 (doi: 10.1038/srep02741).
4. Goldman A. (2006), Modern Ferrite Technology 2nd edition, Springer (978-0-387-28151-3).
5. Dagotto E. (2007), When Oxides Meet Face to Face, Science, 318, 1076 (doi: 10.1126/science.1151094).
6. Izyumskaya N., AlivovYa., Morkoç H. (2009), Oxides, oxides, and more oxides: high-κ oxides, ferroelectrics, ferromagnetics, and multiferroics, Critical Reviews in Solid State and Materials Sciences, 2010,1-260.
7. Goldschmidt, Victor M. (1926). Die Gesetze der Krystallochemie Die Naturwissenschaften 21: 477–485.
8. Rondinelli J. M. , May S. J., Freeland J. W. (2012), Control of octahedral connectivity in perovskite oxide heterostructures: An emerging route to multifunctional materials discovery, MRS Bulletin, 37, 261, (doi: 10.1557/mrs.2012.49).
9. Rodriguez-Martinez L. M., Attfield J. P. (1998), Cation disorder and the metal-insulator transition temperature in manganese oxide

perovskites Phys. Rev. B, 58, 2426. (doi: 10.1103/PhysRevB.58.2426).

10. Li W. *et al* (2013), Oxygen-Vacancy-Induced Antiferromagnetism to Ferromagnetism Transformation in $Eu_{0.5}Ba_{0.5}TiO_{3-\delta}$Multiferroic Thin Films , Scientific Reports, 3 : 2618, 1-6 (doi: 10.1038/srep02618).
11. Du Y. *et al* (2013), Manipulation of domain wall mobility by oxygen vacancy ordering in multiferroic $YMnO_3$, Phys.Chem. Chem. Phys., 15, 2010 (doi: 10.1039/c3cp52892h).
12. Reehuis M. *et al* (2012), Neutron diffraction study of spin and charge ordering in $SrFeO_{3-\delta}$, Phys. Rev. B, 85, 184109 (10.1103/PhysRevB.85.184109).
13. M. C. M.,Chancey C. C. (1993), The Jahn–Teller effect: An introduction and current review, Am. J. Phys., 61(8), 688 (doi: 10.1119/1.17197).
14. Correlated electron phases, www.psi.ch/swissfel/correlated-electron-phases.
15. Blundell S. (2001), Magnetism in Condensed Matter, Oxford University Press (0 19 850592 2).
16. Englman R., Halperin B. (1970), Cooperative Dynamic Jahn-Teller Effect .I. Molecular Field Treatment of Spinels, Phys. Rev. B, 2, 75-94.
17. Cullity B. D., Graham C. D. (2008), Introduction to Magnetic Materials, 2nd ed., Wiley-Blackwell (978-0471477419).
18. Magnetic Design, http://www.electronenergy.com/magnetic-design/magnetic-design.htm.
19. Hubert A., Schäfer R. (2009), Magnetic Domains-The Analysis of Magnetic Microstructures, Springer (978-3-540-64108-7).
20. Chikazum S. (1997), Physics of Ferromagnetism 2nd edition, Oxford university press (0-19-851776-9).

21. Bozorth R. M. (1958), Magnetization in Single Crystals of Some Rare-Earth Orthoferrites, Phys. Rev. Lett., 1, 3 (doi:10.1103/PhysRevLett.1.3).

22. Néel L. (1953), Some New Results on Antiferromagnetism and Ferromagnetism, Rev. Mod. Phys., 25, 58.
23. He T. and Cava R. J.,Disorder-induced ferromagnetism in $CaRuO_3$, Phys. Rev. B,63 172403 (doi: 10.1103/PhysRevB.63.172403).
24. Matsui T., Taketani E., Sato R., Morii K. (2007), Origin of the leakage current inZr-substituted magneto-dielectric$BaFeO_{3-\delta}$ single-crystal films on(001) $SrTiO_3$ substrates, J. Phys. D: Appl. Phys., 40, 6066 (doi:10.1088/0022-3727/40/19/045).
25. Callender C., Norton D. P., Das R., Hebard A. F., Budai J. D. (2008), Ferromagnetism in pseudocubic $BaFeO_3$ epitaxial films, Appl. Phys. Lett., 92, 012514-3 (doi: 10.1063/1.2832768).
26. PullarR. C. (2012), Hexagonal ferrites: A review of the synthesis, properties and applications of hexaferrite ceramics, Progr. Mater. Sci., 57, 1191–1334 (doi.org/10.1016/j.pmatsci.2012.04.001).
27. Smit J., Wijn H. P. J. (1959), Ferrites, Philips Technical Library.
28. Affleck L. *et al* (2000), Combustion Synthesis of $BaFe_{12}O_{19}$ in an External Magnetic Field: Time-Resolved X-ray Diffraction (TRXRD) Studies, Adv. Mater., 12, 1359 (doi: 10.1002/1521-4095).
29. Jia J. (2013), Exchange coupling controlled ferrite with dual magnetic resonance and broad frequency bandwidth in microwave absorption, Sci. Technol. Adv. Mater. 14, 045002 (doi: 10.1088/1468-6996/14/4/045002).
30. Fujifilm technology key to IBM demo of multiple terabyte storage, http://www.fujifilm.com/news/n060519.html.

31. Jeong Y. K. *et al* (2012), Structurally tailored hexagonal ferroelectricity and multiferroism in epitaxial $YbFeO_3$ thin-film heterostructures, J. Am. Chem.Soc., 134, 1450−1453 (dx.doi.org/10.1021/ja210341b).
32. Acharya S., Mondal J., Ghosh S., Roy S.K., Chakrabarti P.K. (2010), Multiferroic behavior of lanthanum orthoferrite ($LaFeO_3$), Mater. Lett., 64, 415–418 (doi:10.1016/j.matlet.2009.11.037).
33. Wang W. *et al*(2013), Room-temperature multiferroic hexagonal $LuFeO_3$ films, Phys. Rev. Lett. , 110, 237601 (doi: 10.1103/PhysRevLett.110.237601).
34. Helmolt R. V. *et al* (1993), Giant negative magnetoresistance in perovskitelike, Phys. Rev. Lett., 71, 2331(doi/10.1103/PhysRevLett.71.2331).
35. Jin S. *et al* (1995), Thickness dependence of magnetoresistance in La–Ca–Mn–Oepitaxial films, Appl. Phys. Lett., 67, 557 (doi.org/10.1063/1.115168).
36. Hardy V. *et al* (2003), Staircase effect in metamagnetic transitions of charge and orbitallyorderedmanganites, J. Magn. Magn. Mater. 264, 183 (doi:10.1016/S0304-8853(03)00201-4).
37. Mavani K. R. *et al* (2012), Spin dynamics of $(Pr0._{5-x}Ce_x)Ca_{0.5}MnO_3$ (x=0.05, 0.10, and 0.20) system studied by muon spin relaxation, J. Appl. Phys., 112, 073911 (doi: 10.1063/1.4754848).
38. Mavani K.R., Paulose P. L.(2007), magnetic field cycling induced anomalous irreversibility in resistivity of charge ordered manganites, Euro. Phys. Lett. 78, 37004 (doi: 10.1209/0295-5075/78/37004).
39. Rana D. S. *et al* (2004), Disorder effects in $(LaTb)_{0.5}(CaSr)_{0.5}MnO_3$ compounds , J. App. Phys., 95, 7097 (doi:10.1063/1.1687257).

~ End of Chapter 1 ~

Chapter 2

Synthesis of Materials and Experimental Techniques

This chapter describes the details of various synthesis and characterization techniques used during the course of research work. We begin with describing the synthesis of samples, which is divided in to two parts: *i)* synthesis of bulk materials and *ii)* thin film deposition.

2.1 Synthesis of bulk materials

The polycrystalline bulk materials were prepared by solid state reaction method. These bulk materials are required to be prepared in form of disc-shaped pellets with a diameter of 15-20 *mm* and with a weight of 3.5 – 4 *gm*. These pellets are used as targets for deposition of thin films.

2.1.1 Solid state reaction method

Solid state reaction is one of the most extensively used processes for making polycrystalline bulk samples of oxides [1]. Solid state reaction method is advantageous over chemical route processes since the solubility of reactants in water or solvents limits the utility of the latter, whereas no such solvents are required in the former. In the wet methods, once the reaction is complete the residual solvent needs to be removed from the final product. No such purification process is required in the solid state reaction method thus, making it simpler and cheaper. Also, this method is environment-friendly as there is no waste product (or solvent) to discard at the end.

The solid state reaction method involves the heating of two or more high-purity powders (metal oxides, carbonates, nitrides, *etc.*) weighed and mixed proportionally to form the desired product. The reactions in solids take place in a constrained environment of crystal lattices; therefore it not only requires high temperatures for overcoming the lattice energy, but it also needs uniform mixing of reactants so that the cations and anions can diffuse to newer sites. For better reactivity, it is required that the constituent materials are thoroughly grinded to ensure homogeneous mixing. This increases the surface area, maximizes the contact between the reacting solids and hence ensures better reactivity. The grinding could be performed either manually by using a mortar and a pestle or mechanically by using a ball-mill. For homogeneous mixing of the reacting powders, Isopropanol or Acetone could sometimes be added to the mixture once or twice during grinding process. The addition of any such liquids causes the coarse particles to settle down at the center of mortar thereby facilitating the grinding process. These volatile organic liquids evaporate gradually during grinding. The grinding process is usually carried over a period of about 3-4 *hrs* for 4 *gm* of material to ensure uniform blending of reacting powders. After the first grinding, the mixture has to be calcined to remove volatile components like CO_2, NO_2 *etc*. This is followed by intermittent grindings and heating at various high temperatures. In some cases, the mixture is pelletized using a hydraulic press before heating, for better contact and increased reactivity between the crystallites. These pellets are then reground before next heating. The final sintering of the pellet is carried at an optimized temperature. The samples are sintered in air or in presence of a gas (*e.g*. O_2, Ar, *etc.*) depending on the requirement.

The disadvantage of solid state reaction method is that the technique being diffusion-limited requires high temperatures for synthesis and therefore sometimes there can be incomplete reactions or formation of compositionally inhomogeneous products.

In the later subsection, we describe the procedure adopted for the preparation of bulk pellets of the materials under study. All the powders used for bulk synthesis had purity ≥ 99.99%.

2.1.2 Synthesis of $BaFeO_{3-\delta}$, $BaFe_{0.9}Ti_{0.1}O_3$ and $BaFe_{0.9}Ru_{0.1}O_3$

The bulk sample of $BaFeO_{3-\delta}$ (BFO) was prepared by mixing $BaCO_3$ and Fe_3O_4 powder in required molar ratios. The mixture was grinded for 3 to 3.5 *hrs* using pestle-mortar. Isopropanol was mixed twice during the first grinding. The ground powder was placed in an alumina crucible which was covered with an alumina lid and heated at 950^oC for 6 *hrs* in air in a furnace. After the first heating, powder was grinded again for about 2 *hrs*. The powder was made into pellet using a 20 *mm* die-set by applying a pressure of 4.5 *tons* for 5 *min* with the help of a hydraulic press. The pellet was sintered at 1000^oC for 12 *hrs* in air in the box furnace. Once cooled, the pellet was again grinded to a fine powder for about 2 *hrs* and made into pellet using the above mentioned procedure. The pellet was finally sintered at 1100^oC for 10 *hrs* in air in the box furnace. The cooling rate was set to 5$^oC/min$ at every stage.

The bulk sample of $BaFe_{0.9}Ti_{0.1}O_3$ was prepared by mixing $BaCO_3$, Fe_3O_4 and TiO_2 powders in molar ratios. The rest of the procedure was same as that described for BFO

The bulk sample of $BaFe_{0.9}Ru_{0.1}O_3$ was prepared by mixing $BaCO_3$, Fe_3O_4 and RuO_2 powders in required molar ratios. The rest of the procedure was same as that for BFO.

2.1.3 Synthesis of $Pr_{0.5}Ca_{0.5}MnO_3$, $Pr_{0.45}Ce_{0.05}Ca_{0.5}MnO_3$ and $Pr_{0.4}Ce_{0.1}Ca_{0.5}MnO_3$

To prepare the bulk samples of $Pr_{0.5}Ca_{0.5}MnO_3$, Pr_6O_{11}, $CaCO_3$ and MnO_2 powders were first mixed in the required molar ratios. The mixture was grinded for 4-5 *hrs*. To ensure homogeneous mixing, Isopropanol was mixed twice or thrice during grinding. The ground powder was placed in an alumina crucible, covered with lid, and placed in a box furnace to be calcinated at 950 ^oC for 24 *hrs* in air. The powder was then sintered at 1050 ^oC and 1150 ^oC for 24 *hrs* with intermediate grinding. Finally, the pellet was prepared using 20 *mm* die-set and by applying a pressure of 5 *tons* for 5 *min* using a hydraulic press. The pellet was placed over a platinum foil and sintered at 1340 ^oC for 24 *hrs*. The rate of heating and cooling was 10$^oC/min$ during the entire process.

To prepare 5% and 10% Ce-doped pellets of $Pr_{0.5}Ca_{0.5}MnO_3$, Pr_6O_{11}, $CaCO_3$, CeO_2 and MnO_2 powders were mixed in molar ratios. Rest of the procedure was same as that described for the undoped sample.

2.2 Synthesis of Thin films

Thin film is a layer of material with thickness ranging from few nanometers to several micrometers. The progress in the field of electronics and computer-technology has caused an upsurge in research on materials to satisfy the need of miniaturize the size, improve capacity and functioning of various devices. Many materials are found to show different properties in bulk and thin film form. New physics may arise in a material on confinement in one or two dimensions when grown as thin film. The combination of thin films in form of multilayer or heterostructures has lead to the evolution of sophisticated phenomena like quantum-well lasers or heterojunction laser. These combinations have opened new avenues for tuning the properties of materials sometimes even leading to evolution of new phenomena at the interfaces which was initially absent in the parent materials. Thin films are important for different applications such as optical coatings, protection against corrosion, in various components in optoelectronics, electronic and magnetic devices [2]. They have become the best means of research since they have multiple applications and require a very small amount of material.

Epitaxy basically refers to extended single crystal growth of a material over single crystal substrate [2,3]. An epitaxial thin film follows the substrate orientation. In many thin film applications epitaxial growth of thin films is of little importance except for semiconductor technology which requires highly pure defect free growth of thin films.

The synthesis of thin films requires a template over which it nucleates and the geometry of which it follows [4]. Such templates are called as substrates which are generally single crystal oxides, semiconductors or metals. The substrates are so chosen that the lattice parameters are nearly same as those of the materials to be deposited. When there is a minor mismatch between the lattice parameters of the material and substrates, the lattice structure of the films get strained. This epitaxial strain can be used to tailor the properties of thin films. There are several techniques for thin film fabrication which includes molecular beam epitaxy, chemical vapor deposition, ion beam sputtering, magnetron sputtering, pulsed laser deposition *etc.*

2.2.1 Pulsed Laser Deposition

The advent of lasers in 1960 marked the beginning of a new era of materials research. In 1965 the first attempt to deposit thin film using high power ruby laser was demonstrated by Smith and Turner [5]. In the 1980s with the growing demand for fabricating high T_c superconductors for various applications, scientists were urged to seek efficient techniques for thin film fabrication. The major breakthrough came with the invention of Pulsed Laser Deposition (PLD) by Venkatesan in 1987 [6, 7, 8]. He was first to demonstrate successful synthesis of thin films of high T_c superconductor $YBa_2Cu_3O_7$. It gave the right impetus to the development of laser as a tool to ablate the material by using laser and fabricate thin films. This technique was called Pulsed Laser Deposition (PLD). With the development of laser technology, the PLD technique became competitive. Today it is used to deposit thin films of a variety of complex oxides, semiconductors, multilayer thin films and superlattices, making it a very versatile technique.

Principle of operation

The process of PLD can be divided into three stages. The first stage is the laser material interaction. When a high power pulsed laser of sufficiently high energy-density is made incident on the material, it penetrates the surface within a certain depth. The penetration depth depends on two parameters: *i)* laser wavelength and *ii)* refractive index of the target material at the incident wavelength. The electric field associated with an electromagnetic wave is given by the equation [5]:

$$E = \left(\frac{2\Phi}{c\varepsilon_0 n}\right)^{\frac{1}{2}}$$

Where, E = electric field of the electromagnetic wave in V/m

Φ = power density in W/cm^2

ε_0 = dielectric constant in vacuum

n = refractive index

c = velocity of light

If we consider a material of refractive index $n = 1.5$ and a laser pulse with a peak power density of ~ $10^8 W/cm^2$ is incident on it then it would generate an electric field of about ~ $10^5 V/cm$, which is high enough to cause dielectric breakdown. Thus, when a short laser pulse hits the target it gets heated up, melts and vaporizes to ablate out from the target surface with the stoichiometric ratio of the target material. The instantaneous ablation rate depends on the laser fluence shined on the surface. The shorter laser pulses would result in congruent evaporation. A parameter called as thermal diffusion-length is defined as [5]:

$$L = 2\,(D.\tau)^{1/2}$$

Where D is thermal diffusivity and τ is laser-target interaction time, which is equal to the pulse duration.

For congruent ablation, thermal diffusion length must be equivalent to the thickness of the ablated layer per pulse. Thus if shorter pulses of laser are used, it is more likely that the ablation is congruent, thus allowing PLD to maintain the stoichiometry of the target material in thin film. The second stage is the formation of a plasma plume containing ions, electrons, micron sized chunks and molten globules of the material. Due to coulomb repulsion and recoil from the target surface this cloud of energetic particles moves in forward direction normal to the target surface and impinges on the substrate surface placed in line to the target. The angular spread of the ablated material is governed by the laser spot-size, plasma-temperature and the distance between the target to substrate. The spatial distribution of plume depends on the gas pressure inside deposition chamber.

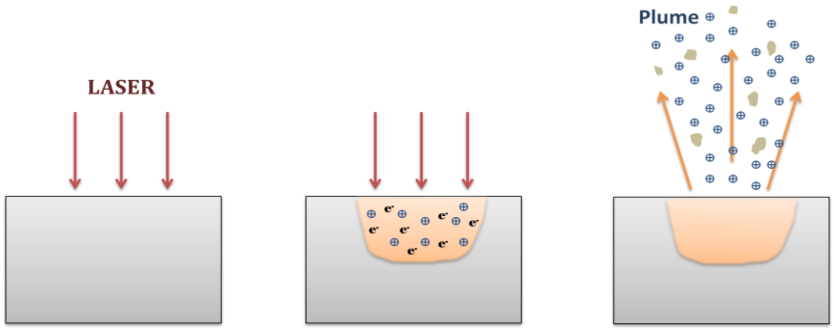

***Figure 2.1: The process of ablation by laser during thin film deposition*.**

The third and final stage is the nucleation of thin film on the substrate surface. As the highly energetic species strike the substrate surface, initially it will sputter atoms from the substrate surface. A thermalized region by the interaction of these sputtered atoms and the plume is formed beyond which the film growth starts. The growth of thin films depends on a number of parameters like the temperature, physical and chemical properties of the substrate, pressure inside the chamber, ratio of gases inside the chamber, *etc.*

The prime advantage of PLD system is the ease of use and low initial set up cost as compared to other techniques like Molecular Beam

Epitaxy (MBE). Since the laser and the deposition system are separate parts, several deposition systems can be used with the single laser source by using beam splitters and mirrors. In PLD, the congruent evaporation maintains the stoichiometric proportions of chemical species, so one can make single-phase films even if the target is multiphase. Complex multilayers and superlattices can be fabricated using multi-target rotations. Moreover, the size of target required for deposition is very small as compared to larger size required for other techniques like Ion Beam or Magnetron Sputtering. Also, absence of heating elements and discharging electrodes in the deposition system gives freedom to fabricate the films in the ambience of any kind of reactive gases.

There are two major limitations of PLD, first is splashing or particulate generation which can hinder the use of thin films prepared by PLD in device applications. Second is lack of uniformity of film over large area due to narrow angular distribution of the plume. The uniformity can be maintained in not more than 10 *mm* × 10 *mm* area.

Experimental Design

The Pulsed Laser Deposition system consists of three main parts. These are the essential constituents of a PLD setup; however, there can be various modifications in these components depending on the need of applications. Here we describe in detail the setup installed at IIT Indore.

a) Laser

Lasers of various wavelengths in infrared (IR), visible and ultraviolet (UV) range have been used as source in PLD. Majority of materials show high absorption in the wavelength range of 200 – 400 *nm*. The most commonly used sources for PLD have been Q-switched Nd:YAG (λ - 1.064 μm, second harmonic-532 *nm*, third harmonic 266 *nm*) which is a solid state laser and Excimer lasers such as KrF (λ - 248 *nm*), ArF (λ - 193 *nm*) etc. The advantage of Excimer lasers is that they are gas lasers, directly emitting in ultraviolet region and they are able to provide higher laser fluence (> 1 J/cm^2). Excimer stands for excited dimer. The active medium is a mixture of an inert gas such as Argon, Krypton, Xenon and a reactive halide such gas as Flourine or Chlorine. The inert gases in excited state combine with halides to form a molecule which then dissociates via spontaneous or stimulated emission. Among the excimer lasers, KrF is the highest gain system and one of the most widely used source for PLD. The system in our laboratory at IIT-I has KrF Excimer laser (Coherent made) as the source with a maximum energy up to 400 *mJ*, pulse width 20 *ns* and a maximum repetition rate of 20 *Hz*.

b) Vacuum Chamber

It is a chamber made of stainless steel, which consists of a target holder and a substrate holder. The target holder in the current system can hold six targets. The target surface must be ablated evenly to avoid formations of pitches which deviates the plume from the direction normal to the surface. To achieve this, the target holder is provided with rotation and raster motion so that the laser beam falls uniformly over the entire surface of the target. The substrate holder is placed at an optimized distance from the target holder. It is attached to a heater which can attain and maintain a temperature up to 830 °C. The targets and substrates are mounted on their respective holders using silver paste. There are different ports in this chamber for laser entry, vacuum gauge attachment and for viewing the deposition. As the temperature of heater also raises the temperature of the chamber, there is an arrangement of fans to keep the chamber cool. There is a port for air-suction via vacuum pump and inlet for the flow of gas.

c) Vacuum Pump

The vacuum system is generally a combination of rotary and turbo molecular pumps. Rotary pump is used to evacuate the chamber from atmospheric pressure to around 10^{-3} *Torr*. Turbo molecular pump takes over from this level of pressure and creates a vacuum of the order of 10^{-6} *Torr*.

Figure 2.2 shows the various parts and functioning of a PLD system. Figure 2.3 shows the photograph of the actual setup of PLD in our laboratory. Figures 2.3(a) shows the complete system, 2.3(b) shows the substrate mount and 2.3(c) shows the top view of chamber during a deposition.

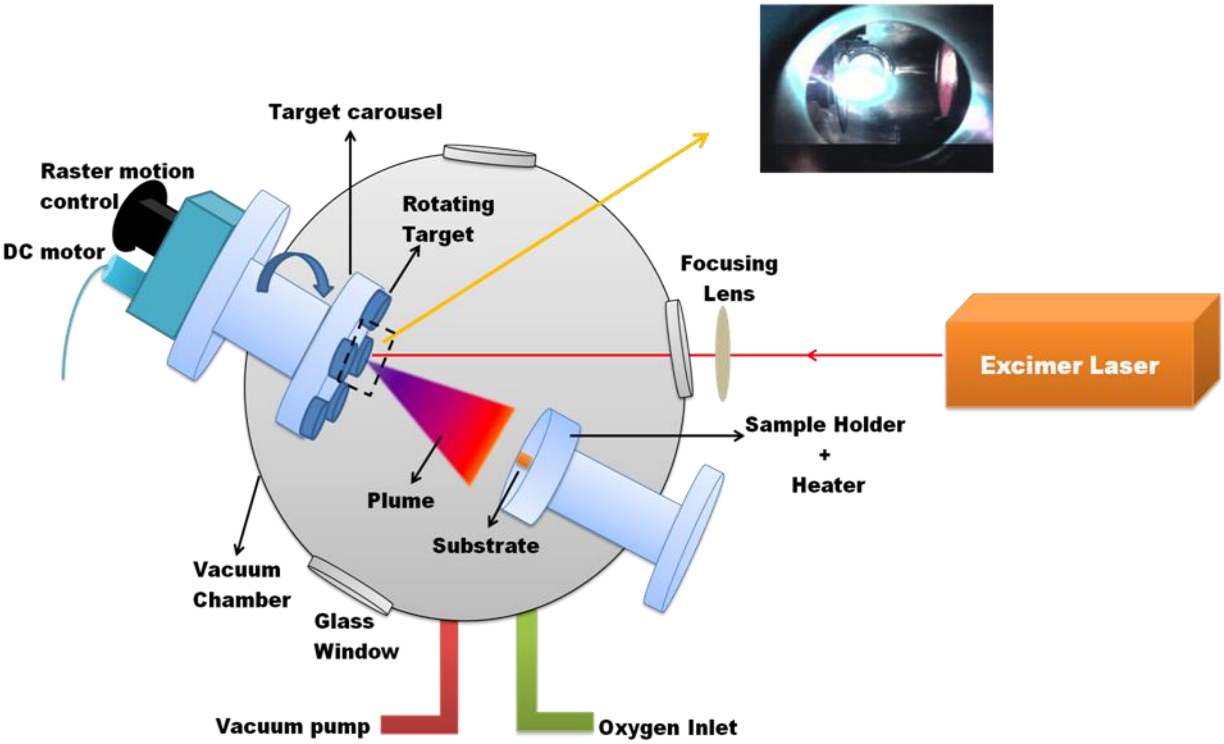

Figure 2.2: Schematic of Pulsed Laser Deposition System

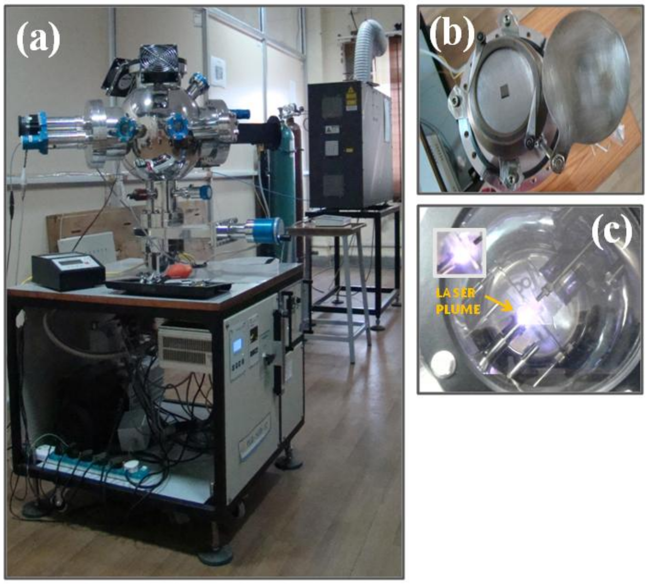

***Figure 2.3: Pulsed Laser Deposition setup at IIT Indore*.**

2.3 Annealing

Annealing is a process of heating a material to higher temperature, generally in vacuum or in presence of gases (*e.g.* oxygen), which can result in alteration of its structural and micro-structural properties. We have annealed undoped and doped $BaFeO_3$ thin films in flowing oxygen using a tube furnace (MTI Corporation). It consists of a quartz tube, with flanges at both ends, placed in a refractory chamber provided with heating elements and a thermocouple to monitor the temperature. When the sample has to be annealed in vacuum one of the flanges can be connected to a vacuum pump. For heat-treatment in the presence of a gas, the desired gas cylinder is connected to one of the flanges using a gas pipe. At the other end a small piece of gas pipe is connected which is immersed in oil. The gas-flow is generally maintained by keeping a watch on bubbles. The sample to be annealed is placed in an alumina boat or on a platinum foil and kept at the center of the tube. The tube furnace has a zone-length of 9 inches for heating.

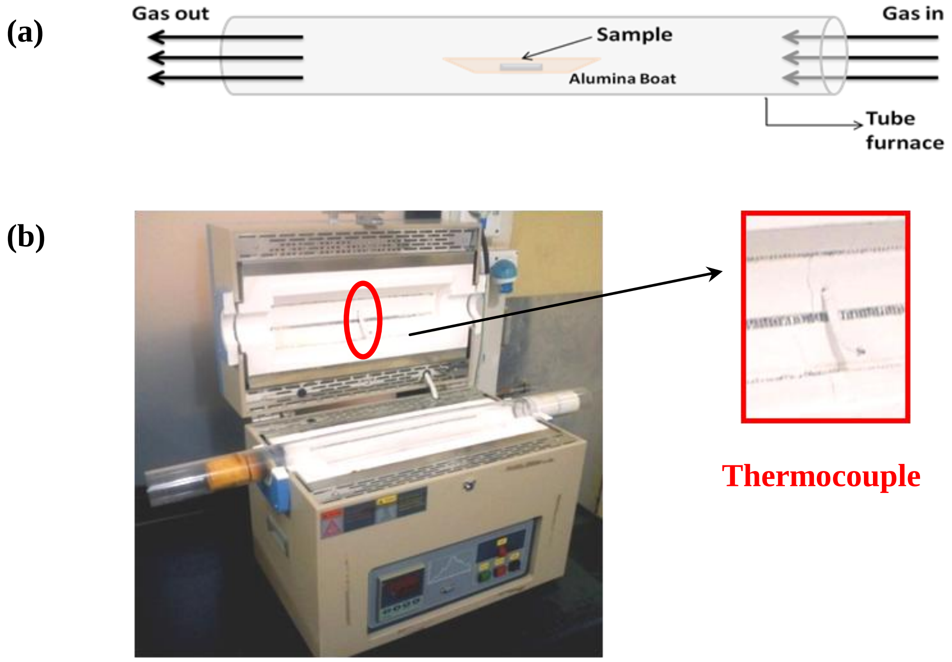

Figure 2.4: a) Schematic of annealing process of bulk or thin film samples, b) The tube furnace used for annealing.

2.4 Characterization Techniques

2.4.1 Structure and Surface Morphology

The structural properties of the bulk and thin film samples were investigated using X-Ray Diffraction (XRD) and Reciprocal Space Maps (RSM). To examine the surface morphology, we used Atomic Force Microscope (AFM). The thickness of these films was determined using X-Ray Reflectivity (XRR) measurements or surface profilometer, depending on the thickness of the films. These techniques are discussed briefly in the coming sections.

a) X-Ray Diffraction

The atomic planes in the crystals have separation of about a few to several angstroms, which is of the order of the wavelength of X-Rays. Thus, when X-Rays are incident on crystalline materials they get diffracted by the crystallographic planes. The diffracted X-rays undergo constructive interference when they satisfy the Bragg's condition [10]:

$$2d \sin\theta = n\lambda$$

Where, d is the separation between the planes, θ is the angle of diffraction, n is the order of diffraction and λ is the wavelength of the incident X-Rays (Cu-$k\alpha$ radiation, 1.5406 Å). Figure 2.5 illustrates a typical XRD system.

Various measurements are used to determine the crystalline state (*i.e.* whether single crystal, polycrystalline or amorphous), lattice parameter, grain size, strain and orientation of materials. The θ-2θ scan is used to determine the precise value out-of-plane lattice parameter [6, 7] of thin films or lattice parameters of polycrystalline powder. In case of thin films, the precise determination of lattice constants of the film and the substrates gives the information of strain present in the system. If the Full Width at the Half Maximum (FWHM) of each Bragg peak of a system is constant then it is an indirect measure of the crystallite size.

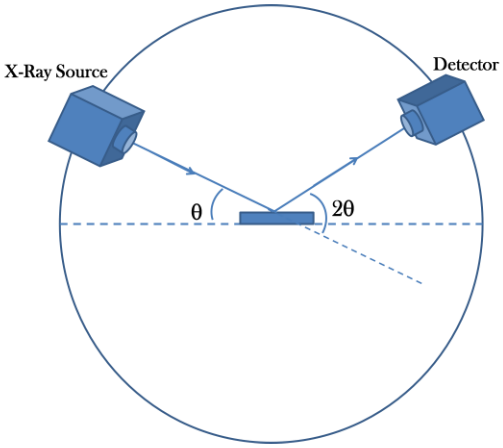

Figure 2.5: Illustration of X-Ray Diffraction.

b) Reciprocal Space Mapping

RSM is an effective tool to probe structural qualities such as dislocations, defects in crystalline materials, structural orientations, thickness, layer tilts and strain relaxation in epitaxial layers, interface extent/diffusion in multilayer. The weak superlattice peaks, which may not be visible in a normal XRD, can be detected using these maps. The RSM gives information about the in-plane parameters of thin films as well. We have measured RSMs around asymmetric peaks to explore in-plane lattice mismatch and strain-relaxation in the various films under study.

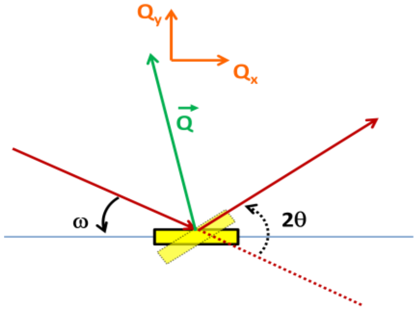

Figure 2.6: Schematic of Reciprocal space mapping (from Panalytical tutorials).

RSM basically is an integration of a series of $\omega/2\theta$ scans around a specific Bragg peak. Here ω is the angle between the sample and the source, 2θ is the angle of detector with respect to the incident beam. Each scan is taken at a different ω value. The scan is obtained in reciprocal lattice units (Q_x, Q_y).

The reciprocal vector components can be expressed in terms of ω and 2θ as follows [10]:

$$Q_x = R[\sin\omega + \sin(2\theta - \omega)]$$

and $Q_y = R[\cos\omega - \cos(2\theta - \omega)]$

The Reciprocal Space Maps of the various thin films were recorded using diffractometer with 5-axes cradle (Emperean, PanAlytical)

(Cu-Kα). The plots were obtained by importing the data to Epitaxy software by PanAlytical.

c) Atomic force microscopy

AFM is a technique to explore the surface topography of thin films [12]. It has the resolution down to few nanometers. AFM consists of a sharp tip of about 2-20 *nm* width attached to a flexible cantilever which moves over the sample surface. The scanning motion is controlled by a tube scanner, consisting of piezo-actuators, by application of different electric potentials. The tip senses the Van-der Waal's forces as it comes in the vicinity of sample surface and maintains a constant distance. A feedback loop is used to obtain a precise motion of scanner or to maintain a constant cantilever surface distance. The motion of cantilever is sensed by shining a laser over it which is then detected by a photodiode after reflection. The mode of operation can be contact mode, where tip is static and it touches the sample surface or non-contact/semi-contact mode where the tip is oscillating with certain resonant frequency and does not touch the sample surface. All the measurements done in the present study were carried out in non-contact mode. We have used AFM (model: AIST-NT SmartSPM) to obtain the images of surface of the thin film samples studied. The tips used were Gold coated (100 *nm*) Silicon tips of height 7-10 μm and curvature 10-25 μm, they were mounted over rectangular cantilever. During the scans, the samples were fixed on the sample holder by a two-sided tape.

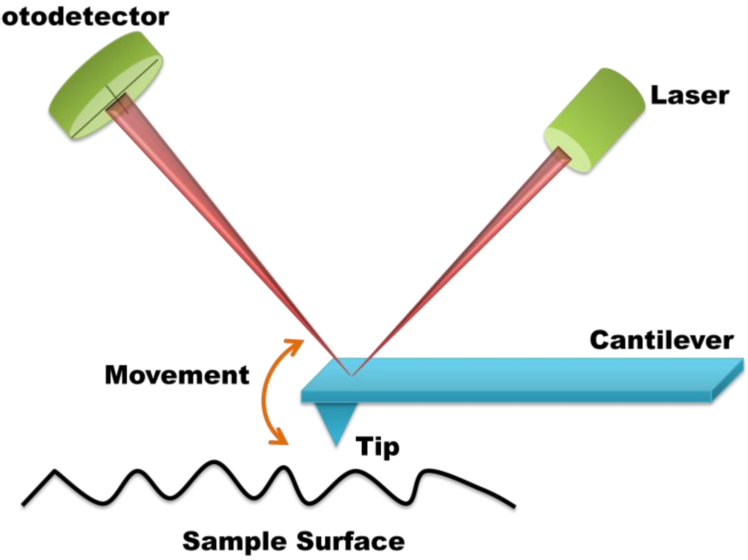

Figure 2.7: Schematics of Atomic force microscope.

2.4.2 Magnetic properties

The Magnetic properties of the thin film samples, such as the variation of Magnetization (M) with varying magnetic field (H) [M(H) curves] or varying Temperature [M(T) curves] were measured using Superconducting Quantum Interference Device – Vibrating Sample magnetometer (SQUID VSM). The ferromagnetic domains on surface of BFO thin films were observed by using Magnetic Force Microscopy (MFM). The magnetoresistance of PCMO thin films was measured using Physical Property Measurement System (PPMS).

a) Magnetometer

A VSM works on the principle of electromagnetic induction. A magnetic sample oscillates at the center of a current carrying coil. As the magnetic flux through the coil changes, it causes a change in the current flowing through the coil. This change in current is measured. A SQUID-VSM uses superconducting magnet and superconducting detection coils for sensing the magnetic moments.

Superconductivity is the property by virtue of which electrical resistivity of certain materials becomes zero when they are cooled below a critical temperature. This phenomenon was discovered in 1911 by Kamerlingh Onnes [13]. Superconductors are known to carry persistent current for years, without any decay. When placed in a weak magnetic field, they behave as diamagnets expelling out all the magnetic flux lines, which is called *Meissner effect*. In superconducting state the conduction electrons form bound pairs known as Cooper pair. When two superconductors are brought close to each other with a thin insulating region separating the two then these electron pairs can tunnel from one superconducting region to another, carrying the supercurrent across the junction. As these electron pairs tunnel the associated waves get coupled. This effect is called as Josephson's Effect and the junction between the two superconductors are called Josephson junction or weak links.

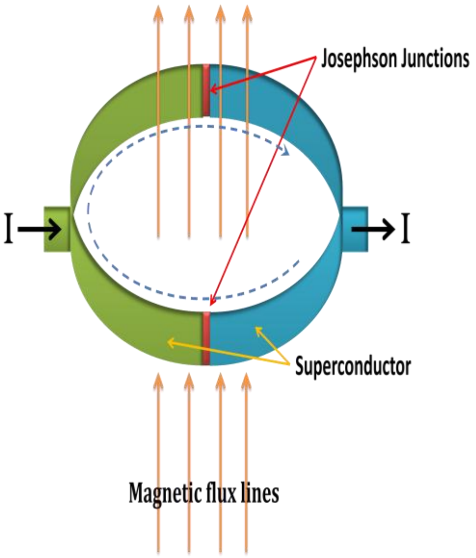

Figure 2.8: Schematic showing principle of SQUID magnetometer [16].

The magnetic flux passing through the superconducting ring is quantized and is given by the following equation [13]:

$$\Phi = \left(\frac{2\pi\hbar c}{q}\right) s$$

Where $q = -2e$ (charge of cooper pair) and s is an integer.

Unit flux, $\Phi_0 = 2 \text{ x } 10^{-15}\ Tesla\ m^{-2}$

SQUID basically consists of superconductors combined by two Josephson junctions. Each of these junctions produces same or opposite phase difference in the current flowing through each, which results in constructive or destructive interference in them. This interference leads to a certain critical current density which can be sustained in the loop without decay. The critical current density is highly sensitive to even a very small change in the magnetic flux associated with the loop. This principle is used in magnetometers to measure the magnetic moments.

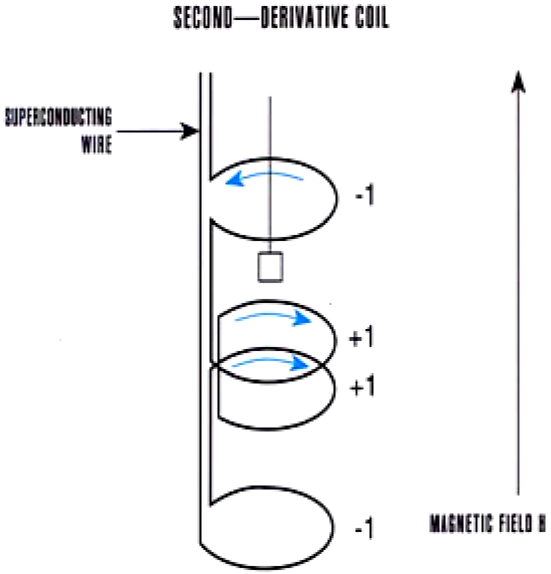

Figure 2.9: Principle of SQUID-VSM.

Magnetization Measurements:

1. Magnetization versus Magnetic field M(H) curve: To study the type of magnetism present in the system M(H) curves are recorded.

2. Magnetization versus Temperature: These measurements are performed to explore the temperature dependence of the magnetization of the materials and to study magnetic transitions. The measurements generally are carried in two parts:

i) Zero Field Cooled (ZFC): In this case the system is cooled to lowest temperature without application of any magnetic field. Then a small field is applied and magnetic moment is recorded while warming the system.

ii) Field Cooled (FC): The system is cooled to lowest temperature in presence of a magnetic field and in presence of the same field the moment is measured while warming the system.

We used SQUID magnetometer by Quantum design for all the magnetic measurements.

b) Magnetic Force Microscopy

It is a type of atomic force microscopy where a ferromagnetic tip is used to characterize the magnetic field distribution over the surface of magnetic thin films. The tip senses the magnetostatic force or the magnetic force gradient on the sample surface and maps the domain structure. The magnetic force microscopy (MFM) works on a two pass mode. In the first pass, the tip scans the surface topography and in second pass it maps the magnetic force from the sample surface following the topography. By this procedure the surface features are automatically subtracted from the total image thereby leaving only the magnetic signal information in the final scan obtained.

The tip used for our measurements were obtained from Mikromasch model number HQ:NSC18/Co-Cr/Al BS made of n-type silicon and coated with Co-Cr, the typical tip radius was 8 *nm* and tip coercivity was 306 *Oe*.

Before recording the MFM images all the films were first made to undergo a magnetic hysteresis cycle by applying a ramp of magnetic field from 0 to 7 *T* at 300 *K* in a SQUID. To maintain the remanent magnetization the samples were then stored in a magnetic field of 30 *mT* till the MFM measurements were made.

c) Magnetoresistance

MR can be measured in two ways:

1. Resistance versus Temperature at a particular field

2. Resistance versus magnetic field at a particular Temperature

The physical property measurement system by Quantum design was used to perform the above measurements.

2.5 Swift Heavy Ion (SHI) Irradiation

Ion irradiation has been used as tool to study the properties of oxide thin films since a very long time. When highly energetic ions impinge on the thin films they pass through it forming cylindrical paths and transferring their energy to the surrounding atoms. The energy of the ion is transferred via two mechanisms. When the energy of the heavy ion is of the order of few *KeV* then the basic mechanism for loss of energy is by elastic scattering with the nuclei of the target atom this is known as the nuclear energy loss and when the energy is greater than 1-2 *MeV* then the mechanism for the loss of energy is via inelastic scattering (electronic excitations of the surrounding atoms). The ion while passing through the material will continuously lose its energy via elastic and inelastic collisions along with small radiative losses as it passes through the material. The total loss dE/dX in energy can be summed as [14]:

$$\frac{dE}{dX} = \left(\frac{dE}{dX}\right)_{nuclear} + \left(\frac{dE}{dX}\right)_{electronic} + \left(\frac{dE}{dX}\right)_{radiation}$$

The loss in energy of ion to the material culminates in form of point defects, columnar defects and phase transformations. Sometimes the irradiation also causes interstitial and substitutional effects. All these structural alterations in the thin films can results in changes in their electrical and magnetic properties. The advantage of this technique is that we can produce defects of *nm* size in a controlled way and hence modify and study the properties of material.

For the irradiation study we used 15UD pelletron at IUAC delhi. Further details will be described in chapter 4.

References

1. A. R. West, (1991) Solid State Chemistry and its Applications, John Wiley and Sons (978-0471908746).
2. Milton Ohring (2001), Materials Science of Thin Films, 2nd ed. Academic Press (978-0125249751).
3. Epitaxy, www.wikipedia.org/wiki/Epitaxy.
4. J. A. Venables, G D T Spiller, M Hanbucken Rep. Prog. Phys. 47, 399 (1984).
5. Douglas B. Chrisey ,Graham K. Hubler, (1994), Plused Laser Deposition of Thin Films, John Wiley and Sons. (978-0471592181).
6. Michael Lorenz, M. S. Ramachandra Rao (2014), 25 years of pulsed laser deposition, J. Phys. D: Appl. Phys. 47, 030301 (doi:10.1088/0022-3727/47/3/030301).
7. T. Venkatesan (2014), Pulsed laser deposition invention or discovery? J. Phys. D: Appl. Phys. 47, 034001(doi:10.1088/0022-3727/47/3/034001).
8. D. Dijkkamp, T. Venkatesan, X. D. Wu, S. A. Shaheen, N. Jisrawi, Y. H. MinLee, W. L. McLean, and M. Croft, (1987), Preparation of YBaCu oxide superconductor thin films using pulsed laser evaporation from high T_c bulk material, Appl. Phys. Lett. 51, 619 (doi: 10.1063/1.98366).
9. Charles Evans , Richard Brundle , Wilson (1992), Encyclopedia of Materials Characterization: Surfaces, Interfaces, Thin Films, Butterworth-Heinemann (978-0750691680).
10. B. D. Cullity, C. D. Graham (2008), Introduction to Magnetic Materials, 2nd ed., Wiley-Blackwell (978-0471477419).
11. Panalytical Tutorials, http://www.panalytical.com.
12. Greg Haugstad (2012), Atomic Force Microscopy: Understanding Basic Modes and Advanced Applications, Wiley-Blackwell (978-0470638828).

13. Charles Kittel (2007), Introduction to Solid State Physics, seventh edition, Wiley India Pvt. Ltd.(978-8126510450).
14. D. K. Avasthi , G. K. Mehta (2011), Swift Heavy Ions for Materials Engineering and Nanostructuring, Springer, (978-9400712287).
15. SQUID Magnetometer, http://hyperphysics.phyastr.gsu.edu/hbase/solids/squid.html
16. Quantum Design, www.qdusa.com/sitedocs/appNotes/mpms/FundPrimer.pdf

~End of Chapter 2~

Chapter 3

Effect of Structural and Chemical Modifications on Magnetic Properties of $BaFeO_{3-\delta}$ Thin Films

3.1 Introduction

Ferromagnetic metals and alloys are disadvantageous in applications involving oscillating/high frequency magnetic fields. These time-varying fields produce voltage resulting in generation of eddy currents which gives rise to resistive heating. Due to these drawbacks, ferrimagnetic materials having insulating state are more conducive for various applications. Ferrites, in general, have Fe in 2+ or 3+ states and they are either ferrimagnetic or antiferromagnetic insulators. However, there are a few ferrite oxides with Fe in unusually high valence state of 4+ and these oxides exhibit some unusual properties. The $AFeO_3$ (A=Ba, Sr, Ca) are examples of such type of oxides with $A^{2+}Fe^{4+}O^{2-}{}_3$ stoichiometry. $CaFeO_3$ is insulting below the antiferromagnetic transition temperature of 290 K and shows charge disproportion [1,2]. $SrFeO_3$ is screw antiferromagnetic and metallic down to 4 K while maintaining the cubic symmetry [3]. Both $SrFeO_3$ and $CaFeO_3$ form in the required stoichiometry under high pressure [4]. $BaFeO_{3-\delta}$ (BFO), the third member of this unusual family, shows weak ferromagnetism. Thus, changing the ionic radius at A-site from 1.12 Å for Ca to 1.42 Å for Ba, the magnetic ground state shows pronounced changes with a strong dependence on the changing structure due to A-site cation radius. Here, BFO does not require high pressures for synthesis.

3.1.1 $BaFeO_{3-\delta}$ in Bulk Form

$BaFeO_{3-\delta}$ (BFO) usually acquires hexagonal state with a = 0.568 nm and c = 1.386 nm in bulk form. However, it is found to exist in various crystalline structures and different magnetic phases depending on the oxygen stoichiometry δ: *triclinic* ($2.64 < \delta < 2.67$), *rhombohedral* ($2.62 < \delta < 2.64$), *tetragonal* ($2.75 < \delta < 2.81$) and *hexagonal* ($2.63 < \delta < 2.92$) [5]. There are contradicting reports over its magnetic behavior as follows. Sabura Mori [6] reported that BFO shows paramagnetic to ferromagnetic transition at 250 K and ferromagnetic to antiferromagnetic transition at 160 K, as temperature decreases [6]. Iga *et. al.* did not observe any ferromagnetic or antiferromagnetic ordering for 160 K > T > 250 K [7]. A metamagnetic transition was also observed in BFO in the temperature range of 140 K-170 K [8]. These inconsistent results indicate that BFO has a complex magnetic ground state and requires further investigations.

The reports on electrical transport properties of BFO reveal that the room-temperature conductivity depends on carrier mobility which is governed by the oxygen vacancies [9]. Low temperature conductivity measurements on BFO in oxygen atmosphere showed it to be n-type semiconductor [9]. In higher temperature range of 400°C to 700°C, BFO showed a dramatic exponential increase in electrical conductivity [9]. Thus in bulk form, BFO shows a range of structural, magnetic and electrical properties.

3.1.2 $BaFeO_{3-\delta}$ in Thin Film Form

The behavior of BFO in thin film is also quite enigmatic reflecting the complex magnetic properties. In thin films, BFO crystallizes in pseudocubic or tetragonal structure and exhibits weak ferromagnetism at room temperature [10]. The BFO thin films show magnetocrystalline anisotropy, possess high dielectric constant [11] and are highly insulating [10, 12]. In various studies on BFO thin films so far, there have been no reports of ferromagnetic to paramagnetic transition temperature up to 390 K except for the case of oxygen annealed films which were reported to show a critical temperature of T_c = 235 K [13]. This implies that the transition temperature of BFO thin films lies at higher temperatures. Oxygen annealing of these films enhances their ferromagnetic moment and makes them highly conducting [13]. The mechanism for such a behavior can be understood as follows. With ideal stoichiometry, $BaFeO_3$

has various elements in ionic forms: Ba^{2+}, Fe^{4+} and O^{2-}. As the oxygen stoichiometry varies from O_3 to $O_{3-\delta}$, a mixture of Fe^{3+} and Fe^{4+} ions takes place in the compound. Now the magnetic complexity arises as per the following explanation. Fe^{3+}-O-Fe^{3+} and Fe^{3+}-O-Fe^{4+} superexchange interactions are antiferromagnetic, whereas Fe^{4+}-O-Fe^{4+} superexchange interactions are ferromagnetic [6]. Therefore, with an increase in the oxygen deficiency, BFO may show antiferromagnetic behavior. To attain ferromagnetic ordering in BFO system, a large Fe content should be stabilized in tetravalent state.

In an attempt to improve ferromagnetic and dielectric properties of BFO thin films, doping of a strongly oxidizing element like zirconium in BFO has also been employed in past [14]. It was found that Zr^{4+} (with $3d^0$), though being non-magnetic, significantly enhanced ferromagnetism in BFO thin films. This is attributed to the strong oxidizability if Zr^{4+} ions which helps to stabilize oxygen in the lattice which in turn stabilizes Fe in 4+ oxidation state. Tetravalent doping (Zr^{4+}) also improves the dielectric properties of BFO thin films.

In spite of all the studies on BFO thin films, its room temperature magnetic behavior seems too complex to be fully understood and leaves plenty of room for further investigations. The prime objective of the present study is to explore magnetic properties of $BaFeO_{3-\delta}$ thin films and modify these properties at room temperature. We tried different mechanisms in order to understand the magnetic properties and its correlations to structural properties of BFO thin films, as briefly described below:

Varying Epitaxial Strain:

As mentioned earlier, $CaFeO_3$, $SrFeO_3$ and $BaFeO_3$ have different magnetic ground state varying from antiferromagnetic to screw antiferromagnetic to weak ferromagnetic state. As varying structure shows largely varying magnetic ground state, the strain in thin films should change the magnetic properties of BFO. So far the effect of changing the type of strain has not been explored for BFO thin films. Especially there are no reports of BFO films grown under tensile strain. We have prepared BFO films on two different substrates under tensile and compressive strains and made a comparative study of the resultant structural and magnetic properties.

Titanium and Ruthenium doping:

We have doped BFO with 10% of tetravalent and non-magnetic titanium (Ti^{4+}) ions. It is expected that doping Ti^{4+} in BFO should stabilize oxygen in the lattice which in turn should stabilize Fe in 4+ valence state. In comparison to non-magnetic dopant, we also doped BFO with 10% ruthenium ions (magnetic). This was done in attempt to understand the magnetic properties of BFO films while comparing effects of non-magnetic and magnetic dopants.

Oxygen annealing:

We then compare the effect of oxygen annealing on the undoped and doped BFO thin films on various substrates in order to understand the effects of oxygen stoichiometry.

The following sections give description of synthesis and characterization results of various undoped and doped $BaFeO_{3-\delta}$ thin films.

3.2 Experimental Details

Polycrystalline bulk pellets of $BaFeO_3$ (BFO), $BaFe_{0.9}Ti_{0.1}O_3$ (BFTO) and $BaFe_{0.9}Ru_{0.1}O_3$ (BFRO) were prepared by conventional solid state reaction method as described in chapter 2. The pseudocubic lattice parameter of bulk BFO is a = 3.997 Å. When films are synthesized over a single crystal substrate, they acquire a strain depending on the lattice mismatch (LM) given by the formula below:

$$LM = |\left(\frac{a_{bulk} - a_{sub}}{a_{sub}}\right)| \times 100\%$$

where a_{bulk} is the lattice parameter of material in bulk form and a_{sub} is the lattice parameter of substrate.

Compressive strain:

When a material is deposited over a substrate with a lattice constant less than that of material, the film experiences a compressive strain. For epitaxial growth, as the material with a larger unit cell takes place over smaller unit cell of substrate it experiences an inward push resulting in decrease of in-plane lattice parameter but at the same time increase in out-of-plane lattice parameter to maintain the unit cell volume.

Tensile strain:

When the material is deposited over a substrate with a lattice constant greater than that of material, the film experiences a tensile strain. As the smaller unit cell takes place over a larger unit cell to maintain the epitaxy, it will experience an outward stretch this will result in increase of in-plane lattice parameter and decrease in out-of-plane lattice parameter to maintain the unit cell volume.

These substrates were so chosen that each of these imparts different epitaxial strain to the films. The lattice mismatch between BFO (a = 3.997 Å) and substrates used for fabrication is listed in Table 3-I. In addition to the above substrates, the undoped BFO thin films were grown over MgO *(110)* and *(111)* substrates in order to investigate magnetocrystalline anisotropy in BFO films.

Table 3-I: Lattice parameters, mismatch with BFO and the type of strain imparted to the films.

Substrates	Lattice constant (Å)	Lattice mismatch	Strain
$SrTiO_3$ *(001)*	3.905	2.35 %	Compressive
MgO *(001)*	4.2	4.83 %	Tensile

Synthesis conditions:

We have used pulsed laser deposition method (described in chapter 2) to deposit various thin films. Laser fluence during deposition was kept between 1.5 - 2.0 J/cm^2. Laser repetition rate was 5 *Hz* and the substrate temperature was maintained at 700°C for all the films. The target to substrate distance was 5 *cm* and oxygen partial pressure during deposition was varied from 1 to 10 *mTorr*. Depositions were carried for 60 *minutes* duration. These films were post-annealed (*in-situ*) for 5 minutes at 100 *mTorr* oxygen partial pressure and cooled in the same pressure at the rate of 10°*C*/min. The undoped films were yellowish in color with orange tan, Ti-doped films appeared darker than the undoped films having a brownish tinge and Ru-doped films were dark brown in color.

To study the effects of oxygen annealing, both the MgO *(001)* and the $SrTiO_3$ (STO) *(001)* substrates were cut into two equal halves. The BFO films were simultaneously deposited on each pair of these halves of substrates. One part was kept untreated and the other part was heated at 900°*C* for 24 *hrs* in presence of flowing oxygen in a tube furnace. All the films after annealing appeared black in color. The as-deposited and annealed films on various substrates will be referred by the abbreviated form listed in the Table 3-II.

Table 3-II: List of sample-codes.

Substrate	**$BaFeO_{3-\delta}$**		**$BaFe_{0.9}Ti_{0.1}O_{3-\delta}$**		**$BaFe_{0.9}Ru_{0.1}O_{3-\delta}$**	
	Pristine	Annealed	Pristine	Annealed	Pristine	Annealed
$SrTiO_3$ ***(001)***	BFO-S	BFO^A-S	BFTO-S	$BFTO^A$-S	BFRO-S	$BFRO^A$-S
MgO ***(001)***	BFO-M	BFO^A-M	BFTO-M	$BFTO^A$-M	BFRO-M	$BFRO^A$-M

3.3 Results and Discussions

3.3.1 Bulk and Thin Films of $BaFeO_{3-\delta}$

Polycrystalline target of bulk BFO was prepared using the procedure described in Chapter 2. The target was found to show two structural phases with hexagonal and cubic symmetry (Figure 3.1), but XRD did not detect any impurity peak. Similarly, the targets of BFTO and BFRO showed multiple structures, but without impurity peaks. As described in Chapter 2, the advantage of PLD is that the single-phase films can be grown using multiphase targets, if all the required elements are present in stoichiometric proportions. Therefore, we used the same targets for deposition of thin films. Two series of films of BFO, BFTO and BFRO were fabricated on two single crystal substrates, namely, MgO *(001)* and $SrTiO_3$ *(001)* and having different lattice-mismatch with the materials (Table 3-I). In the first part of study, the BFO and BFTO thin films were deposited both under tensile and compressive strains. For the sake of brevity, results have initially been discussed separately for each series of films. Then a comparison among them has been made to get deeper insights of effects of doping, oxygen annealing and strain. Followed by this, the series of BFTO films is discussed.

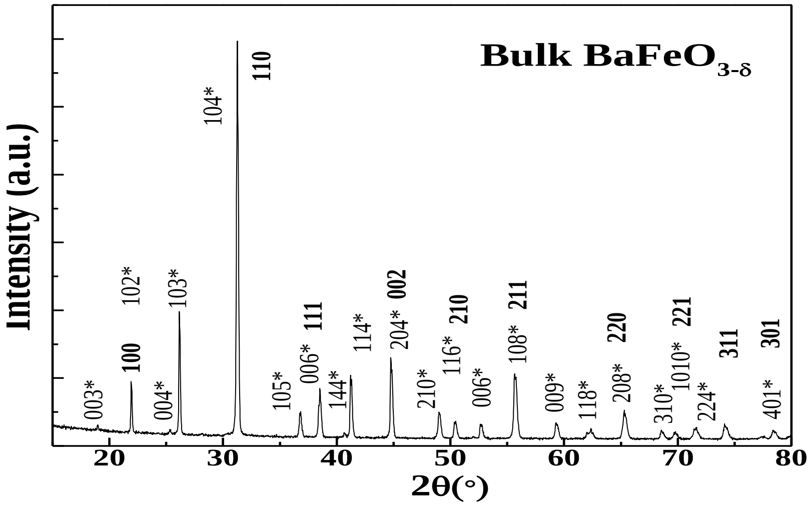

Figure 3.1: XRD pattern of BFO pellet, the bold indices belong to the peaks corresponding to cubic symmetry and '' mark indices correspond to hexagonal symmetry.*

The XRD patterns confirm that all the films are phase pure with no impurity peaks corresponding to iron or barium oxides. The lattice parameter of BFO, BFTO and BFRO thin films on these substrates are listed in Table 3-III.

Table 3-III: Lattice parameters of the various films on two substrates.

	Lattice parameter (Å)	
	$SrTiO_3$ *(001)* Compressive Strain (2.35%)	MgO *(001)* Tensile Strain (4.86%)
$BaFeO_3$	4.071	4.057
$BaFe_{0.9}Ru_{0.1}O_3$	4.078	4.1
$BaFe_{0.9}Ti_{0.1}O_3$	4.083	4.12

3.3.2 Undoped $BaFeO_{3-\delta}$ Thin Films Deposited on MgO *(001)*

The XRD patterns of BFO-M thin film reflects structural growth oriented along the *(001)* crystallographic direction of the MgO single crystal substrate (Figure 3.2).

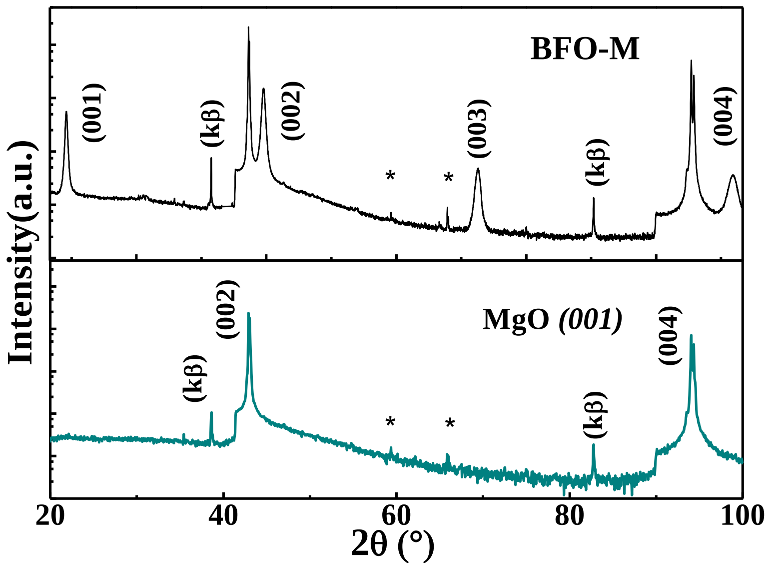

Figure 3.2: XRD pattern of BFO-M thin film and MgO substrate. The data of MgO substrate is shown in order to show that some extra reflections that appear in film, basically originate from MgO substrate on which the film is deposited.

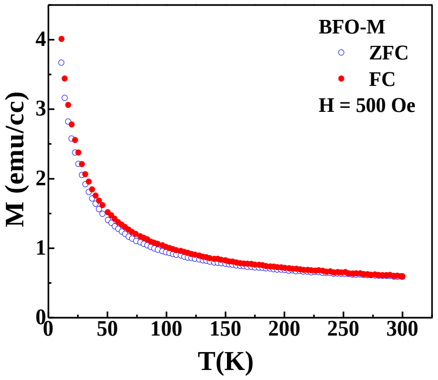

Figure 3.3: ZFC and FC magnetization versus temperature curves for BFO-M.

Figure 3.3 shows the magnetization versus temperature curves recorded in zero-field-cooled (ZFC) and field-cooled (FC) conditions in a field of 500 *Oe*. The ZFC and FC curves showed a minor separation, which indicates presence of short-range ferromagnetic interactions. At low temperatures, the magnetization does not show any transition. Bulk polycrystalline BFO is reported to show a transition to antiferromagnetic state at low temperature, which seems to be absent here. To further probe the magnetic states, magnetization verses magnetic field measurements were performed at 300 *K* and 20 *K*. At 20 *K*, the hysteresis curve does not saturate till high applied magnetic fields, which indicates competing magnetic interactions

(Figure 3.4b). At room temperature, BFO-M film shows weak ferromagnetism as can be clearly seen from the magnetization isotherm in Figure 3.4a. A similar magnetic state has been previously reported for BFO films [10, 13].

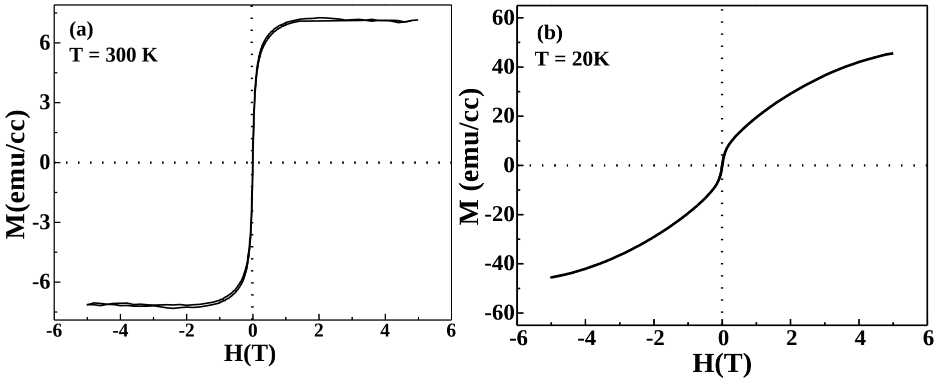

Figure 3.4: Magnetization versus magnetic field isotherms of BFO-M at a) 300 K and b) 20 K.

3.3.3 Oxygen Annealing of BaFeO$_{3-\delta}$ Thin Film on MgO *(001)* Substrate

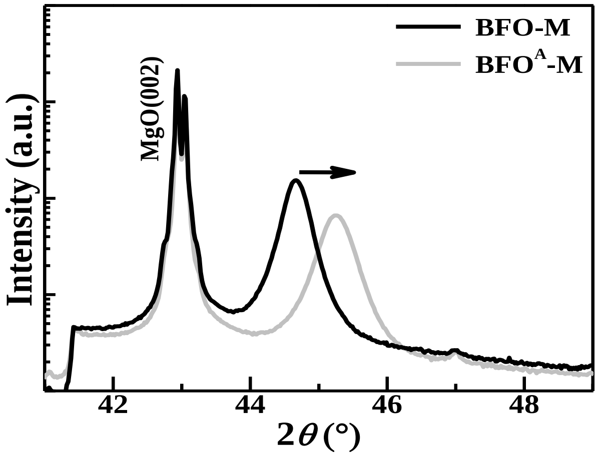

Figure 3.5: XRD peak (002) of BFO-M and BFO^A-M. The arrow shows a shift in the peak of annealed film.

To decrease oxygen vacancies, BFO-M film was annealed in flowing oxygen at 900^o*C* for 24 *hrs*. A previous study shows that oxygen annealing of BFO film at 900°*C* shows largely enhanced magnetization at room-temperature [13]. Heating for a long duration ensures reduced oxygen vacancies with 3-δ → 3, but causes structural changes too. After this annealing, no extra XRD peak was observed. All the XRD peaks shift to higher 2θ after oxygen annealing, showing a different lattice constant of the BFO^A-M film. A typical shift of *(002)* XRD peak is shown in Figure 3.5.

This shift indicates a decrease in out-of-plane lattice parameter from 4.053 Å in BFO-M to 4.005 Å in BFO^A-M film. The oxygen annealing transforms Fe^{3+} ions to Fe^{4+} ions to neutralize the charge in BFO^A-M film. The size of Fe^{3+} (0.65 Å) is larger than that of Fe^{4+} (0.59 Å) [15], which causes a change in the lattice parameters of the film. The shrinking lattice parameter of oxygen annealed BFO films has been reported earlier for films deposited on other substrates too [11]. Therefore, this shifting of XRD peak is not substrate-dependent effect. Different lattice constants of BFO-M and BFO^A-M films suggest that these two films have different pseudocubic structures [11, 13]. On the other hand, a smaller lattice constant of BFO^A-M signifies larger tensile strain after oxygen annealing. To further investigate the effect of oxygen annealing on the in-plane lattice parameters of the film, we recorded Reciprocal Space Maps (RSMs) of these films about *(311)* peak (Figure 3.6). We find that the in-plane parameters of BFO^A-M film are smaller than those of BFO-M film. The decrease in all three lattice parameters indicate a decrease in unit cell volume, which further suggests that the tensile strain has increased in all three crystallographic directions after oxygen annealing. RSMs indicate an incoherent strain in these films (Figure 3.6).

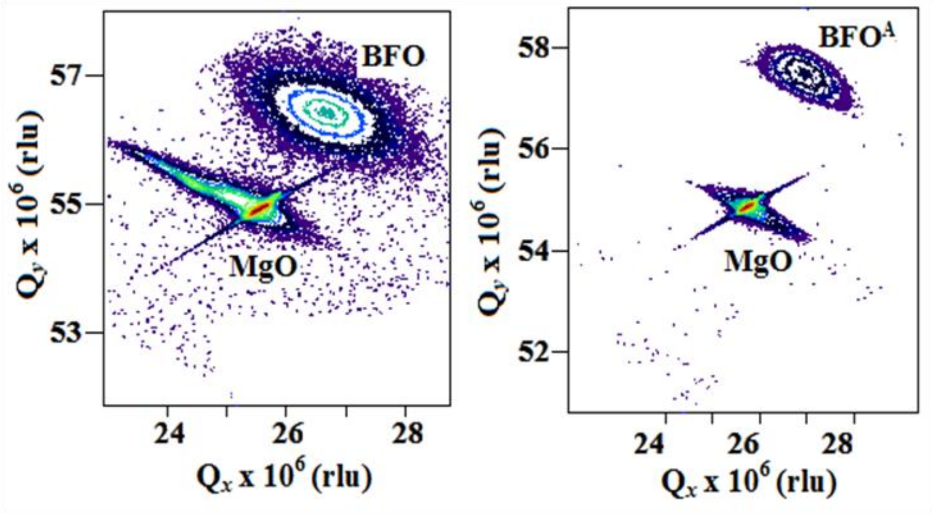

Figure 3.6**: *RSMs of BFO-M and BFO^A-M films around (311) peak.***

Figure 3.7 shows the surface morphology of these films recorded using Atomic Force Microscopy (AFM). A self-organized growth of square structures is clearly visible on the surface of BFO-M. All the squares are symmetric and aligned in the same crystallographic direction. In other words, all the edges of the square are found to be aligned parallel.

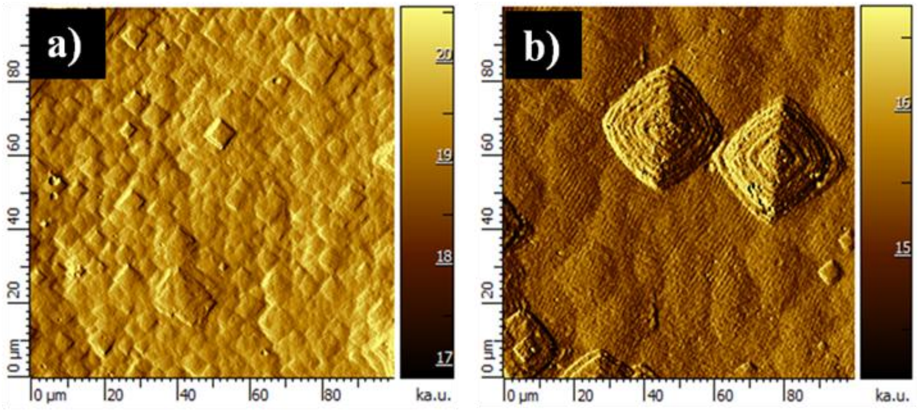

Figure 3.7**: *AFM image of a) BFO-M b) BFO^A-M thin films*.**

In addition, the symmetry of the squares is maintained in grains varying in size from a few micrometers to tens of micrometers of the scale. However, it is important to note that after annealing, these squares grow tremendously and yet symmetrically in size without deforming the square-geometry in BFO^A-M. In addition, we also observed growth of symmetric pyramid-type of structures in BFO^A-M. This growth exhibits the characteristic of BFO to develop symmetric structures in form of squares along the two dimensional surface on MgO *(001)*. The symmetric growth also effectively continued in the third dimension along the thickness in form of pyramids, where the stacking of the squares is visible in Figure 3.7. The average grain size has increased by 5.4 times in BFO^{A}–M film as compared to that in BFO-M film.

Figure 3.8 shows ZFC and FC magnetization versus temperature plots of BFO^{A}-M film. A slightly larger separation between ZFC-FC curves (Figure 3.8) of BFO^{A}-M than that of BFO-M indicates increased short-range magnetic interactions. A small hump appears above 200 K, which marks the onset of competing magnetic interactions (inset Figure 3.8). No such transition was visible in BFO-M film. Below this onset temperature, there is an increased separation between ZFC-FC curves.

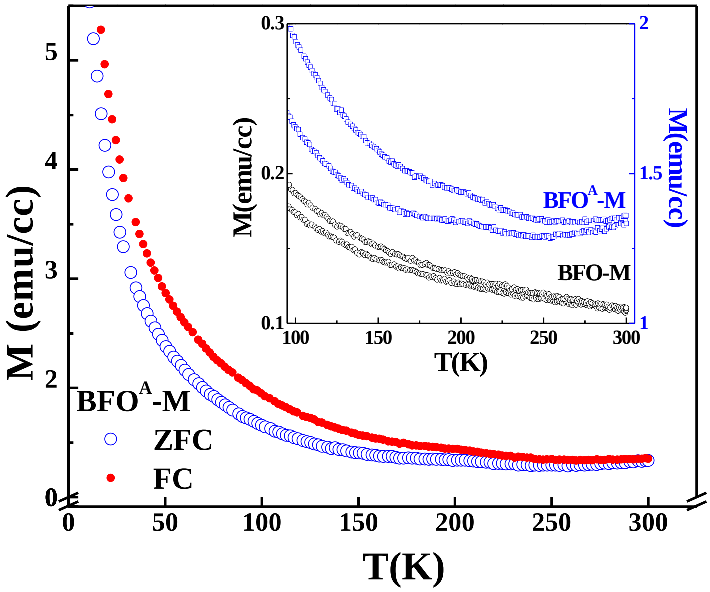

***Figure 3.8**: ZFC and FC magnetization curves of BFO^{A}-M at H= 500 Oe. The inset figure shows magnified region from 100 K to 300 K.*

Figure 3.9*a* & *b* show magnetization versus magnetic field (M-H) isotherms at 300 *K* and 20 *K* respectively. The annealed film shows an enhanced magnetization at room temperature as well as at low temperature. The magnetic hysteresis of BFO^A–M shows five-times increase in coercivity as compared to those of BFO-M film. Basically the oxygen annealing increases the oxygen content in the film, which causes replacement of Fe^{3+} ions with Fe^{4+} ions. By the Kanamori-Goodenough superexchange interaction rules, since Fe^{3+} has half filled d-orbitals (d^5),

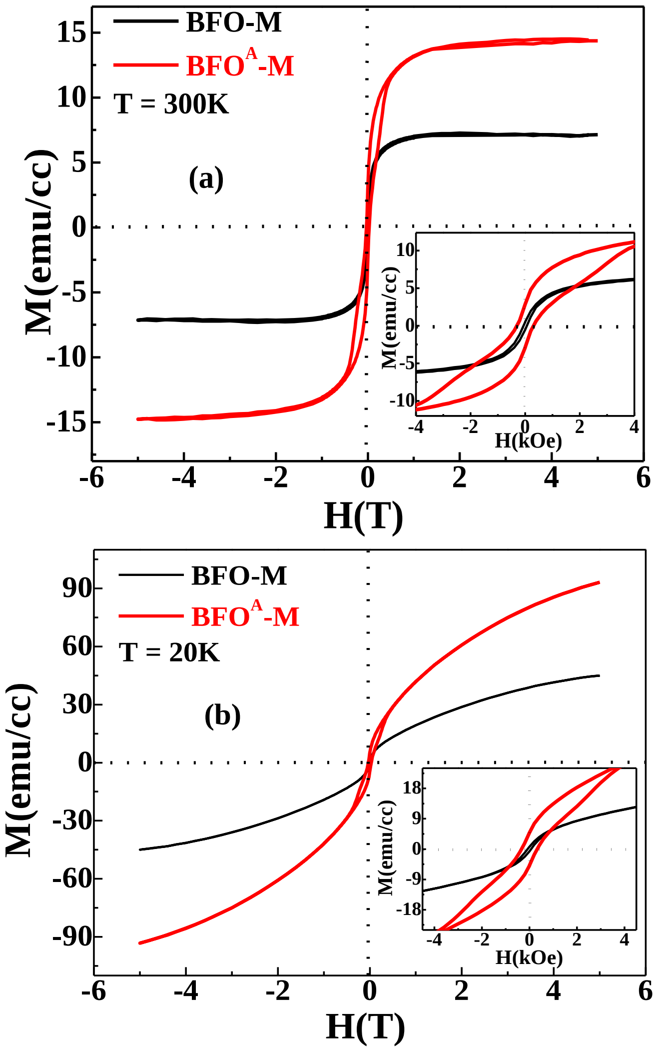

***Figure 3.9**: Magnetization versus magnetic field isotherm of BFO-M and BFO^A-M films at a) 300 K b) 20 K. The inset shows the same plots on a larger scale.*

the Fe^{3+}-O-Fe^{3+} superexchange interactions are antiferromagnetic while the Fe^{4+}-O-Fe^{4+} exchange interactions are ferromagnetic with Fe4+ having less than half filled d-orbitals (d^4). Therefore, the presence of larger content of Fe^{4+} ions causes an enhanced magnetization. The decreased unit cell volume also confirms that Fe^{4+} content has increased. M-H isotherm of BFO-M film shows saturation of magnetization at 300 K, which clearly indicates weak ferromagnetic state (Figure 3.9*a*). However, the BFO^A-M film shows annealing-induced magnetic anisotropy in M-H hysteresis loop at 300 K, *i.e.*, the magnetization saturates at higher magnetic fields and the coercivity enhances. The applied magnetic field needs to exert a larger force to overcome anisotropic energy BFO^A-M film at 300 K.

After oxygen annealing, a feature like pinching of ferromagnetic hysteresis manifests for BFO^A-M film as shown in Figure 3.9*a & b*. Such features appear due to anisotropy or coexisting soft and hard ferromagnetic phases [16-21].

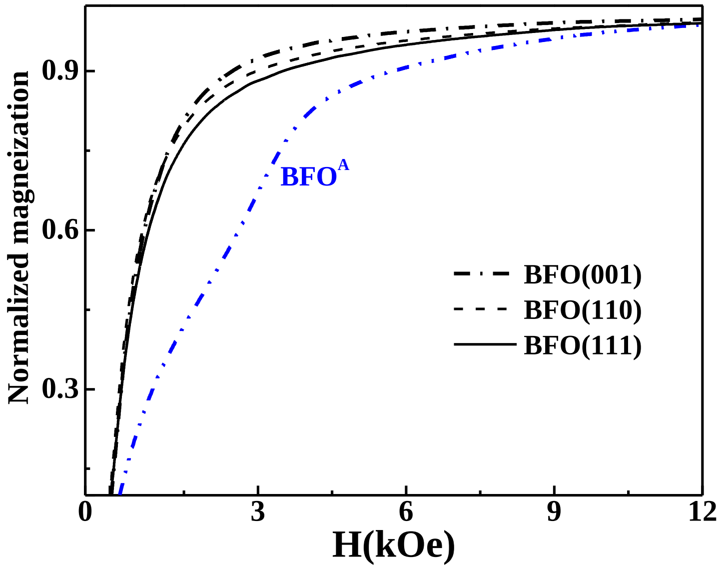

***Figure 3.10**: The normalized first curves of magnetization isotherms of BFO (001), (110), (111) and BFO^A-M at 300 K.*

To further investigate these features of isotherms in detail, we made another three films of BFO on three MgO substrates with different crystallographic orientations: *(001)*, *(110)* and *(111)*. It should be noted that these three films are deposited simultaneously to ensure similar growth. For a qualitative comparison, Figure 3.10 shows the normalized magnetization versus magnetic field plots for all three films at room temperature. It can be observed from this figure that the film with *(111)* orientation requires highest magnetic energy to achieve saturation of magnetization whereas the film with *(001)* orientation needs lowest magnetic energy. This is because the *(111)* axis of BFO is hard-axis of magnetization. Thus, BFO films have inherent magnetocrystalline anisotropy, which was previously observed on other substrates too [11].

However, the comparison is qualitative (*i.e.* magnetization is normalized) and the opening of the loop is quite larger for BFO^A/MgO *(001)* films than that observed due to magnetocrystalline anisotropy only, in BFO/MgO *(111)* film. The qualitatively compared hystereses show that the opening cannot be just because of magnetocrystalline anisotropy in BFO^A film, but there is an additional contribution to this opening. As mentioned earlier, pinching of hysteresis loops in thin films may also appear due to coexisting ferromagnetic phases [17]. The BFO compounds have tendency to show several structural transformations depending on changes in the oxygen stoichiometry [6]. As $\delta \rightarrow 0$, the structure of film changes in order to accommodate extra oxygen ions and the reduced size of Fe ions (Fe^{3+} converts to Fe^{4+}). This process enhances the in-plane strain quite largely in the film as explained earlier. This enhanced strain not only causes anisotropy, but also a larger surface roughness in the film, both of which can induce a hard (or less soft) magnetic phase coexisting with already present soft magnetic phase. To confirm coexistence of two magnetic phases, we plot *dM/dH* versus H as shown in Figure 3.11. It helps us identify two peaks in *dM/dH* of BFO^A film. This feature indicates different saturation of magnetization of two magnetic phases. The pinching of M versus H loop (Figure 3.9) also suggests two different coercive fields of one soft and another hard (less soft) magnetic phases.

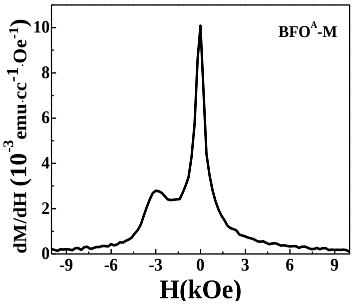

Figure 3.11*: *dM/dH versus H plot of BFO^A-M film at 300 K.

The *dM/dH* plot of untreated BFO-M film does not show such feature. This feature is arising as a result of oxygen annealing. Thus the pinching of hysteresis is a mixed contribution from magnetocrystalline anisotropy and newly evolved hard magnetic phase in coexistence with a soft magnetic phase. An incoherent distribution of strain would augment the existing magnetocrystalline anisotropy. This is also apparent from Figure 3.10 as magnetization of BFO^A-M does not saturate till high magnetic fields. The local structural differences would cause soft/hard magnetic regions as well. An amalgamation of these two phenomena plausibly results in the pinched hysteresis curve obtained for BFO^A-M and saturation of magnetization at higher magnetic fields in comparison to that of BFO-M film. The magnetic properties of this film will be discussed in comparison to other films at later stages.

The resistivity measurements were performed on BFO-M and BFO^A-M films over the range of 300 *K* to 7 *K*. In both cases the resistivity was found so high that the values were beyond measurable limit of our instrument (Keithley made model: 2612A). Unlike the earlier report [13] of BFO films becoming highly conducting on annealing, we found that these annealed films on MgO remain highly insulating at all temperatures.

To further understand the magnetism of BFO system at room-temperature, we have performed Magnetic Field Microscopy (MFM) on BFO and BFO^A-M films at room temperature (Figure 3.12). These images were captured after recording the magnetic hysteresis at high magnetic fields at room temperature. Thus, the samples were already exposed to high magnetic fields before MFM recording. However, during recording of MFM images, no magnetic field was applied (limitation of our instrument). Therefore the MFM images reflect the magnetic domain arrangement of remanent magnetization at 300 *K*. BFO^{A}-M film shows higher contrast and clearer pattern of the domains at room temperature. The largely enhanced magnetization produces well-defined domain patterns with a larger remanence of magnetic hysteresis (Figure 3.9).

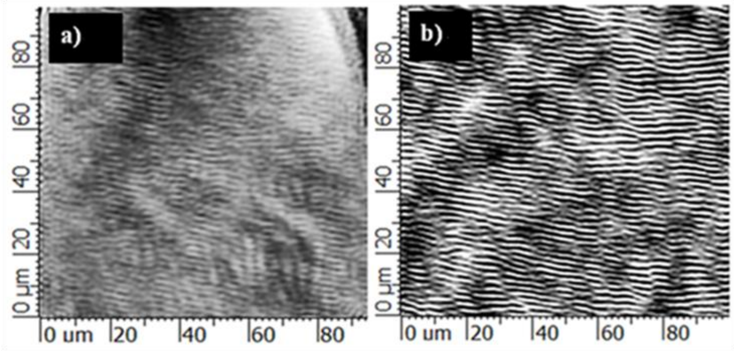

Figure 3.12*: *MFM images over 100 µm × 100 µm area of a) BFO-M and b) BFO^{A}-M films at 300 K.

3.3.4 BaFe$_{0.9}$Ti$_{0.1}$O$_{3-\delta}$ Thin Film Deposited on MgO *(001)*

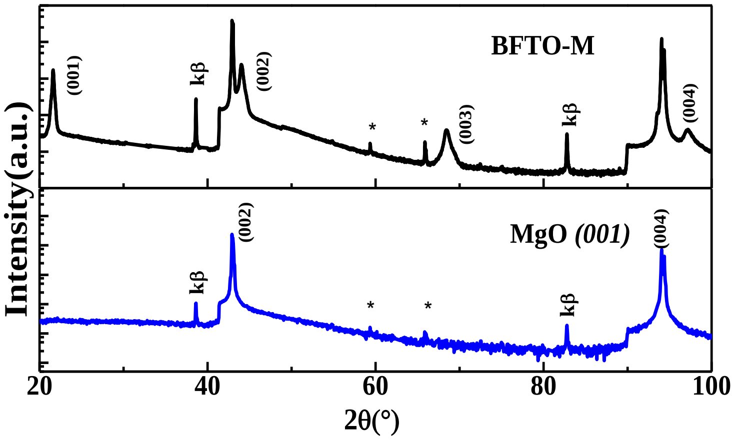

Figure 3.13*: *XRD pattern of BFTO-M thin film. The XRD pattern of MgO substrate is shown (bottom panel) in order to show that some extra reflections that appear in film, basically originate from MgO substrate on which the film is deposited.

In this section, we discuss the results of 10% Ti-doped thin films of BFO deposited on MgO *(001)*. The film formed was free of any impurity and oriented along the crystallographic planes of MgO *(001)* (Figure 3.13).

Figure 3.14 shows ZFC and FC magnetization versus temperature plots for the BFTO-M film. The ZFC-FC curves show clear bifurcation indicating larger magnetic frustration and enhanced magnetization. These curves remain largely separated till 350 *K*. As the measurements were recorded starting from 350 *K*, this feature indicates that the short-range ferromagnetic correlations originate at higher temperature than 350 *K*. The Ti being a strong oxidizing ion when doped in BFO should acquire a stable stoichiometry by holding the oxygen to the lattice structure. This in turn may help stabilize Fe in 4+ valence state, and consequently, the ferromagnetic interactions will increase.

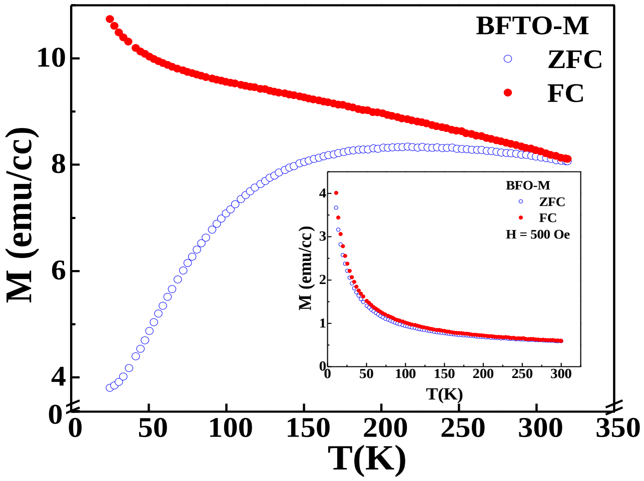

***Figure 3.14**: ZFC and FC magnetization curves of BFTO-M film. The inset shows ZFC and FC magnetization curves of BFO-M for comparison.*

Figure 3.15*a* shows a comparison of the magnetic hysteresis of BFO and BFTO films at room temperature. The BFTO film shows almost two times larger value of saturation magnetization as compared to that of

BFO film at 300 *K*. The Ti^{4+} is a nonmagnetic ion with $3d^0$ orbital. As mentioned earlier, the Zr^{4+} doping (with $4d^0$ orbital) helps stabilize the oxygen stoichiometry in the BFO. Similarly, Ti^{4+} also stabilizes the tetravalent state of Fe and thereby fosters the ferromagnetic Fe^{4+}-O-Fe^{4+} interactions at room temperature. Such enhancement of magnetization after doping non-magnetic ions at Fe-site is observed only in case of thin films of BFO (*i.e.* in cubic/tetragonal structure), but barium ferrites tend to show a decrease in the magnetization after Ti-doping in hexagonal structural symmetry in bulk form [23]. Most plausible explanation is given as follows. As the oxygen stoichiometry is complete ($\delta \approx 0$) in hexagonal structure, there is no further enhancement in oxygen stoichiometry by Ti-doping and, therefore, the doping by nonmagnetic Ti ions causes reduction in the magnetization. The thin films of BFO tend to get oxygen deficiencies by accommodating ions to a different and strained thin structure than the hexagonal bulk structure. Thus, Ti-doping helps stabilize the oxygen stoichiometry in thin films and thereby enhances magnetization.

Now this enhancement in saturation magnetization by 10% Ti-doping is quite large. The non-magnetic ions like Ti^{4+} are expected to dilute the magnetization. In contrast, this substitution enhances ferromagnetism of BFO quite effectively. On comparing the enhancement in magnetization by Ti-doping and by oxygen annealing of BFO, it is clear that Ti-doping is much more efficient in enhancing the magnetization (compare Figures 3.9 and 3.15). This means that Ti-doping not only stabilizes oxygen in BFO (which is also done by oxygen annealing), but it also causes additional effects. Such a huge enhancement of magnetic moment by 10% Ti-doping is most probably realized by enhanced Fe-spins interactions, in addition to stabilizing the oxygen stoichiometry, as explained below.

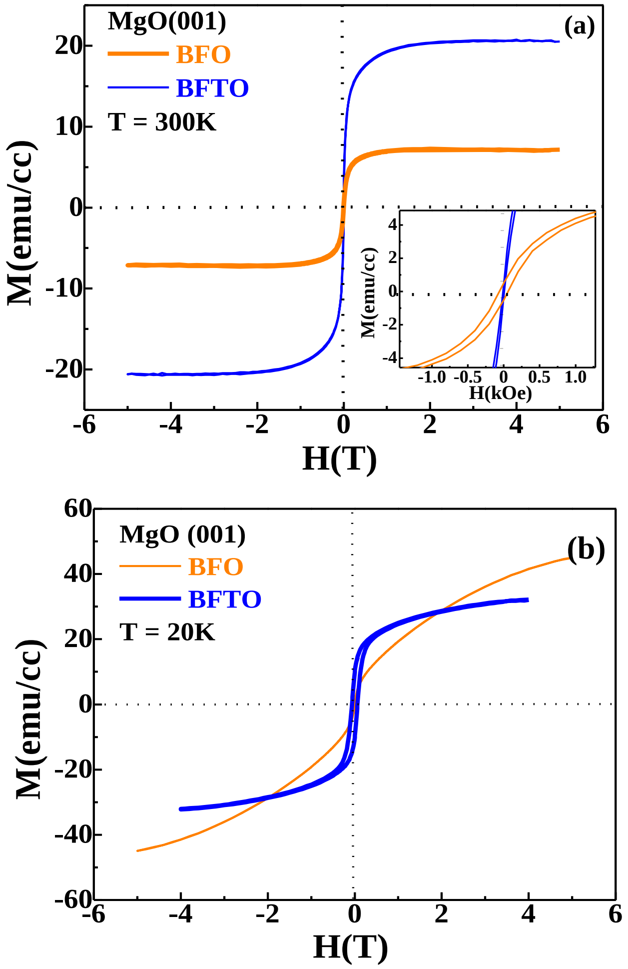

Figure 3.15*: *Comparison of magnetization versus magnetic field isotherms of BFTO-M and BFO-M at a) 300 K and b) 20 K.

BFO has a weak ferromagnetic state at all the temperatures. Thus, the magnetic spins have short-range magnetic interactions, which never achieve full/large ferromagnetic moment of magnetic Fe-sublattice. Let us also note that the ionic size of Ti^{4+} (0.61 Ǻ) is less than that of Fe^{3+} (0.65 Ǻ). Thus, when Ti replaces Fe at B-site, it can create local distortions by tilting the octahedra [24] which may lead to change in the structure and creates a cation disorder at magnetic B-site. In addition, the non-magnetic ions like Ti can also induce a magnetic disorder and produces a vacant slot (zero spin) randomly in the spin-lattice of Fe ions. Such vacant slots in weak ferromagnetic spin-structure can effectively change the exchange interactions and, thus, change the magnetization. This is in addition to the enhancement caused by increasing tetravalent Fe ions due to stable oxygen stoichiometry. Ti ion being a non-magnetic neighborhood in the surroundings of magnetic Fe ions, does not cancel the magnetic contribution of Fe-lattice but help change the degree of canting/exchange of the spins in surroundings in a way that enhances the magnetization. Thus, Ti-doping adds two factors in BFO films: i) structural and cation disorder and ii) modified magnetic interactions. Unexpectedly large influence of Ti-doping suggests that the magnetic ground state of BFO system has a delicate stability and if disrupted by structural-, magnetic- or strain-induced changes, may exhibit large changes in the magnetization and magnetic behavior.

In a similar case, a weak ferromagnetic order was induced by Ti-doping in non-magnetic $CaRuO_3$ [24]. Also, an enhancement of magnetic moment in $CaRuO_3$ has been observed by Cr-doping [25, 26]

3.3.5 Oxygen Annealing of $BaFe_{0.9}Ti_{0.1}O_{3-\delta}$ Thin Film Deposited on MgO *(001)*

Oxygen annealing of $BaFe_{0.9}Ti_{0.1}O_{3-\delta}$ thin film causes a structural transition in the film (Figure 3.16). We have also observed minor XRD peaks related to *(100)* and *(010)* structural orientations in addition to already existing *(001)* XRD peak as shown. This feature, in addition to shifting of all the XRD peaks, indicates a structural transition of the film from tetragonal to orthorhombic symmetry. As $\delta \rightarrow 0$, BFO has a tendency to acquire a hexagonal structural symmetry. However, in case of thin films, the lattice does not have degrees of freedom to acquire a complete hexagonal symmetry; rather such changes in δ produce a strained structure. In addition, Ti^{4+} is a smaller ion than Fe^{3+}. Therefore, this replacement of Fe^{3+} by Ti^{4+} causes local structural distortions. Moreover, oxygen annealing also contributes to large structural changes and greater strain on MgO to accommodate structural and stoichiometric changes in BFTO^A-M film and therefore the structure of Ti-doped film goes through a transformation.

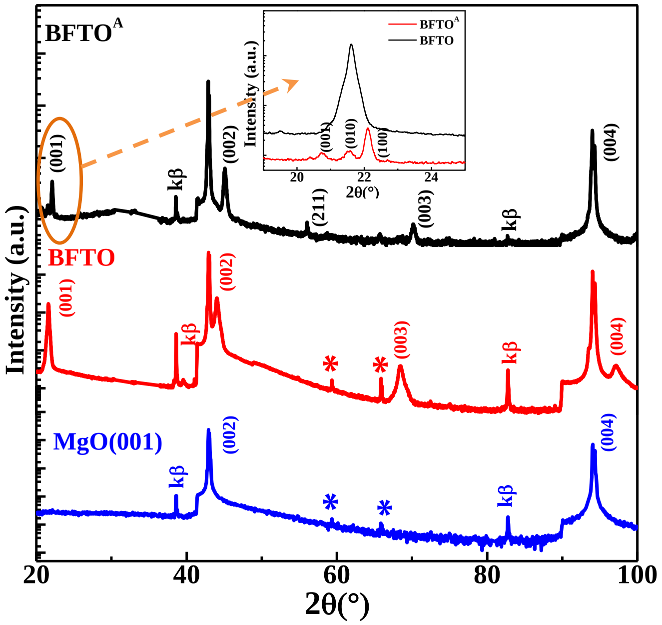

Figure 3.16: *XRD pattern of BFTO-M and BFTO^A-M.*

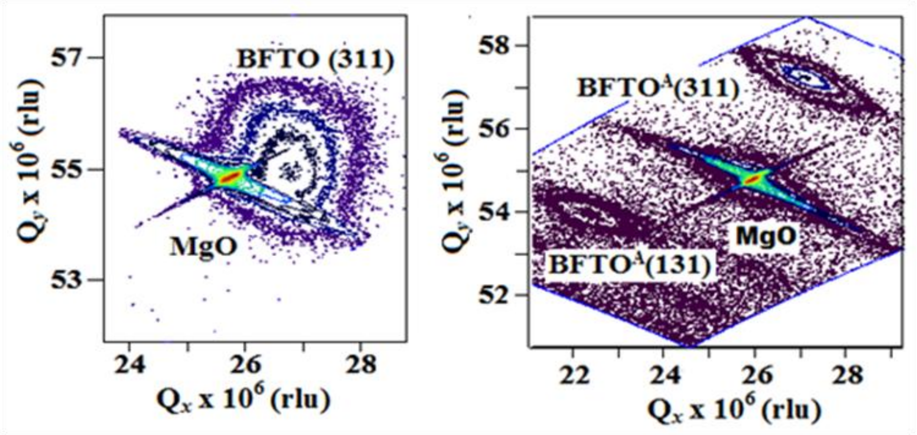

Figure 3.17: *RSMs of BFTO-M and BFTO^A-M films around (311) peak.*

The RSM images of BFTO-M and BFTO^A-M were obtained to study the in-plane geometry of the films (Figure 3.17). The calculations of out-plane (c = 4.111 Å) and in-plane (a = 4.028 Å) lattice parameters of BFTO-M film show that it clearly acquires tetragonal symmetry. RSM of BFTO^A-M shows two peaks with different in-plane orientations. These extra peaks corroborate the earlier observation of structural transformation from tetragonal to orthorhombic phase in BFTO^A film. Due to this structural transition, the film has multiple structural orientations.

After oxygen annealing, average grain size of BFTO^A-M increases by about four times of that in BFTO-M (Figure 3.18). On annealing, as opposed to the undoped BFO^A film, the Ti-doped film shows different magnetic behavior at room temperature and lower temperatures, as described in the following paragraphs.

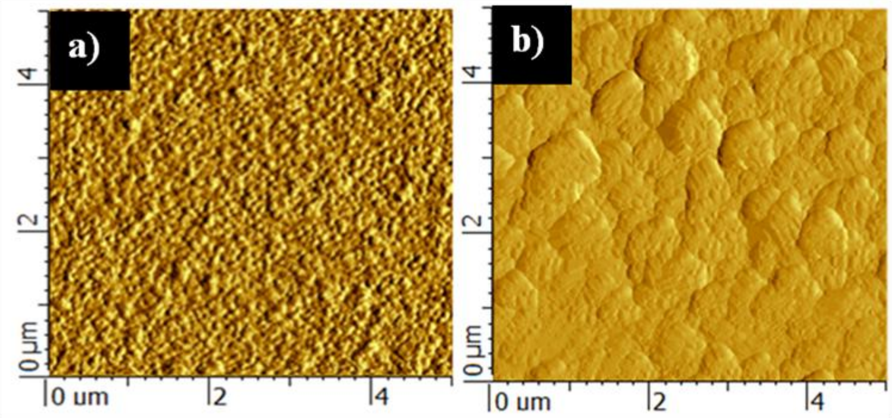

***Figure 3.18**: AFM images a) BFTO c) BFTO^A thin films deposited on MgO (001).*

The influence of annealing on Ti-doped film can be understood from temperature-dependent ZFC-FC magnetization curves (Figure 3.19), which shows smaller separation in ZFC and FC magnetization curves after annealing. The ferromagnetic ordering which was very pronounced in BFTO-M, diminished in

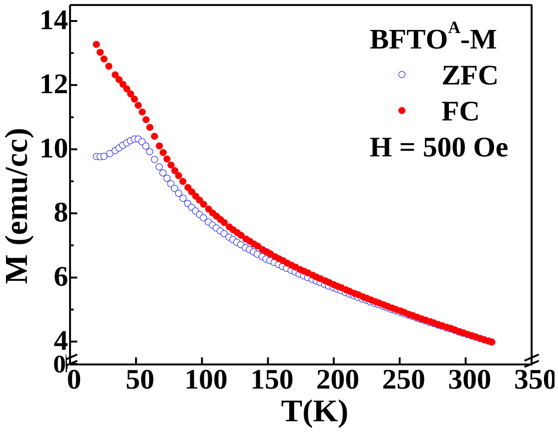

***Figure 3.19**: ZFC and FC magnetization curves of BFTO^A-M at 500 Oe.*

BFTO^A-M although a weak ferromagnetic content remains. At low temperatures a competing magnetic state prevails as indicated by a large separation in ZFC and FC magnetization. These changes in magnetic properties take place due to the structural transition of BFTO^A-M upon annealing.

Magnetic hysteresis at 300 *K*

Figure 3.20 shows a comparison of the magnetic hysteresis of BFTO-M and BFTO^A-M films at 300 *K*. There is a contrast in the features of both the annealed films (BFTO^A and BFO^A): *a)* the magnetization of BFTO^A decreases after oxygen annealing in contrast to enhanced magnetization of BFO^A film and *b)* the opening of magnetic hysteresis loop is negligibly small and qualitatively different for BFTO^A film (inset Figure 3.20) compared to apparently open hysteresis loop of BFO^A (Figure 3.9). These results can be explained as follows. As mentioned earlier, BFO^A film develops a hard magnetic phase and magnetocrystalline anisotropy, which also results into larger coercivity of magnetic hysteresis. In addition, it shows enhanced magnetization due to presence of larger

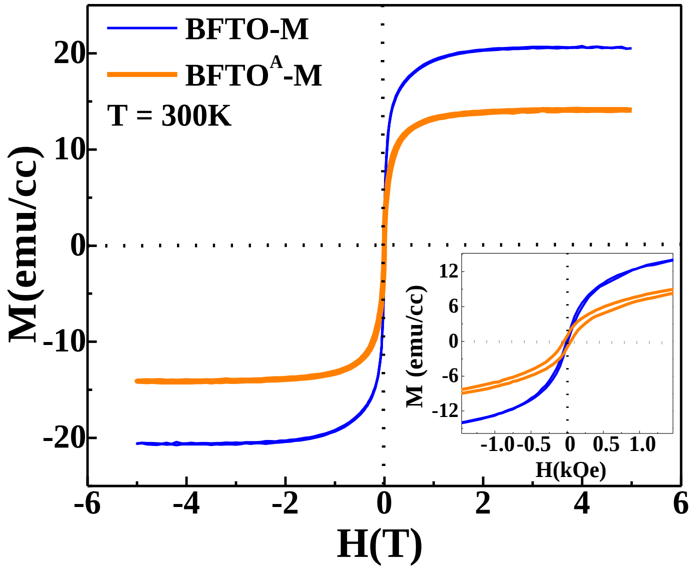

Figure 3.20*: *Magnetization versus magnetic field isotherm of BFTO-M and BFTO^A-M films at 300 K.

number of Fe^{4+} ions. In case of $BFTO^A$ film, as $\delta \rightarrow 0$, the structural transformation takes place. This induces strain in the structure, which augments the already present magnetocrystalline anisotropy in the system. In addition, the enhanced strain in $BFTO^A$ film contributes to the magnetocrystalline anisotropy and opening of the loop. This can be seen in Figure 3.21 that the magnitude of magnetocrystalline anisotropy is enhanced in $BFTO^A$-M when compared to the other three orientations. The saturation occurs at much higher fields.

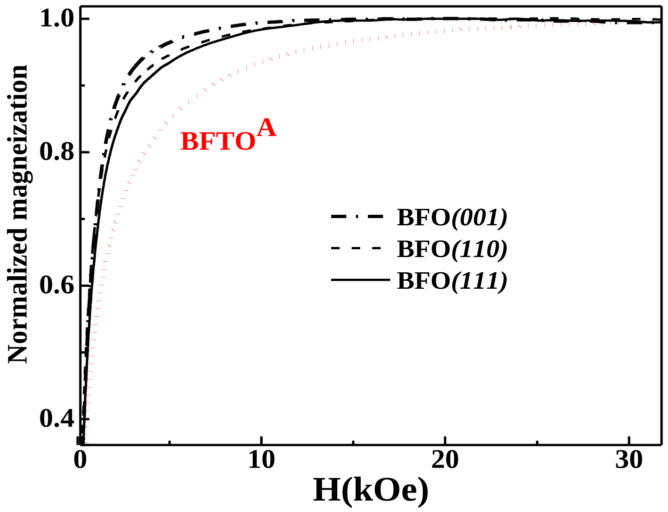

***Figure 3.21*: The normalized first curves of BFO (001), (110), (111) and $BFTO^A$-M.**

However, the opening of loop or coercivity is minor in $BFTO^A$ film compared to that in BFO^A film. This is because there is no development of hard magnetic phase in the former. The absence of hard magnetic phase may be confirmed by *dM/dH* vs. H curves of $BFTO^A$ films in Figure 3.22.

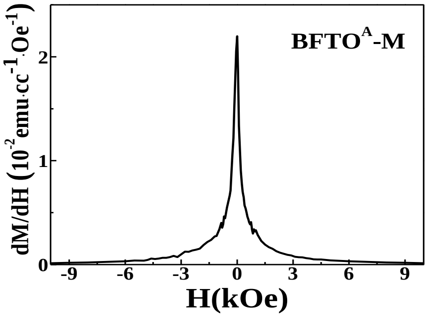

***Figure 3.22*: dM/dH versus H plot of $BFTO^A$-M at 300 K.**

The structural transition after oxygen annealing causes a minor decrease in magnetization of $BFTO^A$ film at 300 *K* (Figure 3.20). It should be noted that BFO^A film develops coexisting magnetic phases (soft and hard), but does not show any structural transition from tetragonal to orthorhombic phase whereas BFTO^A does not develop hard magnetic phase, but shows the structural transition. The Ti-doping actually limits the evolution of hard magnetic phase in BFTO^A film, which was otherwise present in BFO^A film. On the other hand, the same Ti-doping causes structural transformation. Thus, Ti-doping plays a crucial role in determining the structural and magnetic transformations in this series of BFO thin films.

Magnetic hysteresis at 20 K

BFTO^A-M at 20 *K* (Figure 3.23) shows enhanced magnetization in contrast to its behavior at room temperature, where the magnetization decreases. However, the coercivity decreases as compared to the pristine sample confirming that Ti-doping holds the softer magnetic phase in BFO even after oxygen annealing. We have observed that the Ti-doped film does not show surface roughness even after oxygen annealing in contrast to BFO^A-M (Figure 3.18). Therefore, the magnetic coercivity seems to be reducing after oxygen annealing and the soft magnetic phase evolves strongly in BFTO^A-M film with orthorhombic structure and tensile strain.

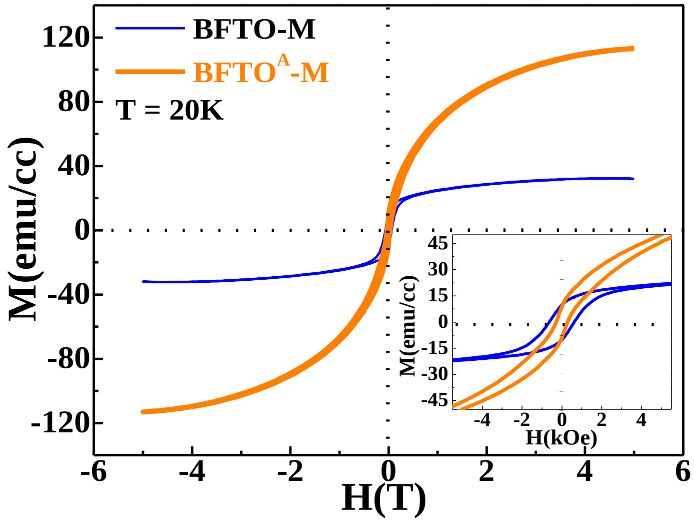

***Figure 3.23*: Magnetization versus magnetic field isotherm of BFTO-M and BFTO^A-M films at 20 K.**

3.3.6 $BaFeO_{3-\delta}$ Thin Film on STO *(001)*

The films deposited on STO experience a compressive strain (Table 3-III). Therefore, these films are expected to show different magnetic behavior compared to the films deposited on MgO.

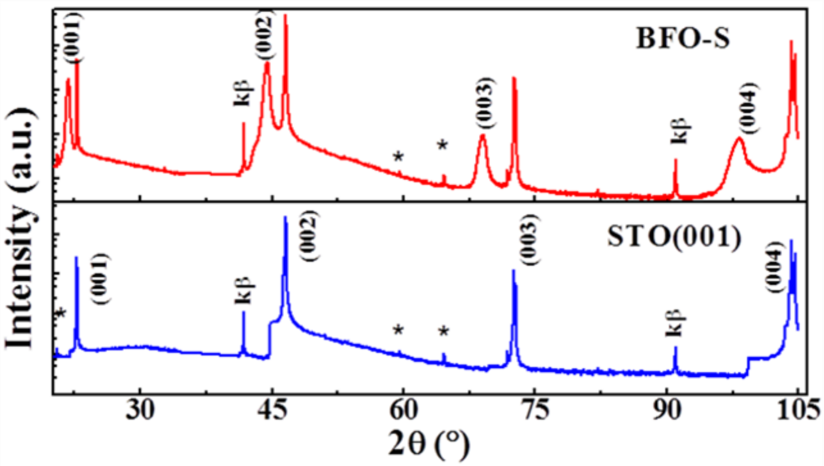

***Figure 3.24**: XRD pattern of BFO-S thin film and STO substrate. The bottom panel shows extra reflections originating from the substrate.*

BFO-S film formed highly oriented on STO substrate (Figure 3.24). All the XRD peaks appear broader as compared to those of BFO-M film, which shows that the films deposited on MgO have better crystalline structure. The structure of BFO-S (a = 4.071Å) has slightly greater out-of-plane parameter than that of BFO-M (a = 4.057Å), due to compressive strain. The out-of-plane parameter elongates and in-plane parameters get compressed if films are deposited on STO.

Figure 3.25 shows magnetization versus temperature curves for BFO-S film. This film shows very large magnetic moment compared that of BFO-M.

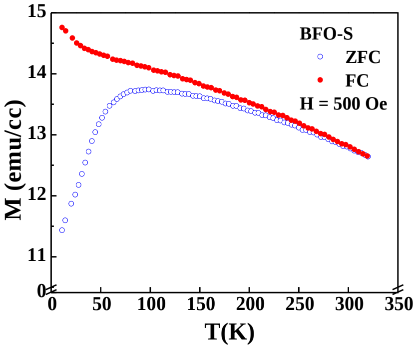

***Figure 3.25**: ZFC and FC magnetization curves of BFO-S film at* **500 Oe.**

Figures 3.26a & b show magnetization isotherms of BFO-S film at 300 K and 10 K, respectively. The film shows soft ferromagnetic behavior at room temperature (Figure 3.26a) with moment much higher than that of the BFO-M film. This large enhancement in magnetization takes place due to compressive strain in BFO-S film whereas BFO-M film has tensile strain. The effect of compressive strain is explained later. Figure 3.26 (b) shows that BFO-S remains soft ferromagnetic down to low temperatures with very small coercivity of ~ 140 Oe. However, the unsaturated magnetic moment in a field of up to 6 T and the quality of magnetic isotherm of BFO-S show that there are competing antiferromagnetic and ferromagnetic interactions at 10 K.

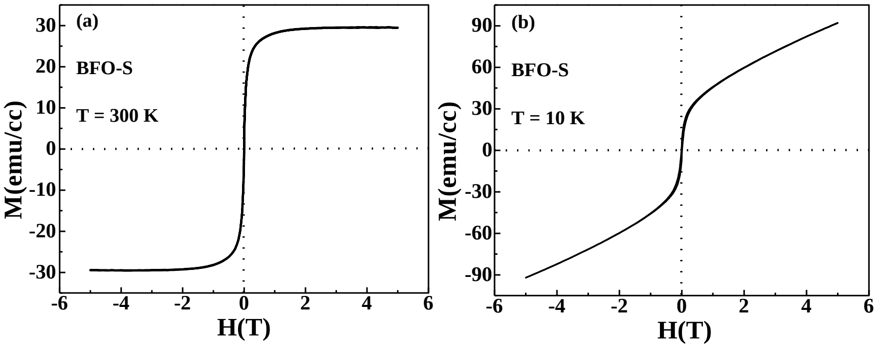

Figure 3.26*: *Magnetization versus magnetic field isotherm of BFO-S at a) 300 K and b) 10 K.

3.3.7 $BaFe_{0.9}Ti_{0.1}O_{3-\delta}$ Thin Film Deposited on STO *(001)*

The Ti-doped films on STO are also highly oriented. However, each of the diffraction peaks in BFTO-S (Figure 3.27, bottom panel) is asymmetric which depicts the presence of dislocations/ disorder in the structures. Figure 3.28 shows the ZFC and FC magnetization versus temperature curves of BFTO-S film. This film has reduced magnetization in the entire temperature range than that of BFO-S, indicating that the short-range ferromagnetic state has, in fact, weakened by Ti-doping.

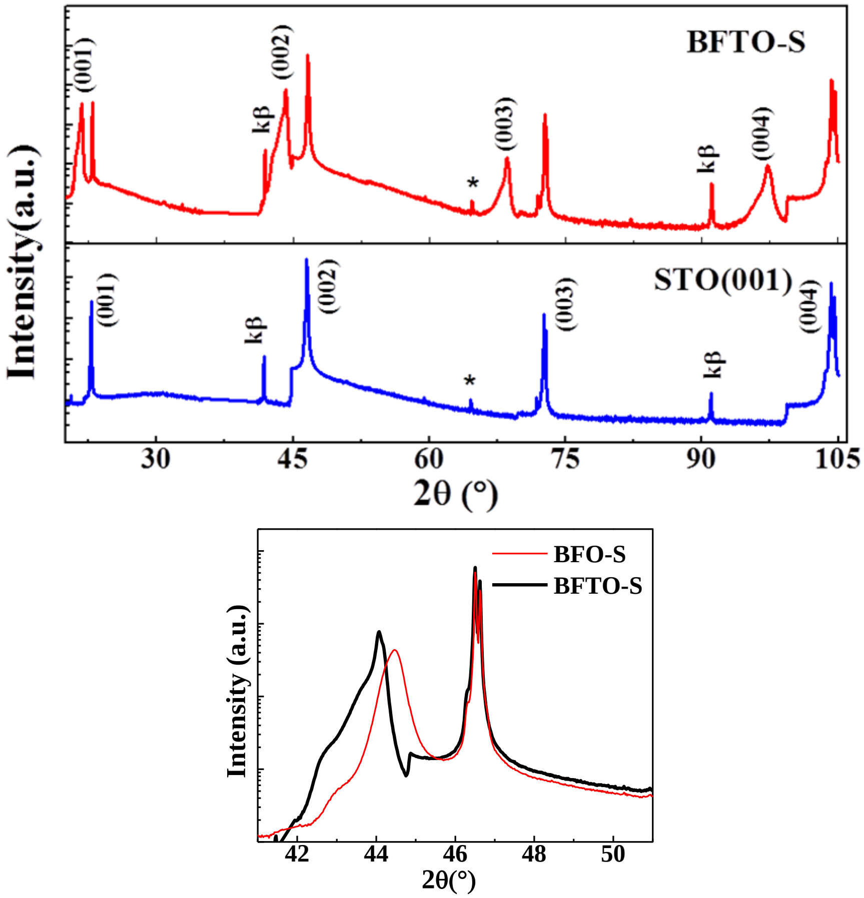

Figure 3.27**: *The upper panel shows the XRD of BFTO-S thin film. Lower panel shows the asymmetric broadening of (002) peak of BFTO-S as compared to BFO-S.***

Figures 3.29 (a & b) show magnetic isotherms of BFO-S and BFTO-S for comparisons. It can be seen clearly that Ti-doping has caused decrease in the magnetization. The magnetic coercivity is slightly higher in BFTO-S film at 300 K and 10 K as compared to that for BFO-S film and the magnetization reduces

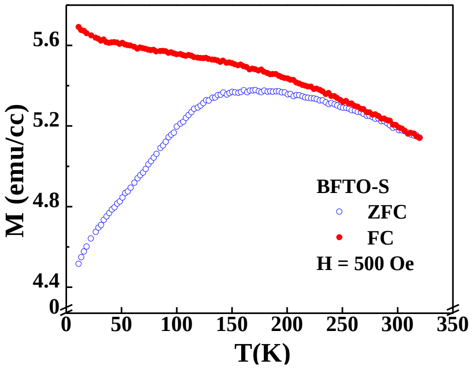

Figure 3.28: ZFC and FC magnetization versus temperature of BFTO-S film at H = 500 Oe.

drastically. As mentioned earlier, the compressive strain largely enhances the magnetization of BFO-S film. The Fe-O-Fe bond length in BFO has been theoretically calculated to be 4.01 Ǻ [27]. Shrinking of lattice by 0.233 Ǻ would result in accommodation of the FeO_6 octahedra to a smaller volume which can lead to reduction of Fe-O-Fe bond length or

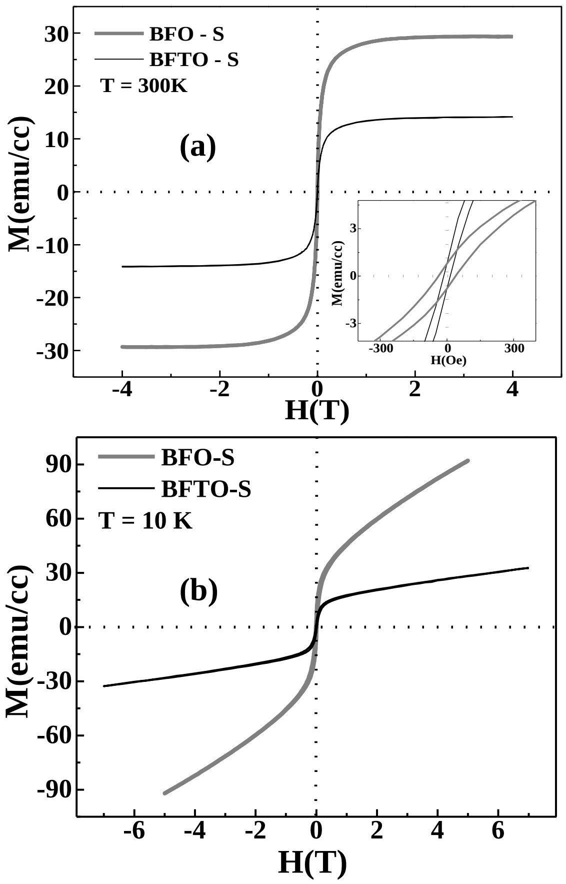

Figure 3.29*: *Magnetization versus magnetic field isotherms of BFO-S and BFTO-S at a) 300 K and b) 10 K.

variation in the Fe-O-Fe bond angle. The enhanced ferromagnetism means the enhanced orbital overlap in Fe-O-Fe bonds. It is very important to note that this enhancement in magnetization is much larger in BFO-S film due to compressive strain, as compared to the enhancement due to Ti-doping in BFTO-M film. The large enhancement further indicates that the oxygen stoichiometry is rather stabilized and the magnetic interactions among Fe ions are stronger due to compressive strain in BFO-S film. The Ti-doping causes disorders and modified magnetic interactions (as explained earlier), which in case of compressive strain, works against ferromagnetic interactions in BFO. Moreover, the XRD peaks for BFTO-S film are found to be asymmetric which causes external structural disorder. This suggests that the compressive strain is more efficient in enhancing ferromagnetic interactions in undoped film and Ti-doping actually dilutes these interactions by inducing various disorders in this series of films with compressive strain. This is in contrast with what was observed in the series of films deposited on MgO with tensile strain.

3.3.8 Oxygen Annealing of $BaFe_{0.9}Ti_{0.1}O_{3-\delta}$ Thin Film on STO *(001)*

Figure 3.30 shows XRD pattern of BFTO-S and BFTO^A-S films together for a comparison. The BFTO^A-S shows a structural transition to orthorhombic symmetry as also observed in case of BFTO^A-M film. All the peaks including extra peaks fit to orthorhombic structure of BFTO^A-S

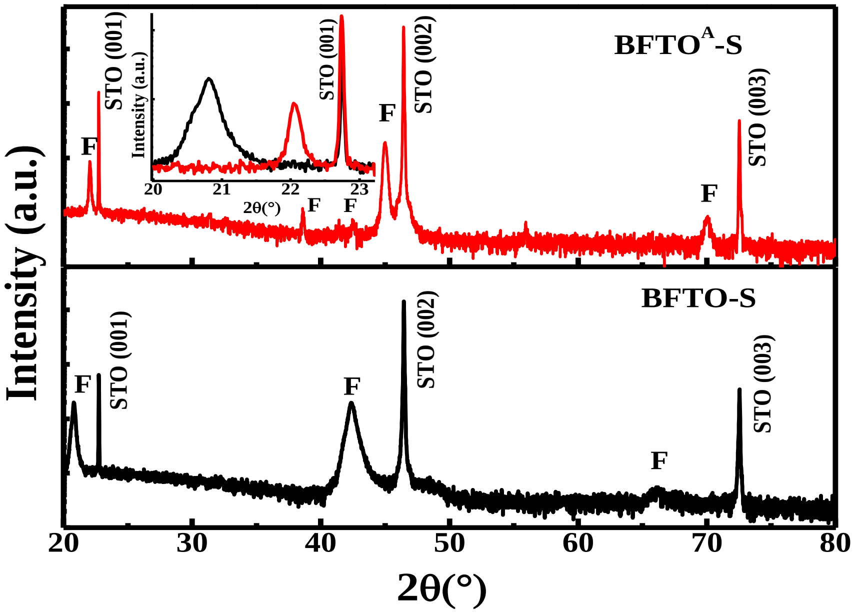

***Figure 3.30**: The XRD patterns of BFTO-S and BFTO^A-S. Inset figure shows typical peak shift in annealed film compared to as-deposited film. All the film peaks are marked by 'F'.*

film. The FWHM of each peak (Figure 3.30) markedly decreased illustrating the improved crystalline quality of annealed film after oxygen annealing. The in-plane parameter of BFTO^A-S also decreased as seen from the RSMs (Figure 3.31). As shown by AFM images in Figure 3.32, the surface roughness of BFTO^A-S film is larger as compared to that of BFTO-S film.

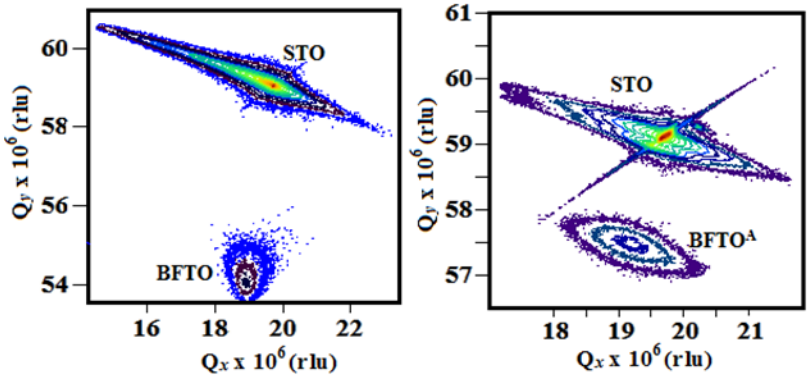

Figure* 3.31: *RSMs of BFTO-S and BFTO^A-S around (311) peak of SrTiO$_3$.

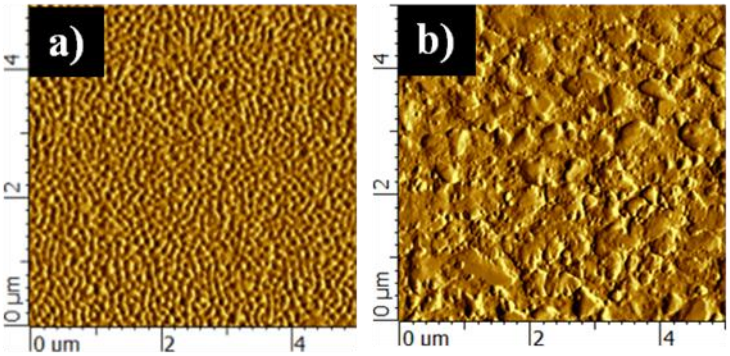

Figure 3.32*: *AFM images of a) BFTO-S b) BFTO^A-S.

Figure 3.33 shows ZFC and FC magnetization curves of BFTO^A-S film. The separation between ZFC and FC curves enhances at low temperature. It can be clearly seen from the Figures 3.33 and 3.28 that the magnetization at low-temperature shows dominatingly competing interactions, whereas the magnetization at room-temperature decreases after oxygen annealing.

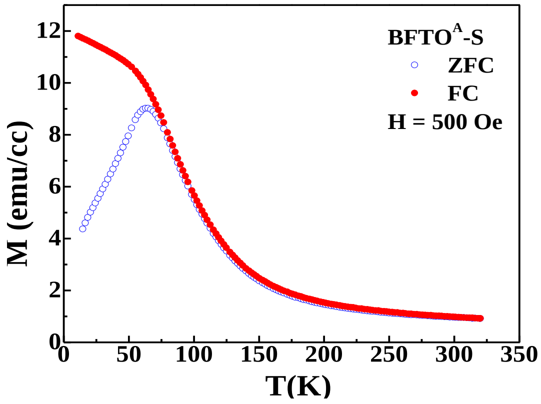

***Figure 3.33**: ZFC and FC magnetization curves of BFTO^A-S film at 500 Oe.*

Figure 3.34 shows magnetization isotherms of BFTO^A-S and BFTO-S films, for comparison. The saturation of magnetization decreases at 300 *K* and a hard magnetic phase dominates even at room-temperature. At 10*K* (Figure 3.34(b)), the magnetization enhanced remarkably with the increase in coercivity (Table IV). In the BFTO^A-S films the hysteresis loop widens to form almost a rectangular shape with a tremendous increase in coercivity (2534 *Oe*) as compared to the un-annealed BFTO-S film (38 *Oe*). The distorted hysteresis loop at 300*K* suggests that the change in magnetic behavior is triggered due to the coexisting soft and hard magnetic phases in BFTO^A-S film. To probe this further, the dM/dH versus H was plotted for the magnetization data at 300*K* (Figure 3.35) it shows the existence of two magnetic phases with different coercivity. This coexistence of magnetic phases might take place due to largely increased surface roughness of the annealed film (Figure 3.32). The changes in magnetic behavior take place because of structural transition after oxygen annealing.

We have observed several similarities and differences in the two BFTO^A films with compressive and tensile strain as listed here:

a) Similarities: i) Both BFTO^A-M and BFTO^A-S films show a structural transition from tetragonal to orthorhombic symmetry due to oxygen annealing, ii) The ZFC and FC magnetization show qualitatively similar behavior with decreased separation at high temperatures and magnetic frustration at low-temperatures, iii) The room-temperature magnetization shows a decrease in both these annealed films as compared to untreated films as observed by magnetic isotherms as well as ZFC-FC magnetization. The decrease in room-temperature magnetization indicates further weakened ferromagnetic interactions.

b) Differences: $BFTO^A$-M shows soft magnetic phase whereas $BFTO^A$-S shows a hard magnetic phase at 300 K and at low temperatures. The hysteresis loop of $BFTO^A$-S also looks distorted at 300 K [Figure 3.34 (a)], which suggests that there are coexisting soft and hard magnetic phases in $BFTO^A$-S film. Figure 3.35 shows dM/dH versus H curve with two peaks. This feature indicates coexisting ferromagnetic phases at room-temperature. The similar coexisting phases have been also observed in BFO^A-M film.

From the above mentioned similarities and differences if $BFTO^A$-M and $BFTO^A$-S films, it is clear that the similarities are taking place due to the structural transition whereas the hard magnetic phase or coexisted phases after oxygen annealing take place because of surface roughness of $BFTO^A$-S film. The surface of $BFTO^A$-M is smooth whereas $BFTO^A$-S and BFO^A-M has larger surface roughness, wherein coexisted magnetic phases (soft and hard) appear after oxygen annealing.

On comparing the combined effects of Ti-doping and oxygen annealing in $BFTO^A$-S (compressive strain) and $BFTO^A$-M films (tensile strain), the effects are very similar (Figure 3.19, 3.20, 3.23, 3.33, 3.34). For instance, both the annealed films show structural transitions, reduced magnetization at 300 *K* and enhanced magnetization at low temperature.

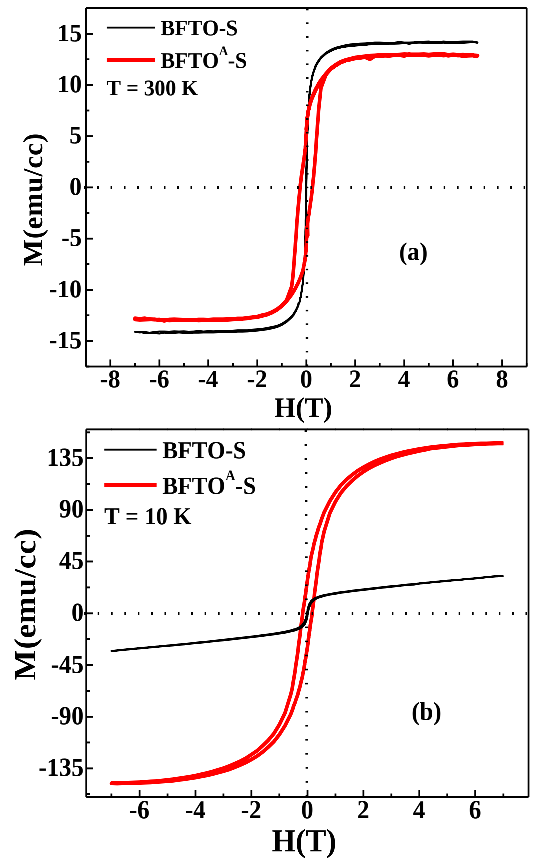

Figure 3.34*: *Magnetization versus magnetic field isotherms of BFTO-S and BFTO^A-S at a) 300 K b) 10K.

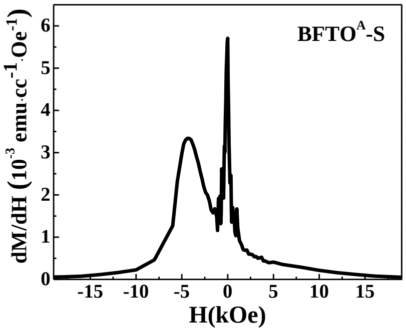

Figure 3.35*: *dM/dH versus H plot of BFTO^A-S at 300 K.

Thus the combined factors of Ti-doping and oxygen annealing cause a structural transition and hence largely influences all the magnetic properties of Ti-doped BFO system; however the effects appear to be molded under the influence of compressive/tensile strain.

3.3.9 Effects of Ru-doping

Ruthenium ions are known to show strong magnetic interactions. Therefore, in order to understand the ferromagnetism in BFO by comparing the effects of non-magnetic Ti-doping with magnetic Ru-doping, we prepared films of $BaFe_{0.9}Ru_{0.1}O_{3-\delta}$ (BFRO).

The results discussed in the earlier portions clearly prove that the strain plays very crucial role in governing the properties of BFO. Under the influence of strain, the doping of a non-magnetic ion (Ti) is found to induce contrasting behavior in BFO depending on the type of the strain. Ti-doping in BFO films enhances the magnetization in the film with tensile strain, while it decreases the magnetization of the film with compressive strain. In the next paragraph, we compare the effects of Ru-doping on BFO Films.

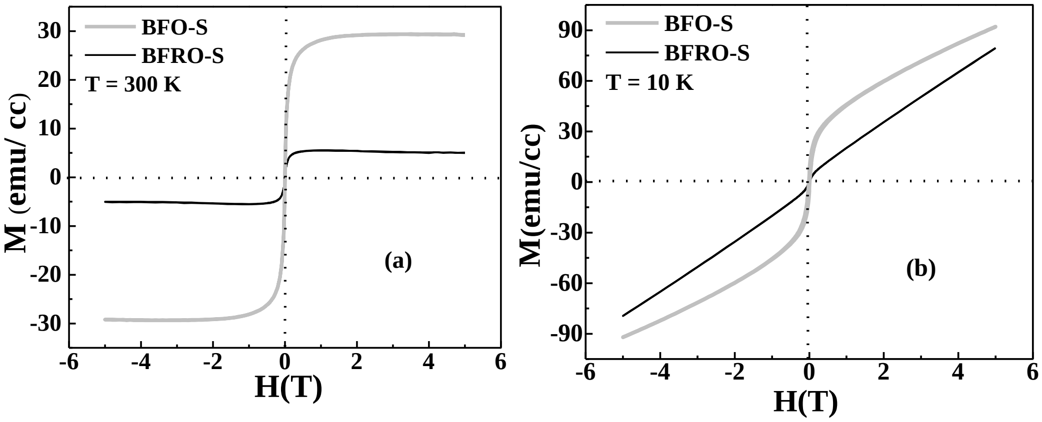

Figure 3.36*: *Magnetization versus magnetic field isotherms of BFO-S and BFRO-S at a) 300 K b) 10K.

Both the BFRO films on MgO and STO substrates are highly oriented. The XRD pattens are similar as typically obtained for Ti-doped films. Figures 3.36 and 3.37 show the magnetization isotherms of BFO and BFRO film deposited on STO and MgO, respectively. Now we compare the magnetic isotherms (3.15, 3.29, 3.36 and 3.37) to show some similarities and differences in the effects of Ti-doping and Ru-doping. As it can be clearly seen, BFRO-S film shows a drastic decrease of magnetization compared to that of BFO-S film indicating suppressed ferromagnetic interactions at 300 *K* (Figure 3.36). The same effect has been earlier observed in case of Ti-doping (Figure 3.29). However, in spite of decreased magnetization of compressive strain thin films after doping Ru/Ti, the saturated magnetization of BFTO-S is nearly double than that of BFRO-S. Also, it can be observed from Figure 3.37, the magnetization of BFRO-M slightly enhanced after Ru-doping in tensile strain films, similarly as observed for Ti-doping in tensile strain films. Again, on comparing BFRO and BFTO films on MgO, Ti-doped film (BFTO-M) show nearly double the saturated magnetization of Ru-doped film (BFRO-M).

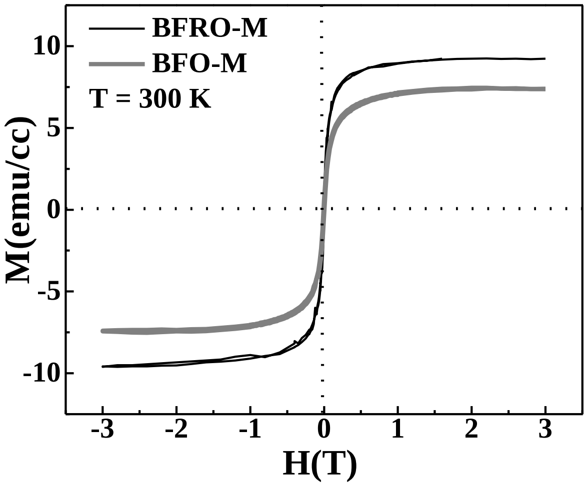

***Figure 3.37*: Magnetization versus magnetic field isotherms of BFO-M and BFRO-M at 300 K.**

Basically there are two parameters working on changing the magnetization of BFO films after doping, i) cation and structural disorder and ii) modified magnetic interactions. The difference in doping-effects can be plausibly explained as follows. Ti ions have tetravalent state. Similarly Ru ions also have tetravalent state in $BaFeO_3$ [28] and therefore, both the dopants equally stabilize the oxygen content of BFO films. It implies that the differences purely arise on magnetic grounds. As per theoretical predictions [28], Ru ions with extended *4d* orbitals have 0.6 to 0.8 μ_B/spin contribution as compared to 3.5μ_B/ Fe ion in a completely ferromagnetic $BaMO_3$ (M=Ru/Fe). Also it is experimentally shown that Fe-O-Ru interactions end up with magnetically frustrated state in hexaferrites due to competing magnetic-exchange-interactions [29]. Thus, Ru ions dilutes the magnetic contribution of Fe-sublattice. In addition, Ru-O bond is less compressible than Fe-O bond, which reduces the effect of strain as per the report.

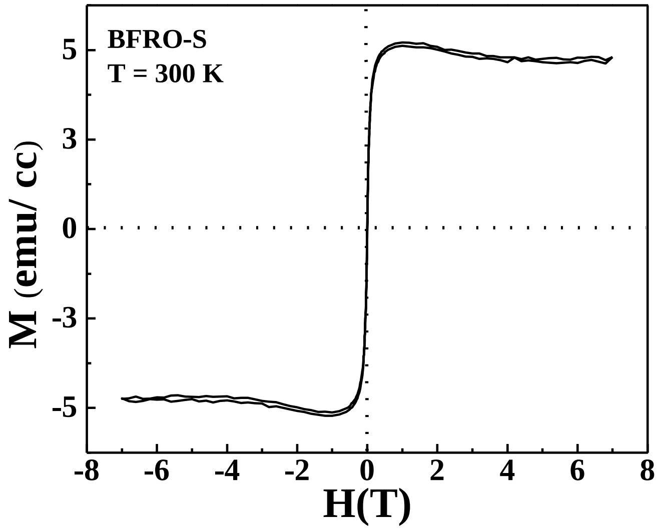

Figure 3.38: Magnetization isotherm of BFRO-S film at 300 K.

Figure 3.38 shows the magnetization isotherm of BFRO-S film at 300 K, on a different scale for clarity of the picture. The saturated magnetization has decreasing slope in Figure 3.38. This shows that magnetic spins of Ru ions align in a way that cancels the saturated magnetization of Fe-sublattice. However, this slope keeps decreasing till high magnetic fields. It means that randomly scattered Ru-ions have no spontaneous alignment of spins at 300 K. However, such slope was not detected in case of another Ru-doped film with tensile strain.

All the above mentioned comparisons show that Ti^{4+} ions induce various disorders without cancelling the magnetic contribution of Fe-sublattice. Ru^{4+} ions induce the disorders, but also dilute the magnetization of Fe-sublattice.

3.4 Conclusions

- Oxygen annealing of BFO films enhances the magnetization and ferromagnetic interactions, but shows coexisting soft and hard magnetic phases. The origin of hard magnetic phase lies in the surface roughness of oxygen annealed films.
- BFO-S shows higher magnetization than that in BFO-M, indicating that the oxygen stoichiometry is rather stable and the ferromagnetic interactions are stronger in BFO film with compressive strain.
- Ti-doping in BFTO-M film enhances the stability of oxygen stoichiometry in BFO films with tensile strain and causes magnetic and cation disorder. Therefore, as a combined effect, Ti-doping largely enhances the magnetization of the film with tensile strain. On contrary, BFTO-S film with compressive strain shows a decrease in the magnetization after Ti-doping. This shows that the magnetic ground state of BFO is delicately balanced. The perturbations through disorder and strain largely influence Fe-O-Fe magnetic exchange interactions.
- $BFTO^A$ films, both with compressive and tensile strains, show similar modifications in structure and magnetism. These similarities show that the combined effects of Ti-doping and oxygen annealing are universal irrespective of the type of the strain in BFO films.
- On comparing the results of BFRO and BFTO films, it is found that the saturation of magnetization is nearly double in magnetic isotherms of BFTO at 300 K, although Ti^{4+} is non-magnetic ions. This difference in the doping effects is plausibly explained as modified magnetic interactions by magnetic Ru-ions.

References

1. P. M. Woodward *et al* (2000), Structural studies of charge disproportionation and magnetic order in $CaFeO_3$, Phys. Rev. B, 62, 844 (doi/10.1103/PhysRevB.62.844).

2. Kawakami T., SaburoNasu S. (2005), High-pressure M¨ossbauer spectroscopy of perovskite high valence iron oxides under external magnetic field, J. Phys.: Condens. Matter 17, S789–S793 (doi:10.1088/0953-8984/17/11/007).
3. Bocquet A. E. *et al* (1992), Electronic structure of SrFe^{+4}O3 and related Fe perovskite oxides, Phys. Rev. B, 45, 1561(doi/10.1103/PhysRevB.45.1561).
4. Kanamaru F. *et al* (1970), Synthesis of new perovskite $CaFeO_3$, Mat. Res. Bull., 5**,** 257-262.
5. Mori S. (1966), Phase Transformation in Barium Orthoferrate, $BaFeO_{3-\delta,}$ J. Amer. Ceram. Soci., 49, 600.
6. Mori S. (1970), Magnetic properties of several phases of Barium orthoferrite $BaFeO_x$, J. Phys. Soci. Japan, 28, 44.
7. Iga F. *et al* (1992), Magnetic and transport properties of $BaFeO_{3-y\,,}$ J. Mag. Mag. Mat., 104-107, 1973 (doi.org/10.1016/0304-8853(92)91628-7).
8. Gil de Muro I. *et al* (2005), Effect of the synthesis conditions on the magnetic and electrical properties of the $BaFeO_{3-x}$ oxide: A metamagnetic behavior, J. Soli. St. Chem., 178, 1712 (doi:10.1016/j.jssc.2005.03.028).
9. Lucchini E., Sbaizero O. (1989), High-temperature conductivity of the hexagonal form of $BaFeO_{3-x}$, J. Mat. Sci. Lett., 8,527-529.
10. Matsui T. *et al* (2002), Structural, dielectric, and magnetic properties of epitaxially grown BaFeO3 thin films on (100) $SrTiO_3$ single-crystal substrates Appl. Phys. Lett., 81, 2764 (doi.org/10.1063/1.1513213).
11. Taketani E., Matsui E. *et al* (2004),Effect of Oxygen Deficiencies on Magnetic Properties of Epitaxial Grown $BaFeO_3$ Thin Films on (100) $SrTiO_3$ Substrates, IEEE Trans. Magn., 40, 2736-2738(doi:10.1109/TMAG.2004.830168).

12. Matsui T., Taketani E., Fujimura N., Ito T., Morii K. (2003), Magnetic properties of highly resistive BaFeO3 thin films epitaxially grown on $SrTiO_3$ single-crystal substrates, J. Appl. Phys., 93, 6993 (doi.org/10.1063/1.1556166).
13. Callender C., Norton D. P., Das R., Hebard A. F., Budai J. D. (2008), Ferromagnetism in pseudocubic $BaFeO_3$ epitaxial films, Appl. Phys. Lett., 92, 012514-3 (doi: 10.1063/1.2832768).
14. Matsui T., Taketani E., Sato R., Morii K. (2007), J. Phys. D: Appl. Phys., 40, 6066 (doi:10.1088/0022-3727/40/19/045).
15. Shannon R. D. (1976), Revised effective ionic radii and systematic studies of interatomic distances in halides and chalcogenide, Acta Cryst., A32, 751 (doi:10.1107 / S 0567739476001551) .
16. Pandey P. K., Choudhary R. J., Phase D. M. (2013), Magnetic behavior of layered perovskite Sr_2CoO_4 thin film, Appl. Phys. Lett., 103, 132413 (doi: 10.1063/1.4823597).
17. Fullerton E. E., Jiang J.S., Bader S.D., (1999), Hard/soft magnetic heterostructures: model exchange-spring magnets, J. Mag. Mag. Mat., 200, 392 (doi.org/10.1016/S0304-8853 (99)00376-5).
18. Estrader M. *et al* (2013), Robust antiferromagnetic coupling in hard-soft bi-magnetic core/shell nanoparticles, Nat. Commun., 4, 2960 (doi:10.1038/ncomms3960).
19. Curecheriu L., Postolache P., Buscaglia V., Horchidan N., Alexe M., Mitoseriu L. (2013), $BaTiO_3$–ferrite composites with magnetocapacitance and hard/soft magnetic properties, Phase Trans., 86, 670 (doi:10.1080/01411594.2012.756879).
20. Kneller E. F., Hawig R. (1991), The Exchange-Spring Magnet: A New Material Principle for Permanent Magnets, IEEE Trans. Magne., 27, 3588, (doi:10.1109/20.102931).
21. Thang P. D. *et al* (2007), Stress-induced magnetic anisotropy of CoFe2O4 thin films using pulsed laser deposition, J. Magn. Magn. Mater. 310, 2621.

22. Stearns M. B., Cheng Y. (2004), Determination of para and ferromagnetic components of magnetization and magnetoresistance of granular Co/Ag films (invited), J. Appl. Phys., 75, 6894 (doi: 10.1063/1.356773).
23. Du L. *et al* (2010), Surfactant-Assisted Solvothermal Synthesis of $Ba(CoTi)_xFe_{12-2x}O_{19}$ Nanoparticles and Enhancement in Microwave Absorption Properties of Polyaniline, J. Phys. Chem. C, 114 (46), 19600(doi: 10.1021/jp1067268).
24. He T., Cava R. J. (2001), Disorder-induced ferromagnetism in CaRuO3, Phys. Rev. B, 63,172403 (doi:10.1103/ PhysRevB. 63. 172403).
25. Tripathi S. *et al* (2014), Ferromagnetic $CaRuO_3$, Scie.Rep., 4, 3877 (doi: 10.1038/ srep 03877).
26. Kumar S. *et al* (2014), Giant ferromagnetism and exchange bias in tensile strained and Cr modified CaRuO3 thin films, Appl. Phys. Lett., 104, 122411 (doi: 10.1063/1.4869977).
27. Hombo J. *et al* (1990), Electrical conductivities of $SrFeO_{3-\delta}$ and $BaFeO_{3-\delta}$ perovskites, J. Solid. State. Chem., 84**,** 138-143 (doi.org/10.1016/0022-4596(90)90192-Z).
28. Li T. *et al* (2013), Electronic structure and half-metallicity in preovskite $BaRu_{1-x}Fe_x O_3$: first-principles studies, Eur. Phys. J. B, 86, 414,(doi: 10.1140/epjb/e2013-40005-8).
29. MiddeyS. *et al* (2011), Glasslike ordering and spatial inhomogeneity of magnetic structure in $Ba_3FeRu_2O_9$: Role of Fe/Ru site disorder, Phys. Rev. B, 83, 144419 (doi: 10.1103/PhysRevB.83.144419).

~ End of Chapter 3 ~

Chapter 4

Interface Influenced Magnetism in $BaFeO_{3-\delta}$ /$BaTiO_3$ Multilayers

and

The Effects of Swift Ion Irradiation on structure and Magnetism of $BaFeO_{3-\delta}$ Thin Films.

In the previous chapters, we discussed about how physical properties of materials have been modified by chemical substitution and variation of strain. In addition to this, the physical properties of materials can be influenced by other techniques such as interface-induced strain in the form of heterostructures and by swift ion irradiation of thin films. In Chapter 3, influence of chemical substitution (Ti and Ru doping), strain and oxygen annealing on $BaFeO_{3-\delta}$ were explored. Each of these was found to influence the structural and magnetic properties of BFO. Present chapter is divided into two parts- **Part A** : *The influence of interfaces on properties of BFO when it is combined with other perovskite oxide in form of multilayers* and **Part B** : *Study of the effect of ion irradiation on BFO system.*

Part A

4.1 $BaFeO_{3-\delta}/BaTiO_3$ Multilayers

When a material is grown in form of thin film over a crystalline substrate, the material follows the structural geometry of the substrate. Generally, a material is grown over a single crystalline substrate with an appropriate lattice mismatch, this is termed as heteroepitaxy. As thin film nucleates, its crystal structure modifies according to the in-plane lattice parameters of the substrate. This lattice mismatching causes a strain in thin film. The extent of strain can be controlled by appropriate choice of substrate. Similarly, when two or more materials are combined in form of multilayers, their interfaces will be strained and fused. Now, a bulk system has all the degrees of freedom namely charge, spin, orbital and lattice, but in thin films, surfaces and interfaces put restrictions on these degrees of freedom [1]. Free surfaces terminate abruptly with dangling bonds which can be accommodated in the structure in different ways causing a change in the properties [2]. The interplay of various kinds of degrees of freedom at the interface causes breaking of symmetry, which in turn results in the change of physical and chemical properties [1]. The region at or around interfaces is never ideally sharp but has intermixing of chemical elements. The redistribution of charge or spins in the fused region causes change in the structural and magnetic properties of the system. Interfaces thus educe new properties in multilayers, not present in the parent materials.

The properties of perovskite oxides are dependent on the connectivity and distortion of BO_6 octahedra [3]. When grown over single crystals in perovskite heterostructure the octahedral connectivity must be maintained across the interface. This constraint enables the octahedral rotations or disortions to be transferred from substrate to film or from one layer to another (in case of hetrostructures). This feature makes perovskites particularly appealing for multilayer growth. Over past few years many unusual properties have been observed in perovskite multilayers and superlattices. For example, in $LaAlO_3/SrTiO_3$ multilayer, each of the constituting oxide is an insulator but interface gives rise to superconductivity [4,5]; antiferromagnetic $LaMnO_3$ and $SrMnO_3$ when combined as bilayer, show ferromagnetism with spin aligned in-plane at the interface [6,7]; multilayer of antiferromagnetic $CaMnO_3$ and paramagnetic $CaRuO_3$ have ferromagnetic interfaces [8]; superlattices of ferroelectric, dielectric and paraelectric materials like $BaTiO_3/SrTiO_3$, $KNbO_3/KTaO_3$ and $PbTiO_3/SrTiO_3$ show enhanced ferroelectricity due to interface effect [9,10].

Paucity of single phase room-temperature multiferroic materials has lead to the engineering of artificial multiferroic materials. An ideal way is to combine a ferroelectric and a magnetic material in form of multilayer or superlattice. BFO, being room temperature ferromagnet with correlated structure and magnetism, is a potential candidate for magnetoelectric materials. Recently, Fukatani *et al* [11] fabricated BFO and BTO superlattices which showed ferromagnetism and ferroelectricity simultaneously. They found enhancement in magnetization of superlattice due to interface effects [11,12]. The magnetic properties of BFO at room temperature are so complex that they leave a huge scope of scientific exploration.

It was discussed in Chapter 3 that structural changes in BFO due to epitaxial strain, doping and annealing lead to changes in its magnetic properties. The magnetic properties of BFO are correlated to the structural properties. $BaTiO_3$ (BTO) is another well known perovskite ferroelectric and has been combined with various oxides to yield new or improved properties [13]. Also, BTO has a structural flexibility to exist in several different structures at different temperatures in the same chemical composition without doping/annealing. It exists in cubic symmetry at high temperatures. When cooled, BTO shows a structural transition to tetragonal structure at 393 K, a second transition occurs at 278 K and a final transformation to rhombohedral structure appears at 183 K [13]. In a trilayer of $BaTiO_3/SrTiO_3/CaTiO_3$, interfaces lead to large polarization enhancement [14], $BaTiO_3/SrTiO_3$ superlattice has enhanced ferroelectricity [9] and $BaFeO_3/BaTiO_3$ superlattice shows coexisted ferromagnetic and ferroelectric state [11]. BFO also has flexibility of structure that it forms in single-phase structure from hexagonal in bulk to cubic in thin film. The combination of BFO and BTO was studied by us from a different perspective as follows: when BFO is combined with BTO in form of multilayers then the structure and interfaces with BTO should influence the properties of BFO. The chances of influencing the magnetic properties are high because both the oxides have Ba ions at A-site and *3d* transition metal ions at B-site. Now any change in structure of BFO via interfacial effect, will in turn affect its magnetic properties. Motive of our study was to synthesize multilayers and bilayers of BFO/BTO with different number of interfaces and to explore how the interfaces affect the magnetic properties of BFO.

4.2 Fabrication of BFO/BTO Bilayers

BFO and BTO pellets were used as targets for thin film synthesis. These targets were mounted on two different target holders. Multitarget rotation mechanism of PLD was employed for depositing the alternate layers of BFO and BTO. All the bilayers and mulilayers were grown on $SrTiO_3$ *(001)* single crystal substrates. The target to substrate distance was 4.2 *cm*. Substrate temperature was $700^{o}C$ and an oxygen partial pressure of 2.8 *mtorr* was maintained during deposition. The samples were then cooled at the deposition pressure. Laser energy was set at 260 *mJ* and the laser repetition rate was 5 *Hz.* Our investigations aimed at studying the effect of interfaces and see how the magnetic properties of BFO vary as the number of interfaces is increased. To do so we first fabricated bilayers, where there is single and sharp interface between BFO/BTO and then gradually increased the number of interfaces keeping the total number of shots constant. Table 4a-I gives the synthesis details of layered structures. Many samples were deposited to optimize the above deposition parameters before obtaining the results presented here.

Table 4a-I: Fabrication-details of bilayers.

Sample Code	**No. of shots**		**No. of repetition**	**% of BFO**	**% of BTO**
	BFO	**BTO**			
BFO/BTO^T	6300	6300	1	50	50
BTO/BFO^T	6300	6300	1	50	50
$(BFO/BTO)_{36}$	175	175	36	50	50
$(BFO/BTO)_{18}$	500	200	18	71.4	28.6

4.3 Results and Discussion

Two bilayers were prepared with equal proportion of BFO and BTO (1:1). In one bilayer, BFO was the top layer (BTO/BFO^T) and in another, BTO was the top layer (BFO/BTO^T). Each layer had a thickness of 450 *nm*. The thickness was chosen such that the magnetometer can detect the signal from the weak magnetization of these layers and we can subtract the diamagnetic contribution of STO substrates, without noise in the net magnetization.

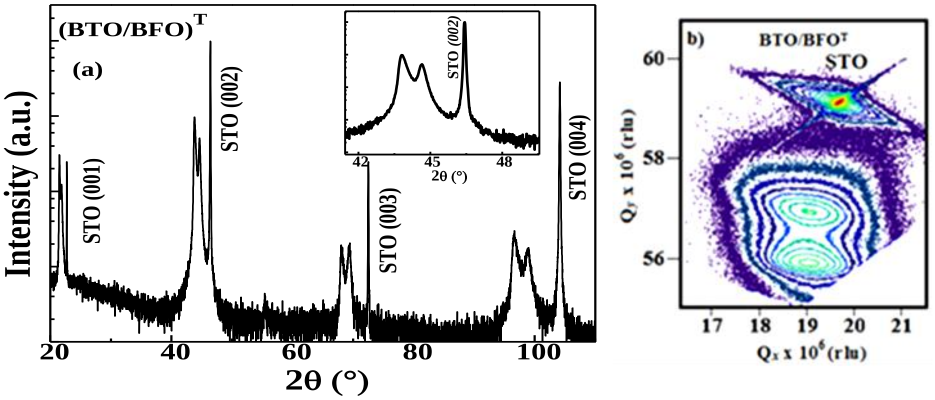

Figure 4a.1: a) XRD pattern b) RSM of bilayer with BFO on top.

Figure 4a.1(a) shows the XRD pattern of BTO/BFO^T. Two XRD peaks from material clearly indicate the formation of two layers with discernible interfaces. These layers have partially relaxed state of strain as apparent from RSM shown in Figure 4a.1(b). RSM images again confirm the formation of bilayers with two in-plane peaks along with the peak of the substrate.

Now we compare the magnetization of BFO film deposited on STO and bilayer BTO/BFO^T deposited on STO. In both the samples (film and bilayer), BFO acquires the position as top layer. The layer of BTO is diamagnetic and contributes negligibly in the magnetization. So whatever magnetic characteristics of bilayer are observed, originate from BFO only. Magnetization measurements showed that BTO/BFO^T has a weak ferromagnetic state at room temperature (Figure 4a.2(b)). Magnetization in BTO/BFO^T has decreased as compared to BFO-S (Figure 3.25) as illustrated by the ZFC and FC magnetization curves in Figure 4a.2(a). An onset of short-range ferromagnetic phase can be observed for bilayer at ~ 260 K. We found that the magnetization of bilayer is reduced in comparison, because the thickness of BFO layer is different and deposition parameters are different. In addition, the BFO-S film has substrate as template on which the film grew whereas BTO/BFO^T has BTO as a bottom layer.

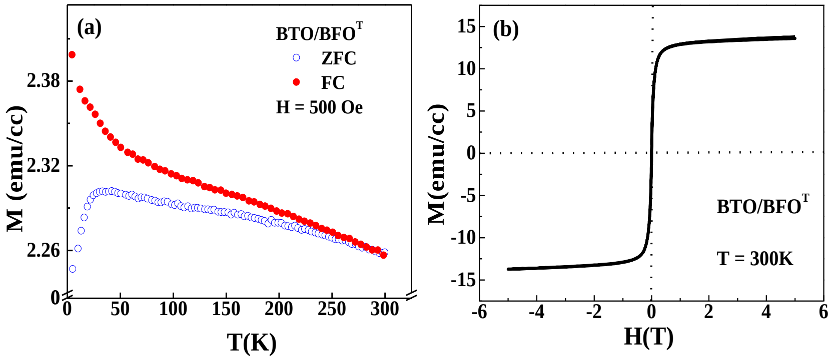

Figure 4a.2: a) ZFC and FC magnetization curves b) Magnetization versus magnetic field isotherm at 300K of BTO/BFO^T.

Generally, different deposition parameters and other such differences give rise to such changes in magnetization of the material synthesized by PLD technique. In the following discussion, we will compare the magnetization of bilayers prepared under the same deposition conditions.

Another bilayer was deposited with identical parameter as that of BTO/BFO^T, but in this case, BFO was first deposited on STO then covered with BTO layer (BFO/BTO^T). Therefore in this bilayer, BFO is sandwiched. In BTO/BFO^T, BFO is top-layer and had one free surface, but in BFO/BTO^T, BFO is placed between STO (bottom) and BTO (top). Similar to BTO/BFO^T, the formation of bilayer was confirmed from the XRD and RSM measurements of BFO/BTO^T bilayer (Figure 4a.3(a &b)).

If the XRDs and RSMs of both the bilayers are compared, they clearly show minor structural differences owing to different strain distributions. The different distribution of strain could be acquired by the samples because of different bottom-layer/substrate.

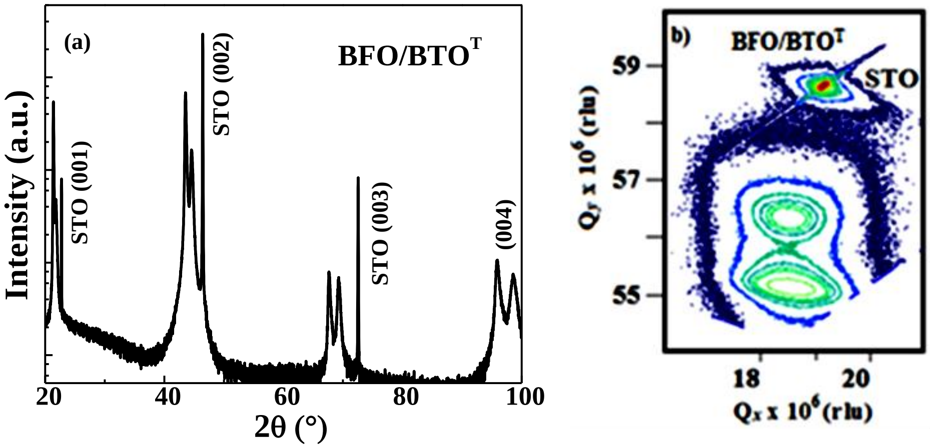

Figure 4a.3: a) XRD pattern b) RSM of BFO/BTO^T bilayer.

Now we compare the magnetization of both the above mentioned bilayers. When BFO was sandwiched between STO and BTO, magnetization showed a very different variation with temperature (Figure 4a.4(a)) as compared to when it has a free surface on top (Figure 4a.2(a)). Whereas, separation between ZFC and FC magnetization curves is diminished for sandwiched BFO indicating diminished short-range ferromagnetic interactions. Also, a frustrated magnetic state arises in the low-temperature region. The magnetization isotherm at 300 *K* of BFO/BTO^T shows a very weak ferromagnetic state as compared to BTO/BFO^T. At 20 K, a dominating antiferromagnetic behavior is reflected by the M(H) loop with competing ferromagnetic interactions (Figure 4a.4(c)). Thus, the bilayers of BTO and BFO show dramatically different magnetic behavior in spite of the same proportions of BFO and BTO compounds. This difference of magnetic behavior can be plausibly explained as follows.

In BTO/BFO^T bilayer, BFO encounters strain at one surface in contact with BTO, while the free surface of the bilayer is formed by BFO layer. Thickness of BFO layer in BTO/BFO^T is ~ 450 *nm* and the chemically diffused region would extend a few nanometers beyond. In

BFO/BTO^T, BFO is sandwiched, and there are two interfaces of BFO: one with STO and another with BTO. Unlike BTO/BFO^T, there is no free surface in BFO/BTO^T, thus, latter has larger content of diffusion. In addition, the sandwiched layer would experience a larger distribution of strain in order to form the sandwiched structure between two different materials. In addition, there are lesser degrees of freedom to the sandwiched structure. Therefore, the sandwiched BFO behaves more like antiferromagnetic at low temperature and like a very weak ferromagnet at room temperature.

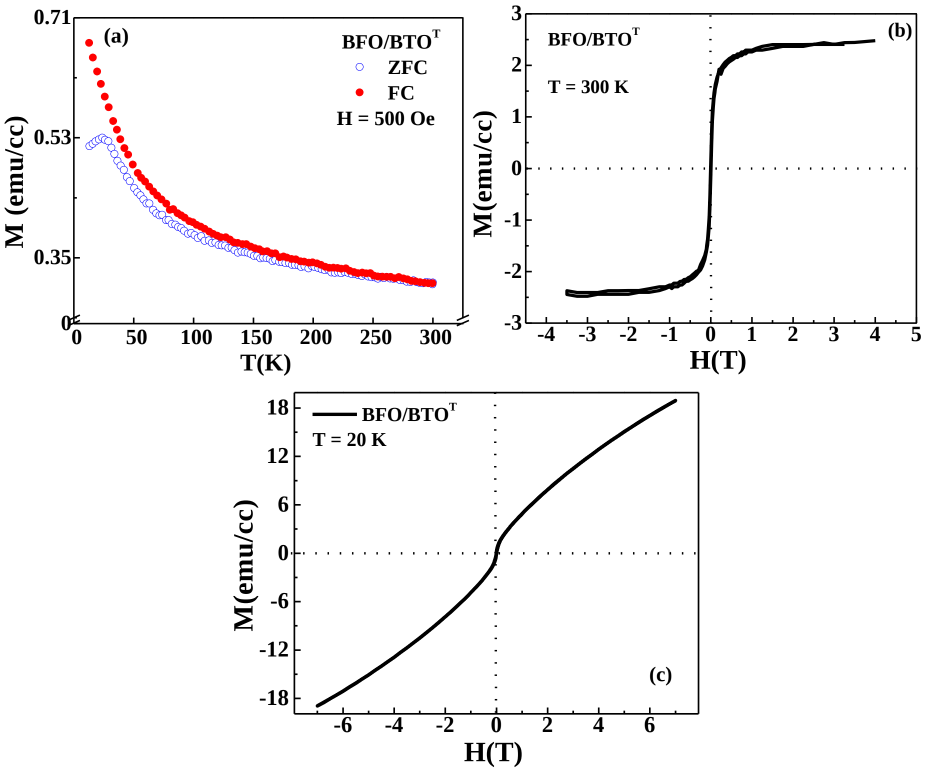

Figure 4a.4: a) ZFC and FC magnetization curves and magnetization versus magnetic field isotherm at b) 300 K and c) 20K of BFO/BTO^T.

Now keeping the ratio of the content of BFO and BTO constant (same as in bilayers), we deposited a multilayer with 36 alternate layers of BFO and BTO, each having a thickness of 12 nm $(BFO/BTO)_{36}$. RSM gives very clear evidence of the formation of multilayers with sharp interfaces where we have observed several peaks for the materials deposited (Figure 4a.5(b)). The XRD pattern shows two broad peaks (Figure 4a.5(a)) with no discernible satellite peaks. Figures 4a.6 shows the magnetization of multilayer. With increase in number of interfaces, the magnetization enhances compared to that of BFO/BTO^T, but the magnetization is slightly less than that of BTO/BFO^T.

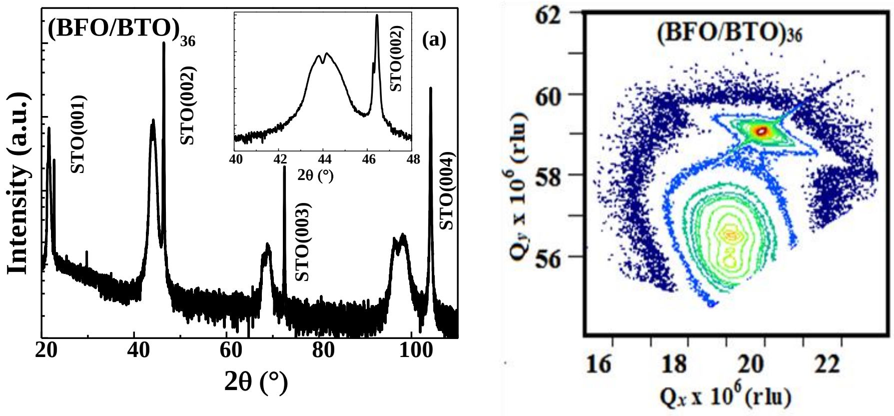

Figure 4a.5: a) XRD pattern and b) RSM of superlattice (BFO/BTO)$_{36}$.

The transition to frustrated magnetic state at low temperature diminished in multilayer. Thus, rather a long-range antiferromagnetic phase is found to arise dominatingly in case of (BTO/BFO)$_{36}$ same as in BFO/BTO^T bilayer.

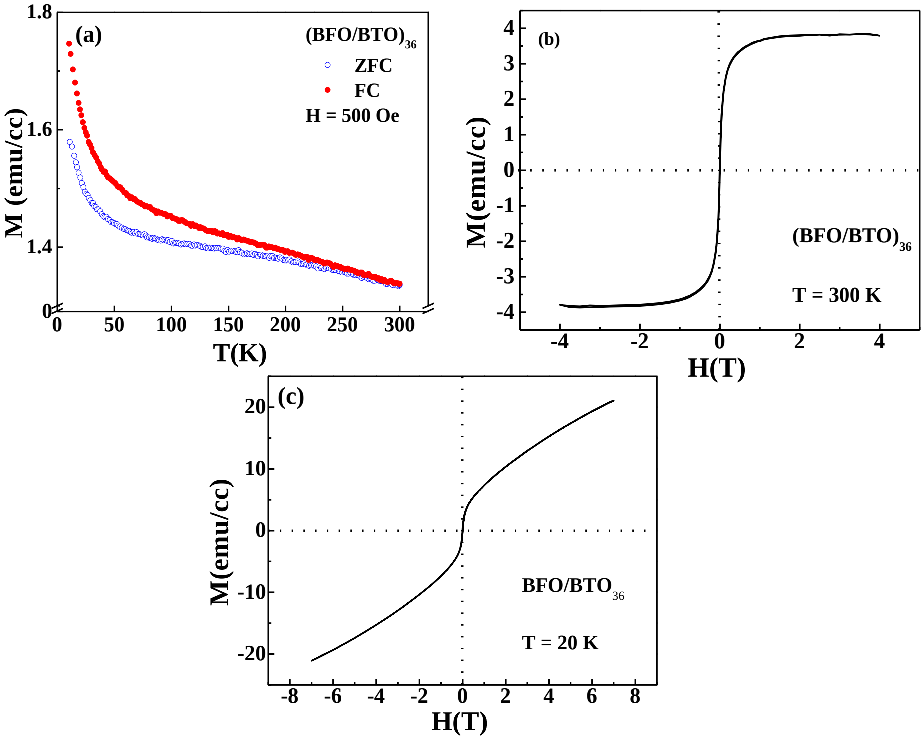

Figure 4a.6: a) ZFC and FC magnetization curves and magnetization versus magnetic field isotherm b) 300 K and c) 20 K of (BFO/BTO)$_{36}$.

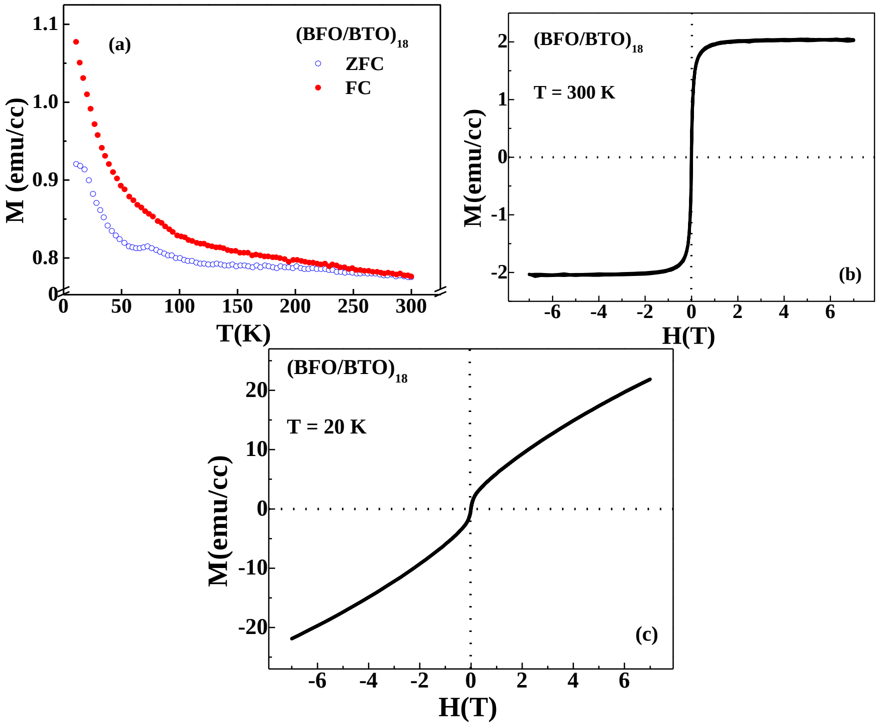

Figure 4a.7: a) ZFC and FC magnetization curves and magnetization versus magnetic field isotherm at b) 300 K and c) 20 K of (BFO/BTO)$_{18}$.

However, the magnetization measurements at 20 K also clearly illustrate the antiferromagnetic order with competing magnetic interactions, which also appears in large ZFC-FC separation at low-temperatures. This indicates highly competing short-range ferromagnetic phase embedded within antiferromagnetic background at low temperatures.

In the next stage of this study, the multilayers were made with a larger proportion of BFO (70%) and lesser BTO (30%). 18 layers of BFO and BTO, with each layer having a thickness of about 35 nm, was synthesized (BTO/BFO)$_{18}$. Figure 4a.7 shows the magnetization plots of this multilayer. A clear transition in ZFC at ~ 75 *K* is observed, which was absent in the bilayers and other multilayer with equal proportions (1:1) of BFO and BTO. This transition did not appear clearly anywhere in bilayers. It shows that, with an increased content of BFO in (BFO/BTO)$_{18}$, the magnetic behavior changes. This transition will be discussed later.

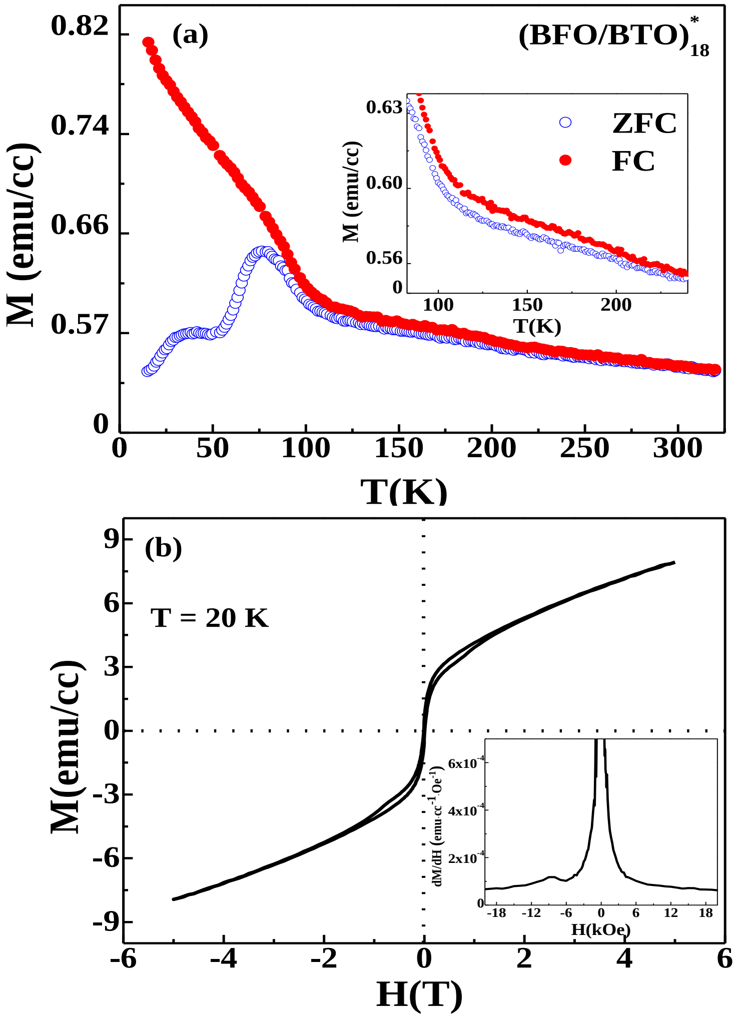

Figure 4a.8: a) ZFC and FC magnetization curves at H = 500 Oe and magnetization versus magnetic field isotherm of (BFO/BTO)$^{*}_{18}$ at 20 K.

To further understand the magnetic behavior of multilayers with 70% BFO content, we made another multilayer [(BFO/BTO)$^{*}_{18}$], having exactly same composition as (BFO/BTO)$_{18}$, but fabricated at a higher oxygen partial pressure (5 *mTorr*) during deposition. It was *insitu* annealed at the deposition temperature (700^{o}*C*) for 5 *mins* at 100 *mTorr* oxygen pressure. It was then cooled to ambient temperature at the same pressure. In the following paragraphs, we compare the magnetic behavior of the two multilayers with 70% BFO and 30% BTO.

In $(BFO/BTO)^*_{18}$, all the features/transitions became sharper and the separation between ZFC and FC curves did not enhance as temperature decreased (Figure 4a.8). This multilayer undergoes sharper transition at 75 K and a cluster-glass like state appears around 35 K as seen in Figure 4a.8. The transitions of $(BFO/BTO)^*_{18}$ also appeared in $(BFO/BTO)_{18}$ but were subdued in terms of sharpness. To further investigate this transition, magnetization isotherms were measured above and below this hump like feature around 75 K (125 K and 43 K). As shown in Figure 4a.9, the magnetization isotherm at 43 K shows enhanced antiferromagnetic interactions which remain absent in the isotherm recorded at 125 K. It clearly indicates that the magnetic transition at 75 K is the onset of antiferromagnetic phase. This transition did not appear clearly in any film or bilayers.

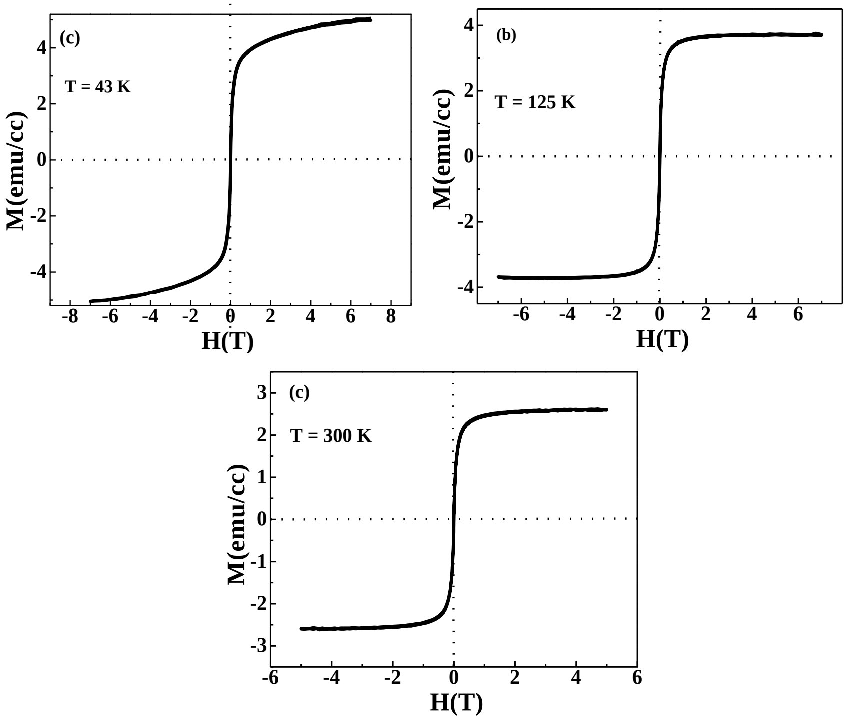

Figure 4a.9: Magnetization versus magnetic field isotherms of $(BFO/BTO)^*_{18}$ at three different temperatures, (a) 43 K, (b) 125 K and (c) 300 K.

The magnetization isotherm recorded at 20 K (Figure 4a.8) shows that $(BFO/BTO)^*_{18}$ has qualitatively hard (less soft) ferromagnetic phase embedded in antiferromagnetic background. It should be noted that $(BFO/BTO)^{*}_{18}$ was deposited at high oxygen pressure and similarly the oxygen annealed film of BFO (Chapter 3) tend to show development of hard magnetic phase. The inset of Figure 4a.8b shows *dM/dH* versus H at 20 K indicating two coercive magnetic fields one soft and another hard (less soft) confirming the presence of hard ferromagnetic phase. However, the total magnetic moment of $(BFO/BTO)_{18}$ remains high compared to $(BFO/BTO)^{*}_{18}$ due to the presence of the soft ferromagnetic phase.

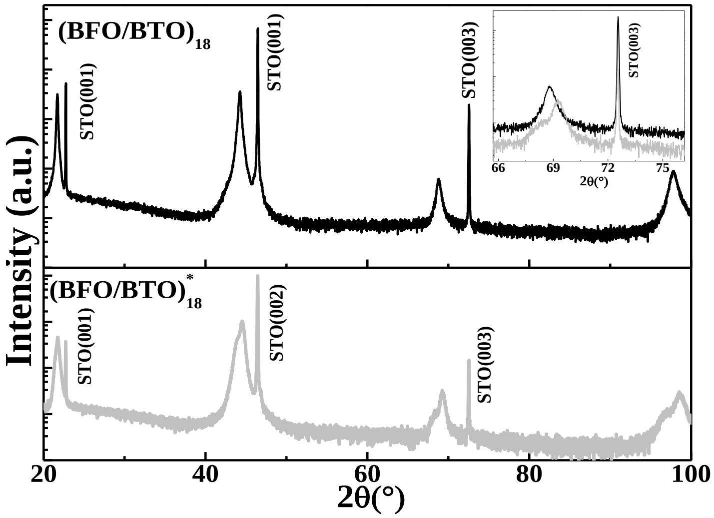

Figure 4a.10: XRD patterns of $(BFO/BTO)_{18}$ and $(BFO/BTO)^{*}_{18}$ compared.

Apart from all the above mentioned features, we observed a very weakly appearing transition marked by a broad hump centered about 185 K in FC curve of $(BFO/BTO)^{*}_{18}$ multilayer. Let us note that BTO undergoes structural transition from orthorhombic to rhombohedral phase at 183 K. If this would be related to the onset of competing magnetic interactions (like in thin films), generally such separation should appear well above 200 K. Therefore, it is contemplated that this hump plausibly corresponds to the structural transition of BTO. This transition does not appear so clearly in bilayers or $(BFO/BTO)_{18}$. This magnetic transition probably indicates that a correlation has been established between structural transition of BTO and magnetism of BFO in case of $(BFO/BTO)^{*}_{18}$ multilayer deposited at slightly higher oxygen pressure.

On comparing the XRD patterns of these two multilayers, it was found that the crystallinity of $(BFO/BTO)^{*}_{18}$ is better than that of $(BFO/BTO)_{18}$ multilayer. Thus, indicating that the high oxygen pressure has improved the crystallinity of this multilayer and therefore, we observe sharp magnetic transitions compared to the other $(BFO/BTO)_{18}$ multilayer.

Part B

Swift O^{7+} and Ag^{15+} Ion Irradiation of $BaFeO_{3-\delta}$ Thin Films

Since the inception of nuclear reactor, high-speed ions have been used in a variety of ways in science and technology. Ion irradiation has been used in creating nanometer size defects in a controlled way in thin films and bulk material. These defects can result in change of their physical properties which can be correlated to the structural, morphological and chemical stoichiometric changes. In this segment of thesis we discuss the effects of ion irradiation on the structural and magnetic properties of $BaFeO_{3-\delta}$ thin films

4.4 Experimental details

Seven identical films of $BaFeO_{3-\delta}$ (thickness ~ 250 *nm*) were fabricated on MgO *(001)* for ion irradiation study. The laser energy was set at 260 *mJ* and repetition rate was 5 *Hz*. The target to substrate distance was kept 4.2 *cm* and substrate temperature was maintained at 700 ^{o}C. Thin films were deposited in an oxygen partial pressure of 2.8 *mTorr* and were cooled to ambient temperature in the same pressure. The ion irradiation was carried out using 15UD Pelletron at the Inter University Accelerator Center (IUAC), New Delhi. One of the films was left untreated which is termed as pristine film. Three films were irradiated by Ag^{15+} ion beam of energy 150 *MeV* and the other three were irradiated by O^{7+} ion beam of energy 100 *MeV*. Fluence of ion beams was varied from 1x10^{11} to 1x10^{12} *ions/cm*^{2}.

4.5 Results and Discussion

All the seven films fabricated on MgO *(001)* formed highly oriented along the substrate's crystallographic direction and no peak corresponding to any impurity was found. Ion irradiation influences the structure of BFO as shown in Figure 4b.1, which shows a typical shift in *(002)* Bragg peak of different films. As the ion fluence increases, Ag^{15+} ion irradiated films exhibit a systematic shift of XRD peaks to lower 2θ values with decreasing peak intensity as compared to that of the pristine film. This corresponds to a gradual increase in the lattice parameter with increasing ion fluence. On the other hand the series of films irradiated by O^{7+} ions show a change in structure, but this change is not so systematic. As seen in Figure 4b.1, the 2θ value first decreases and then becomes almost equal to that of the pristine film.

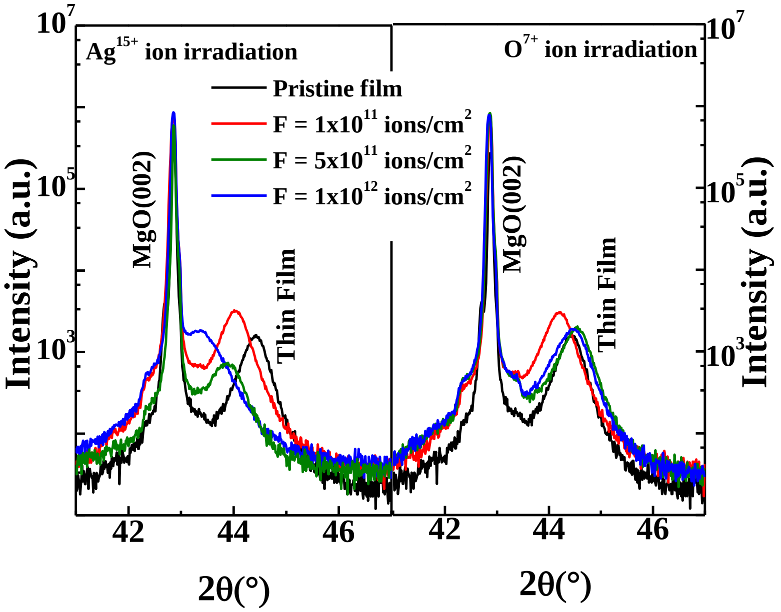

Figure 4b.1: XRD (002) peak shift of pristine and irradiated films compared.

For further investigations, we recorded RSMs of all the films as shown in Figure 4b.2. The peak *(311)* shifts towards the substrate peak for Ag^{15+} ion irradiated films, with increasing fluence. A minor, but non-systematic shift in *(311)* peak was also observed for O^{7+} irradiated films.

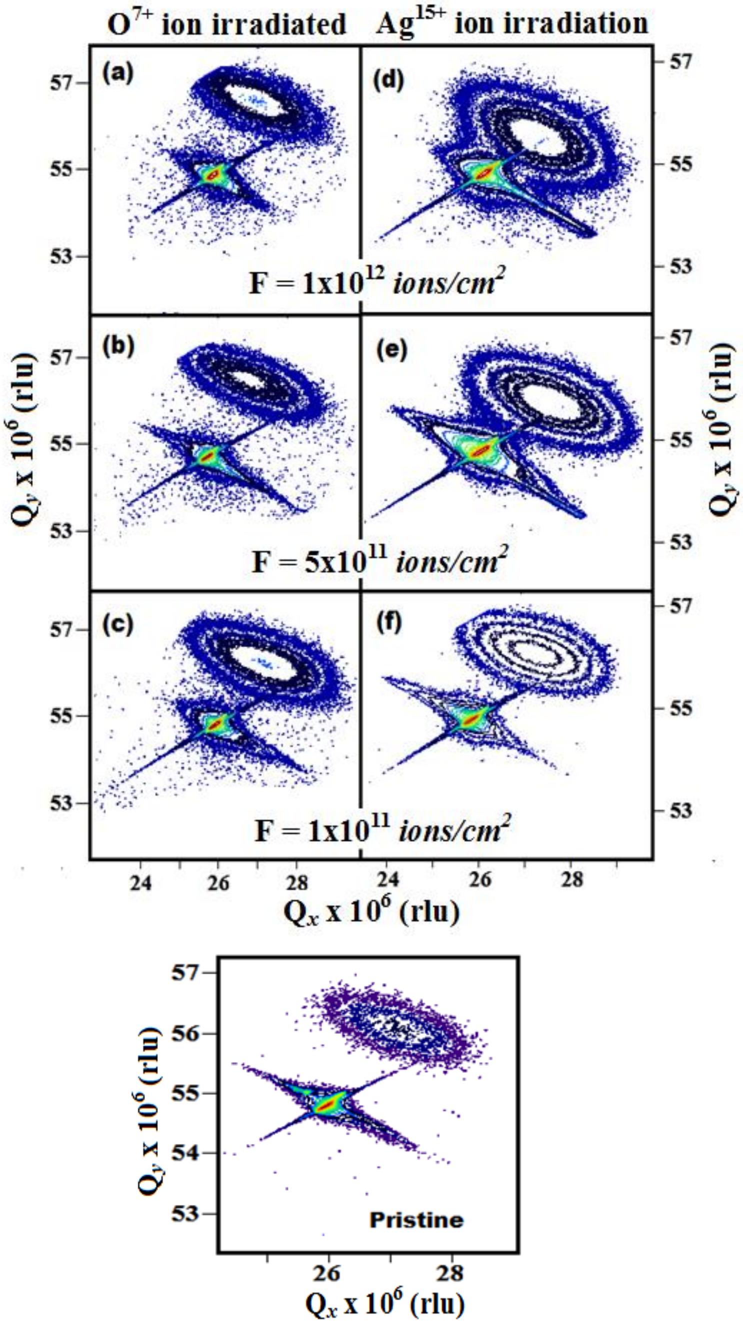

Figure 4b.2: RSMs of pristine and irradiated films around (311) peak.

As mentioned earlier, irradiation causes point defects, clusters or columnar defects on the surface of thin films. Surface morphology of these irradiated films was observed using an atomic force microscope. Thin films irradiated by *Ag*$^{15+}$ ions showed columnar defects (Figure 4b.3*)* for the fluence of 1x10^{11}*ions/cm*^{2}. With further increase in fluence, the surface of films appeared very rough and battered. When heavy ions with such high energy fall on thin films they form cylindrical paths as they move through the volume of material. These paths appear in form of columnar defects. As the fluence increases the density of these defects also increases which may sometimes completely destroy the structure of the film. In case of lighter *O*$^{7+}$ ion no such columnar defects were observed. *O*$^{7+}$ ion irradiation probably results in nano-size point-like defects which could not be resolved by the AFM system we used. Such irradiation-defects tend to relax the tensile strain in the film [15-17], however the shift of XRD peaks show that the lattice parameters are increasing, which corresponds to an increase in in-plane tensile strain rather than relaxing it. Table 4b-I lists the change in lattice constant. It is clear from the table that the lattice parameters vary systematically with increasing fluence of Ag^{15+} ions, however we did not see consistency in changing lattice parameters with increasing fluence of O^{7+} ions, rather the maximum O^{7+} ion irradiated film shows the lattice constant equivalent to that of pristine film.

Table 4b-I: List of lattice parameters with increasing fluence.

Fluence (ions/cm^{2})	**Lattice parameter d (Å)**	
	Ag-ion	**O-ion**
Pristine	4.07	
1 x 10^{11}	4.107	4.092
5 x 10^{11}	4.119	4.063
1 x 10^{12}	4.167	4.068

In Chapter 3, we have seen that oxygen annealing reduces oxygen vacancies in BFO which causes a shift in XRD peaks to higher *2θ* value (lower lattice parameter) due to conversion of larger Fe^{3+} ions to smaller sized Fe^{4+} ions in the system. Here, the films show increase in the lattice parameter, therefore it implies that when films are bombarded with heavy Ag^{15+} ion, they knock out certain amount of oxygen ions which are lighter than Ag ions. It is known that, during swift *heavy* ion irradiation, the lighter ions get knocked out [15,18]. Thus, it results into a conversion of Fe^{4+} to Fe^{3+} ions in order to neutralize the charge. This causes a systematic variation of lattice constant of irradiated films with increasing ion fluence (Table 4b-I). Change in crystal structure on irradiation has been observed earlier in other systems also [19-23]. O^{7+} ions being light ion, cannot knock out oxygen from the lattice, though they do cause local point defects.

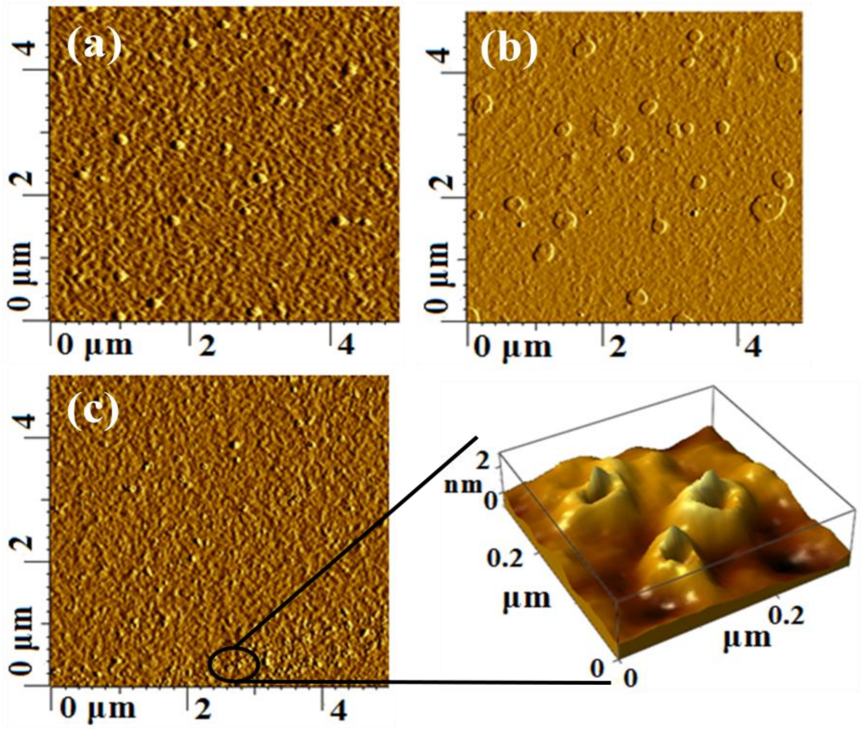

Figure 4b.3: AFM images of a) pristine b) O^{7+}-ion irradiated ($F = 1 \times 10^{11}$ ions/cm^2) c) Ag^{15+}-ion irradiated ($F = 1 \times 10^{11}$ ions/cm^2) BFO thin films and d) columnar defects on the surface film in shown in 'c'.

Surface roughness and grain size both increased gradually with the increasing fluence in case of Ag^{15+} ions irradiation but again no trend was observed in case of O^{7+} ion irradiation. This confirms that Ag^{15+} ion irradiation damages the structure of BFO thin films.

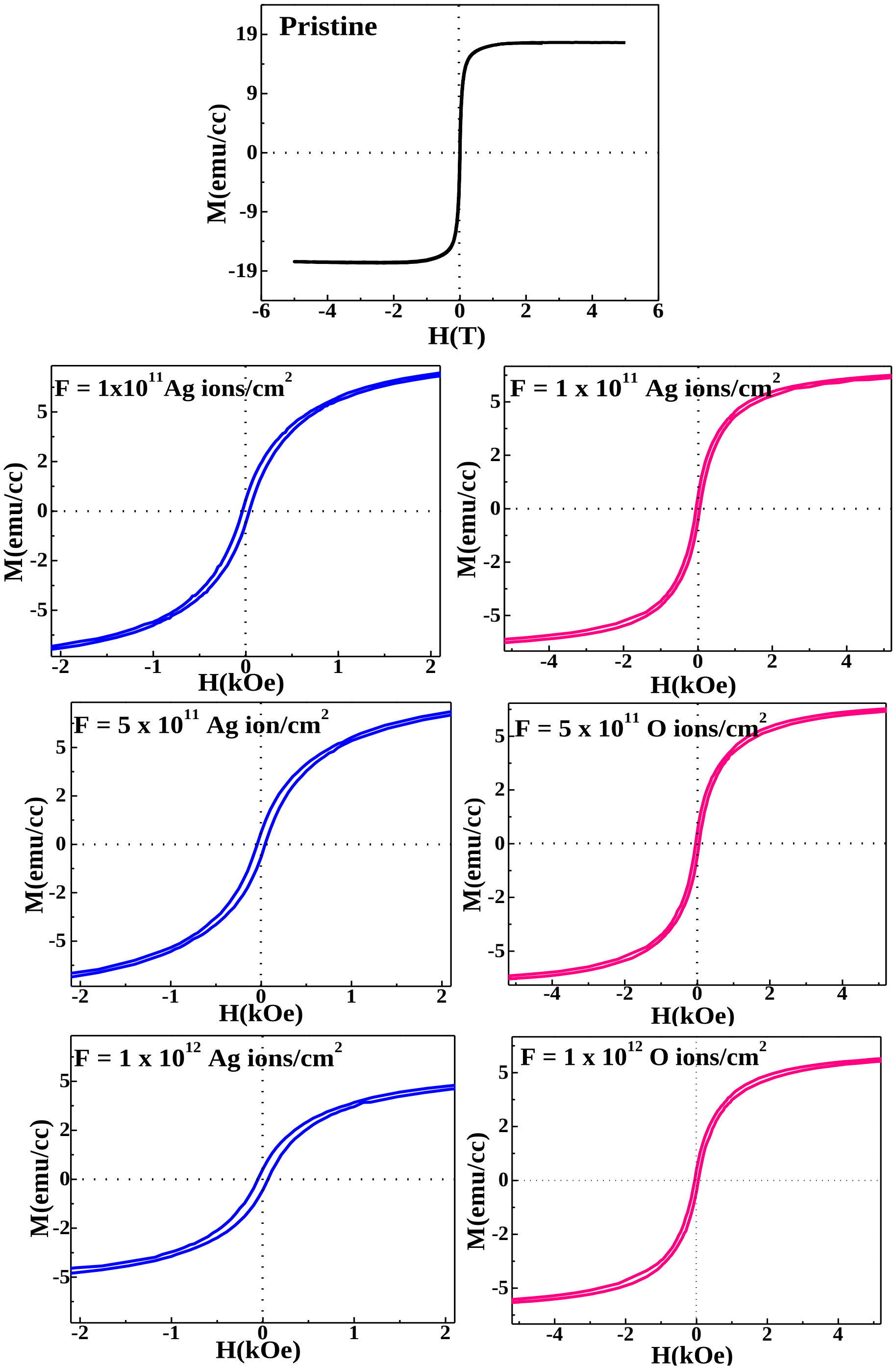

Figure 4b.4: Magnetization versus magnetic field isotherms of pristine and irradiated BFO thin films at 300 K.

To study the magnetic properties in context of irradiation effects,

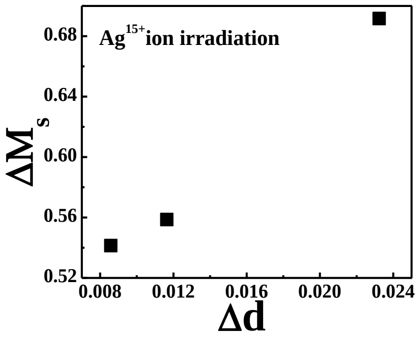

Figure 4b.5: Variation of change in saturation magnetization with change in lattice parameter of irradiated BFO thin films.

the magnetization isotherms of these films were measured at room temperature. All the films are weakly ferromagnetic at 300 *K* as is visible in Figure 4b.4. For 1×10^{11} *ions/cm*^{2} ion fluence, initially the magnetization decreases drastically. Further increase in the ion fluence does not affect magnetization as much in the case of O^{7+} irradiated films, but changes the magnetization gradually in case of Ag^{15+} ion irradiated films. However, this change in magnetization is very small. The maximum Ag^{15+} ion irradiated film shows the least saturation magnetization due to highest damage. In addition, Ag^{15+} ion irradiated films show a gradual but minor increase in the coercivity with increasing ion fluence (Table 4b-II). The change in magnetization follows almost a systematic trend with the change in lattice parameter (Figure *4b.5*). Ag^{15+} ions create columnar defects in BFO thin films, these defects result in pinning of domain walls which along with increased surface roughness causes enhancement in coercivity of irradiated films.

Table 4b-II: Variation Coercive fields of irradiated films compared to the pristine film.

Fluence (ions/cm^2)	**Coercivity H_c (Oe)**	
	Ag-ion	**O-ion**
Pristine	33	
1 x 10^{11}	37	47
5 x 10^{11}	43	47
1 x 10^{12}	56	52

4.6 Conclusions

- Both, the bilayers and the multilayers have interface formation as detected by RSM and XRD measurements.
- On comparing the magnetization of layered structures with 1:1 proportions of BFO and BTO (three samples: two bilayers and one multilayer), it can be seen that the sandwiched BFO has weakest ferromagnetic interactions whereas the bilayer with BFO on top shows the highest magnetization and growth of ferromagnetic phase, while the sandwiched BFO shows the least. It shows sandwiched interfaces restricts the degrees of freedom of BFO to grow ferromagnetic phase.
- The multilayer deposited under higher oxygen pressure shows sharp magnetic transitions and growth of hard magnetic phase.
- Ag^{15+} ion irradiation shows correlated and systematic changes in the structure and magnetization, which confirms that the oxygen ions get knocked out due to increased fluence of Ag ions.
- Ag ion irradiation creates columnar defects in BFO film.
- Oxygen ion irradiation damages the structure, but O^{7+} being lighter than oxygen ions, cannot knock out oxygen ions like Ag irradiation. No systematics is observed for this series of films.

References

1. Zubko P. *et al* (2011), Interface physics in complex oxide heterostructures, Annu. Rev. Condens. Mat. Phys., 2, 141 (doi: 10.1146/annurev-conmatphys-062910-140445).
2. Rondinelli J. M. and Spaldin N. A. (2011), Structure and properties of functional oxide thin films: insights from electronic-structure calculations, Adv. Mater., 23, 3363 (doi: 10.1002/adma.201101152).
3. Rondinelli J. M., May S. J., Freeland J. W. (2012), Control of octahedral connectivity in perovskite oxide heterostructures: An

emerging route to multifunctional materials discovery, MRS Bulletin, 37, 261, (doi: 10.1557/mrs.2012.49).

4. Janicka K., Velev J. P., Tsymbal E. Y. (2008), Magnetism of $LaAlO_3/SrTiO_3$ superlattices, J. Appl. Phys., 103, 07B508 (doi : 10.1063/1.2829244).
5. Ohtomo A., Hwang H. Y. (2004), A high-mobility electron gas at the $LaAlO_3/SrTiO_3$ heterointerface, Nature, 427, 423 (doi:10.1038/nature02308).
6. Ogawa N. *et al* (2008), Nonlinear optical detection of a ferromagnetic state at the single interface of an antiferromagnetic $LaMnO_3/SrMnO_3$ double layer, Phy. Rev. B, 78, 212409 (doi: 10.1103/PhysRevB.78.212409).
7. Bhattacharya A. *et al* (2008), Metal-Insulator Transition and Its Relation to Magnetic Structure in $(LaMnO_3)_{2n}/(SrMnO_3)_n$ Superlattices, Phy. Rev. Lett., 100, 257203 (doi: 10.1103/PhysRevLett.100.257203).
8. He C. *et al* (2012), Interfacial Ferromagnetism and Exchange Bias in $CaRuO_3/CaMnO_3$ Superlattices, Phys. Rev. Lett., 109, 197202 (10.1103/PhysRevLett.109.197202).
9. Diéguez O. *et al* (2005), First-principles study of epitaxial strain in perovskites, Phys. Rev. B, 72,144101(DOI: 10.1103/PhysRevB.72.144101).
10. Dawber M. *et al* (2007), Tailoring the Properties of Artificially Layered Ferroelectric Superlattices Matthew Adv. Mater., 19, 4153 (doi: 10.1002/adma.200700965).
11. Fukatani R. *el al* (2012), Ferroelectricity and Ferromagnetism of $BaTiO_3/BaFeO_3$ Superlattice Thin Films, Japan. J. Appl. Phys., 51, 09LB01 (doi.org/10.1143/JJAP.51.09LB01).
12. Yokota H. *et al* (2010), Fabrication and characterizations of Multiferroic super-lattice thin films $BaTiO_3/BaFeO_3$, Applications

of Ferroelectrics (ISAF), IEEE International Symposium (10.1109/ISAF.2010.5712255).

13. M. K. Lee, T. K. Nath, C. B. Eom, M. C. Smoak, F. Tsui, (2010), Strain modification of epitaxial perovskite oxide thin films using structural transitions of ferroelectric $BaTiO_3$ substrate Appl. Phys. Lett. 77, 3547 (doi.org/10.1063/1.1328762)
14. Lee H. N. *et al* (2005), Strong polarization enhancement in asymmetric three-component ferroelectric superlattices, Nature, 433, 395 (doi: 10.1038/nature03261).
15. Avasthi D. K. , Mehta G. K. (2011), Swift Heavy Ions for Materials Engineering and Nanostructuring, Springer, (978-9400712287).
16. Kumar et al (2006), Swift heavy ion irradiation-induced modifications in structural, magnetic and electrical transport properties of epitaxial magnetite thin films, J. Appl. Phys., 100, 033703 (doi: 10.1063/1.2222066).
17. Dhamodaran S. (2007), High-resolution XRD analysis of swift heavy ion irradiated InGaAs/GaAs heterostructures, Nucl. Instru. Meth. Phys. Res. B, 256, 260 (doi:10.1016/j.nimb.2006.12.011).
18. Bandyopadhyay S.K. *et al* (1998), Irradiation-induced oxygen knock-out and its role in bismuth cuprate superconductors, Phys. Rev. B, 58, 15135 (doi: 10.1103 / PhysRevB.58.15135).
19. D.C. Agarwal *et al* (2006), SHI induced modification of ZnO thin film: Optical and structural studies, Nucl. Instru. Meth. Phys. Res. B, 244, 136–140 (doi:10.1016/j.nimb.2005.11.077).
20. Mallick P. *et al* (2008), Swift heavy ion irradiation induced texturing in NiO thin films, Nucl. Instru. Meth. Phys. Res. B, 266, 3332 (doi:10.1016/j.nimb.2008.04.013).

21. Mishra N.C. (2011), Swift heavy ion irradiation-induced phase transformation in oxide materials, Rad. Effec. Defec. Solid., 166, 657.

22. Krasheninnikov A. V., Nordlund K. (2010), Ion and electron irradiation-induced effects in nanostructured materials, J. Appl. Phys., 107, 071301 (doi:10.1063/1.3318261).

23. Benyagoub A. (2005), Mechanism of the monoclinic-to-tetragonal phase transition induced in zirconia and hafnia by swift heavy ions, Phys. Rev. B, 72, 094114 (doi: 10.1103/PhysRevB.72.094114).

~End of Chapter 4~

Chapter 5

Structural and Magnetic Correlations in Tensile and Compressive Strained Epitaxial Thin Films of $Pr_{0.5-x}Ce_xCa_{0.5}MnO_3$ Manganites

5.1 Introduction

The phenomenon of magnetoresistance, *i.e.*, decreases/increase of resistance on the application of magnetic field, possesses technological applications as read-heads in magnetic data-storage devices. Conventionally, the magnitude of magnetoresistance (MR), calculated as MR = $[(\rho_H - \rho_0)/ \rho_0]\times 100$ (where $\rho_{H/0}$ is resistivity 'with magnetic field'/ 'with no magnetic field'), in normal metal is only a few percent. Intense research on various aspect of MR was triggered by the Nobel Prize winning discovery by Albert Fert and Peter Grünberg (year 2007), who demonstrated extraordinarily large MR of about 30% in engineered superlattices of magnetic and metallic systems. The term 'Giant Magnetoresistance (GMR)' was coined to signify the large magnitude of this effect. The GMR was obtained at room temperature, which promised to revolutionize the sensitivity and speed of magnetic read-heads [1, 2]. Given such a huge potential of the phenomenon of MR, the materials scientists around the world started searching for alternate and even more efficient MR devices. It was in 1993 when Von Helmolt *et al* [3] obtained an MR of about 50-60% in pure perovskite manganite $La_{0.7}Ba_{0.3}MnO_3$. The magnitude of MR was significantly larger than GMR and, hence, a new term 'colossal magnetoresistance (CMR)' was coined to indentify the MR in divalent cation doped or the so called mixed-valent ABO_3 perovskite manganites. This opened up a whole new field of research and a large section of researchers started focussing on understanding and tailoring magnetoresistive properties in manganites. Subsequently, a CMR of 100 % was demonstrated to occur in several divalent cation (Ca^{2+}, Sr^{2+} and Ba^{2+}) doped rare-earth based $RMnO_3$ systems [4,5]. A great deal of researches resulted in a very large number of research papers focussed on the CMR aspects of manganites. Though a CMR of as large as 100% was obtained in manganites, it occurred at low temperatures which could not beat the technology utility of GMR superlattices with large MR at room temperature. In addition, the stability and longevity related issues inherent to manganite oxides hindered the potential of utility aspects of the CMR phenomenon. However, simultaneous to this, several other phenomena rich in fundamental physics caught the attention. Correlation arising from the spin, charge, orbital and lattice degrees of freedom comprised the rich magnetic, electronic and structural phase diagrams of various series of manganites [6]. Eventually, the potential of charge- and orbital-ordering and related phenomena drew all the research attention. A magnetic-field induced melting of charge-ordering resulting in 100% MR, ultra-sharp metamagnetic and electronic phase transitions, vulnerability of the charge-ordering to the structural modification, defects and chemical modifications, and influence of tolerance factor and size-disorder to the charge-ordering, *etc*., are some of the mainstay research areas of charge-ordered manganites.

The ABO_3-type perovskite manganites display complex properties arising due to the lattice, magnetic, and charge degrees of freedom [7, 8, 9]. These manganites have been studied extensively for their magnetic and electronic properties in relation to the parameters like average A-site cationic radius, A-site cation size disorder, and structural distortion. These parameters influence the magnetic transitions, metal-insulator transition and charge-ordering transition [10, 11]. Moreover, the external parameters, such as the magnetic field, laser or X-ray exposure are found to induce structural, magnetic, and/or electronic phase transitions in most of the manganites. While the CMR is a property dominant in the vicinity of optimal (about 33%) divalent cation doping in $RMnO_3$ compounds, the half-doped manganite systems such as $La_{0.5}Ca_{0.5}MnO_3$, $Nd_{0.5}Ca_{0.5}MnO_3$, and $Nd_{0.5}Sr_{0.5}MnO_3$ are popular for the fascinating property of a charge- and orbital-ordering [12, 13, 14]. A phase-diagram depicting various properties of divalent cation doped manganites, *i.e.*, $R_{1-x}A_xMnO_3$, where some popular R in these series are trivalent cations La^{3+}, Pr^{3+}, Nd^{3+}, Sm^{3+}, *etc*, and the divalent cations A are Ca^{2+}, Sr^{2+} and Ba^{2+} , was constructed by Kajimoto *et. al.* [15]. This series of manganite compounds exhibits a wide variety of structural, electronic, magnetic and thermodynamic properties. Global phase-diagram of this series of compounds constructed by Kajimoto *et. al.* [15] is shown in Figure 1. While traversing from left to right in this phase-diagram, *i.e.*, from trivalent to tetravalent manganite, a ferromagnetic phase in the vicinity of optimal doping large bandwidth systems and a variety of antiferromagnetic phases such as A, CE, C, and G manifest as a function of valence state and e_g-electron bandwidth. Also, all these magnetic phases have associated electronic phases, namely, metallic, insulating and charge-ordered phases.

Our present studies concern about half-doped systems. The straight line is superimposed to mark the properties of the half-doped compounds on this phase-diagram (Figure 5.1).

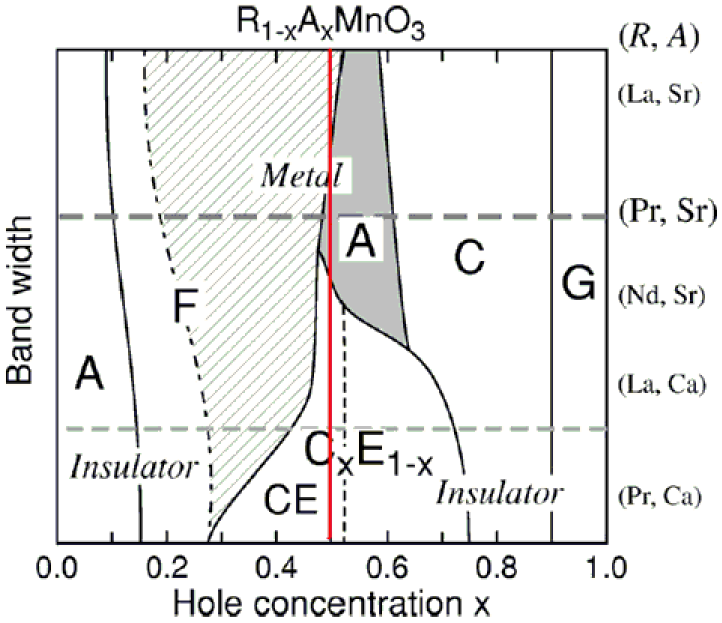

Figure 5.1: Global phase diagram of doped mixed-valent manganites, $R_{1-x}A_xMnO_3$, R = trivalent rare-earth ions, andA = divalent ions [Kajimotoet al., PRB 66 (R), 4253 (2002).

Among various systems, the half-doped $Pr_{0.5}Ca_{0.5}MnO_3$ is a CE-type antiferromagnetic charge-ordered system, in which charge-ordering can melt through a metamagnetic transition by an application of a strong magnetic field of 25 T at 4 K [16]. Interestingly, Mn-site substitution drastically reduces the critical field (*Hc*) required for the metamagnetism and induces successive sharp step-like metamagnetic transition in this system at low temperatures. The *A*-site substitution also induces similar successive sharp metamagnetic transition in the charge-ordered systems [17, 18]. Such sharp transitions are explained as a result of competing magnetic phases and electronic phase-separation. A phase-separated ground state evolves at low temperatures where ferromagnetic domains manifest within an antiferromagnetic matrix. The antiferromagnetic and ferromagnetic phases have different crystallographic structures giving rise to a strain in the phase-separated state of manganites. The lattice degrees of freedom allow the phase-separated ground state to get accommodated, albeit with a strain. An external parameter such as the magnetic field may perturb the energy balance and induce a ferromagnetic state, where the strain could play a role to influence the sharp metamagnetic transitions. The disorder also influences phase separation in the manganites. The fragility of an antiferromagnetic phase increases with disorder and may result in a glassy-state at low temperatures. It is experimentally observed that the random potential originating due to the A-site disorder entirely suppresses the long-range order and gives rise to a spin-glass state in small bandwidth systems below 50 K. Also it is known that the quenched disorder affects the long-range ordered charge-exchange (CE) state more than the ferromagnetic state. The CE-type antiferromagnetic $Pr_{0.5}Ca_{0.5}MnO_3$ has negligible A-site size disorder due to a similar size of Pr^{3+} (1.126 Å) and Ca^{2+} (1.12 Å) ions. In this case, inducing a size-disorder at A-site by substituting a different size cation and a simultaneous slight variation of the valence state is of immense interest as it had potential to reveal the unknown. The structural, magnetic, and transport properties of half-doped $Pr_{0.5-x}Ce_xCa_{0.5}MnO_3$ ($0.03 \leq x \leq 0.20$) polycrystalline compounds revealed interesting correlated structural and magnetic properties [19, 20], which were different from either trivalent cation or divalent cation doped in half-doped compounds. Also, in this case of half-doping, a

Ce-doping of up to 20% was successfully realized, while the same doping level has not achieved in optimal-doped manganite compounds. It was shown that with Ce substitution in the $Pr_{1-x}Ce_xCa_{0.5}MnO_3$ system, the structure evolves from O-type orthorhombic to a quasitetragonal symmetry. The structural and magnetic properties strongly support tetravalent or nearly tetravalent state for Ce in this system. The lower Ce substitution $x = 0.03$ and 0.05 induces sharp and strongly correlated metamagnetic and electronic transitions at low temperatures, as a result of an enhanced Mn^{3+}/Mn^{4+} ratio and large size-disorder. For higher Ce substitution $x \geq 0.1$, the system is driven to a spin-glass-like state. The $Pr_{0.4}Ce_{0.1}Ca_{0.5}MnO_3$ compound shows a spin-glass-like behavior. A detailed muon spin relaxation study revealed more about the complex magnetic structure of these compounds. On the basis of various detailed studies, a phase-diagram of half-doped $Pr_{0.5-x}Ce_xCa_{0.5}MnO_3$ ($0.03 \leq x \leq 0.20$) was constructed. In the phase-diagram shown in Figure 5.2 [from reference 20], the $Pr_{0.5-x}Ce_xCa_{0.5}MnO_3$ ($x = 0 – 0.20$) manganite system shows a clear picture of the correlation among structural, electrical and magnetic properties. The slowing down of magnetic fluctuations was observed at low levels of Ce substitution ($x = 0.05$). However, drastic transformations in the structural, magnetic and transport properties are observed at $x = 0.10$. The spin dynamics change with an increase in x. At room temperature, the structure transits from orthorhombic to quasi- tetragonal symmetry with increasing x, and concomitantly shows a transition from spin-liquid to a magnetic cluster-glass state. Also, with increasing Ce, the low-field magnetization considerably increases at low temperatures and the spin-glass transition temperature (T_G) decreases. By comparing the top and bottom panels, the phase-diagram of this system suggests a correlation between the structure and the magnetic properties of this manganite system. The orthorhombic compounds have an antiferromagnetic charge-ordered state whereas the quasi-tetragonal compounds show a rise of competing ferromagnetic interactions resulting in a glassy state. Overall, the Ce substitution is found to influence the magnetic properties strongly due to an enhanced Mn^{3+}/Mn^{4+} ratio and the cation disorder. As a result, some drastic

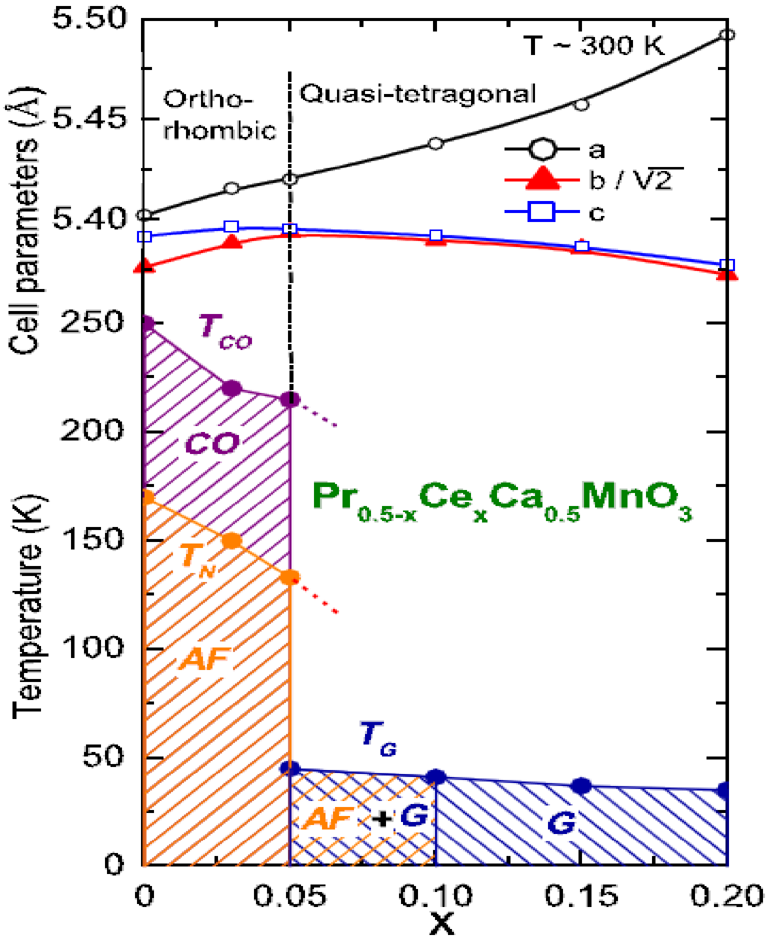

Figure 5.2: Top panel shows the variations of lattice parameters with x in $Pr_{0.5-x}Ce_xCa_{0.5}MnO_3$. A structural transition is observed from an orthorhombic to quasi-tetragonal symmetry at room temperature. The bottom panel shows the schematic phase-diagram of the $Pr_{0.5-x}Ce_xCa_{0.5}MnO_3$ ($0 \leq x \leq 0.20$) system. At low Ce substitution levels, the system exhibits an antiferromagnetic (AF) charge-ordered (CO) state, whereas a glassy state is observed for higher Ce contents. [Source of figure: reference 19]

changes take place in the structure and the spin dynamics at $x = 0.10$, which suggests a strong correlation of lattice and spin dynamics in this manganite system. Overall, the structure shows a transition from an orthorhombic to quasi-tetragonal symmetry around $x = 0.10$ at room-temperature. Low Ce substitution ($x < 0.10$) in $Pr_{0.5}Ca_{0.5}MnO_3$

weakens the antiferromagnetic charge-ordered state whereas for doping $x \geq 0.10$, a magnetic glass-like state manifests.

5.2 Motivation to Study Structural, Magnetic and Electronic Correlation in $Pr_{0.5-x}Ce_xCa_{0.5}MnO_3$ Epitaxial Thin Films

It is established from the phase-diagram of $Pr_{0.5-x}Ce_xCa_{0.5}MnO_3$ that this series of compounds exhibit interesting correlations among structural, electrical and magnetic phase transitions as a function of cerium content [20]. A cerium doping of 10% induces structural phase transition and associated electrical and magnetic phase transition – ranging from antiferromagnetic to phase-separated magnetic state to a spin-glass state. Overall, such a correlation between structure and other physical properties is not so common and, hence, subject of further research. It is known that lattice constants and, hence, the structure can be tuned by the means of strain engineering in thin film form. This provides various opportunities to observe new phases and resultant novel magnetic and electronic properties which are not accessible by any conventional means. Therefore, it is of ample interest that the epitaxial thin films of the $Pr_{0.5-x}Ce_xCa_{0.5}MnO_3$ be formed to provide extra flexibility to the structure such that occurrence of various phases in the phase diagram can be probed. Synthesis of epitaxial thin films of $Pr_{0.5-x}Ce_xCa_{0.5}MnO_3$ may be realised in two ways, namely, i) choosing substrates with suitable lattice constants such that coherent / pseudomorphic phase can be obtained. This requires that the lattice mismatch between the film and the substrate normally be less than 2%, and iii) having substrates with large lattice mismatch with the films. In this latter case, the films are only partially strained / relaxed. This is not so preferred choice as it does not lead to substantial modification of the lattice constants of the films.

In this study, we have mostly deposited coherently strained films. Now, it is important to understand whether the pseudo-cubic lattice constant of film is less or more than that of the substrate. In former case the film is said to be under tensile strain because the out-of-plane lattice constant, *i.e.* in the direction of growth, is under tension. Overall, the tensile strain results in increase in in-plane parameters and decrease in out-of-plane parameter. In the latter case, the film is under compressive strain, in which the out-of-plane parameter increases but the in-plane lattice parameters decrease. Another noteworthy point in case of *coherently* strained films is that the in-plane parameters of both the tensile and compressive strained films are same as the in-plane parameters of the substrate. This further suggests that, for coherently strained films, as the in-plane lattice constants of the film are locked with counterparts of substrate, the unit cell volume is mostly preserved by the enlargement / shrinking of the out-of-plane parameter. In view of all these properties, it may be inferred that the coherently strained films mostly form in tetragonal phase when deposited on cubic substrates.

In this study, we have deposited $Pr_{0.5-x}Ce_xCa_{0.5}MnO_3$ films under both the tensile and compressive strain. Single crystal $LaAlO_3$ *(001)* substrate with lattice constant (a) of 3.79 Å (less than '*a*' of the film) was chosen for deposition of compressive strained films, whereas $(LaAlO_3)_{0.3}(Sr_2AlTaO_6)_{0.7}$ *(001)* substrate with a = 3.87 Å (more than '*a*' of the film) was chosen for fabrication of tensile strained films.

5.3 Thin Film Synthesis of $Pr_{0.5-x}Ce_xCa_{0.5}MnO_3$ (x = 0, 0.05 and 0.10) Compounds

Bulk targets of $Pr_{0.5-x}Ce_xCa_{0.5}MnO_3$ (x = 0, 0.05 and 0.10) , of 20 *mm* diameter were prepared using solid state reaction method as described in Chapter 2. Thin films were prepared on $LaAlO_3$ *(001)* and LSAT *(001)* using PLD technique. Target to substrate distance was kept at 5 *cm* and substrate temperature was maintained at 730 ^oC. Laser was operated at 230 *mJ* energy and pulse repetition rate was 8 *Hz.* A 0.3 *mbarr* oxygen partial pressure was retained during depositions. Films were cooled to ambient temperature in 500 *mbarr* oxygen pressure.

5.4 Structural and Physical Properties of Compressive Strained $Pr_{0.5-x}Ce_xCa_{0.5}MnO_3$ (x = 0, 0.05 and 0.1) / $LaAlO_3$ *(001)* Thin Films

5.4.1 Structure

The structure was determined using XRD technique. All the $Pr_{0.5-x}Ce_xCa_{0.5}MnO_3$ (x = 0, 0.05 and 0.1) / $LaAlO_3$ *(001)* thin films were single-phase and epitaxial. Figure 5.3(a) shows 2θ versus intensity scan around *(002)* peak for all the films. For x = 0 and 0.1, there exist only one *(002)* peak though at different 2θ angles. Interestingly, the 0.05 film depicts two peaks corresponding to *(002)* reflection; it may clearly be seen that while the higher angle peak is nearly at the same position as that of *(002)* peak of x = 0 film, the lower angle peak corresponds to the structural peak of x = 0.1 thin film. This clearly suggests a structural phase transition at x = 0.05.

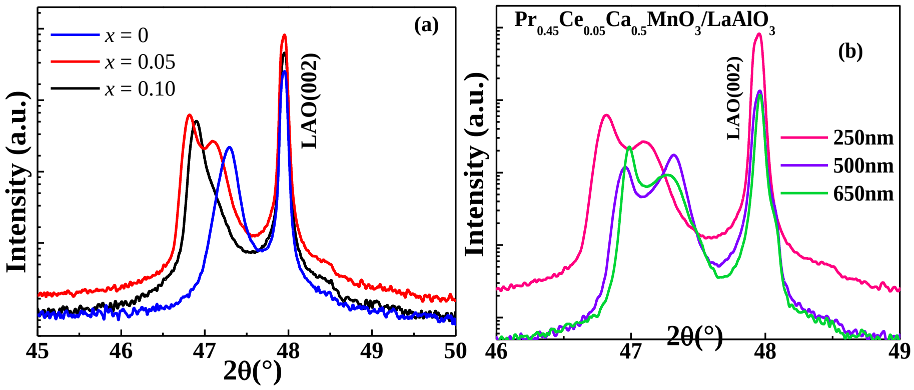

Figure 5.3: (a) Intensity versus 2θ scans around (002) peak for all the $Pr_{0.5-x}Ce_xCa_{0.5}MnO_3$ (x=0, 0.05 and 0.1) / $LaAlO_3$ (001) thin films, (b) Intensity versus 2θ scans around (002) peak for x=0.05 sample for three different thickness of the films.

It is remarkable that a structural transition in compressive strained films is so clearly evident, which is reminiscent of a similar transition in polycrystalline bulk counterparts. In view of this, a film thickness dependent study was carried out for x = 0.05. Figure 5.3(b) shows 2θ versus intensity scan magnified around *(002)* peak for 250 *nm*, 500 *nm* and 650 *nm* thin films for x = 0.05 composition. The existence of two structural peaks is clearly seen for all these films suggesting an unambiguous phase transition at *x* = 0.05 for the case of compressive strain.

It is important to obtain the information on the strain and the in-plane parameters of the films. We recorded the reciprocal space maps (RSM) around asymmetric *(301)* peak for all the films, as shown in Figure 5.4. The most important observation from these data is the existence of coherent compressive strain in all the films. It is clearly seen that the film peak lies in the same pseudomorphic line as the substrate. This suggests that the in-plane parameters of the film are same as that of the substrate – an attribute of coherently strained films. Another observation is the evolution of two peaks for *x* = 0.05 film and stabilization of the lower angle peak for *x* = 0.1 thin film. As mentioned in previous paragraph, this is a structural transition at *x* = 0.05 is an intrinsic property of the material, and the RSMs further strengthen our assertion that this transition exists under coherent compressive strain.

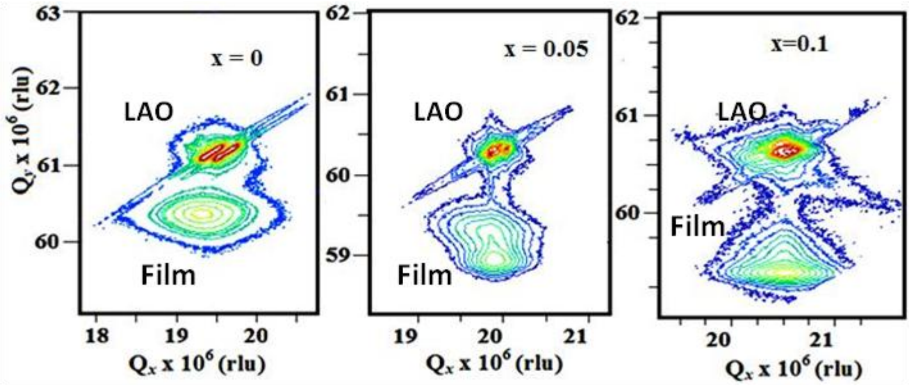

Figure 5.4: Reciprocal space maps around (301) asymmetric peak for the $Pr_{0.5-x}Ce_xCa_{0.5}MnO_3$ (x=0, 0.05 and 0.1) / $LaAlO_3$ (001) thin films with a thickness of 250 nm.

The RSMs were also acquired for other films with thicknesses 500 *nm* and 650 *nm* (*x* = 0.05), as shown in Figure 5.5. These data depict two dominant features, namely, i) the existence of coherent compressive strain and, ii) two peaks for *(002)* depicting a structural transition. While the in-plane parameter for all these coherently strained films is 3.79 Å which is same as that of substrate, the out-of-plane parameter for corresponding to two peaks is 3.83 Å and 3.85 Å.

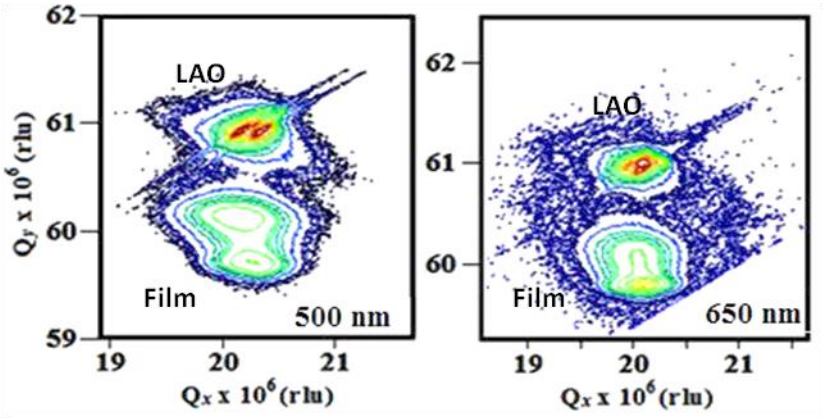

Figure 5.5: Reciprocal space maps around (301) asymmetric peak for the $Pr_{0.5-x}Ce_xCa_{0.5}MnO_3$ (x= 0.05) 500 and 650 nm thick films deposited on $LaAlO_3$ (001).

5.4.2 Magnetic Properties

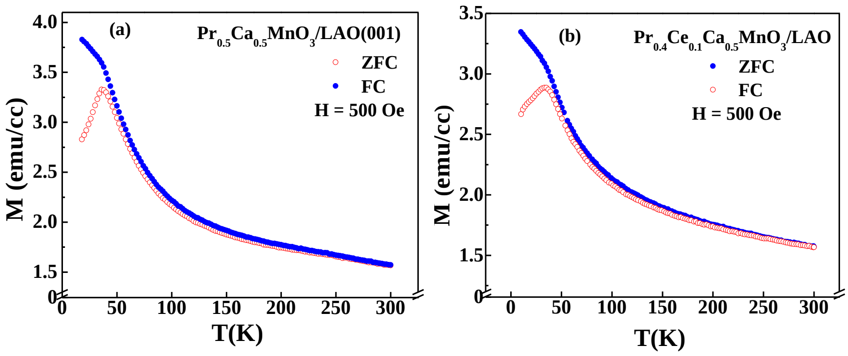

Figure 5.6: ZFC and FC magnetization versus temperature for $Pr_{0.5-x}Ce_xCa_{0.5}MnO_3$ (x=0 and 0.1) / $LaAlO_3$ (001) thin films.

Magnetization (M) as a function of temperature was measured in zero-field-cooled (ZFC) and field-cooled (FC) protocols in an applied magnetic field of 500 Oe for $Pr_{0.5-x}Ce_xCa_{0.5}MnO_3$ (x = 0, 0.05 and 0.1) / $LaAlO_3$ *(001)* thin films (250 *nm*). These data are plotted in Figure 5.6. As it is evident and expected, there is no ferromagnetic transition for any thin film. However, there is a discernible bifurcation of ZFC and FC magnetization at ~35 *K*. This indicates formation of weak cluster-glass like behaviour, which matches with the behaviour of their bulk counterparts. Physical properties of charge-ordered manganites are very sensitive to composition, defects, lattice constants, oxygen content, *etc*. In the present case of thin films, one or more of these aspects (primarily, the deviation in lattice constant from that of the bulk) may result in cluster-glass like behaviour at low temperatures.

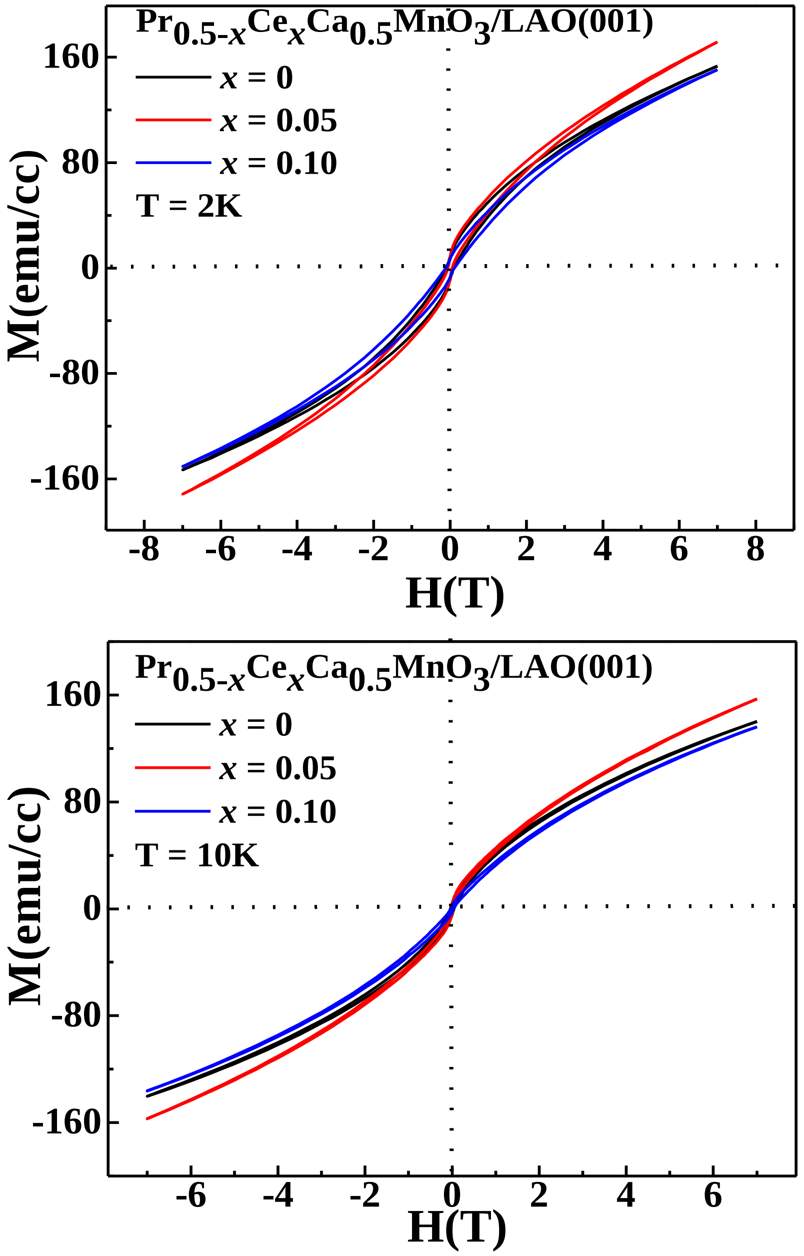

Figure 5.7: Magnetization versus magnetic field isotherms at (a) 2 K and (b) 10 K for $Pr_{0.5-x}Ce_xCa_{0.5}MnO_3$ (x=0, 0.05 and 0.1) / $LaAlO_3$ (001) thin films (250 nm).

To further explore the magnetic properties of all these films, the magnetization versus magnetic field isotherms were acquired at temperatures on 2 *K* and 10 *K*, as plotted in Figure 5.7. All the samples show an unsaturated ferromagnetic hysteresis loop with a very low magnetic moment in the range of about 0.6-0.7$\mu_B/f.u.$ This suggests nearly long-range antiferromagnetic (AFM) order with interspersed ferromagnetic (FM) clusters, which is a clear signature of phase-separated state for all the films. Also, the difference in magnetic moment of the three films is not so significant. This suggests that a Ce-doping of up to 10% does not induce sufficient changes in the ground-state magnetic properties. One of the reasons of such behaviour may be contemplated as the robust AFM charge-ordered state which melts to FM metallic state in a field of up to 25 *Tesla*. It requires large chemical or physical modification either for lowering the field to induce the long-range FM order or complete transformation to a ground state FM order. We will revisit the discussions on the magnetic state of these and some more films at later stage, after discussions about electrical properties.

5.4.3 Electrical Properties

Electrical properties of all the films were studied by measuring both the temperature-dependent and the magnetic field dependent resistivity. Figure 5.8 shows electrical resistivity as a function of

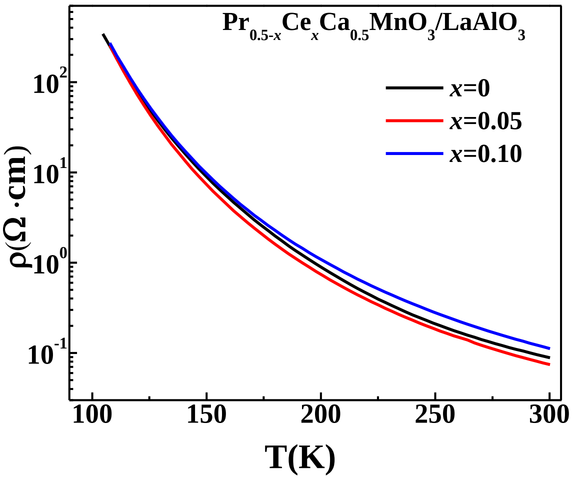

Figure 5.8: Resistivity as a function of temperature for $Pr_{0.5-x}Ce_xCa_{0.5}MnO_3$ (x=0, 0.05 and 0.1) / $LaAlO_3$ (001) thin films.

temperature. It is seen that all the films exhibit highly resistive behaviour, a typical property of the low-bandwidth charge-ordered manganites. The resistivity of these films increases sharply with decreasing temperature and exceeds the measurement range of the instrument; hence, the low temperature data could not be recorded.

Figure 5.9 shows the resistivity versus magnetic-field isotherms for all the films. It is clear that the resistance is decreasing with increasing magnetic field, suggesting a negative MR which is in the range of 20-30 % for these thin films. Though a robust AFM charge-ordered system without melting should not yield this large MR, formation of FM clusters in the major AFM matrix can result in some MR due to Zener-double-exchange in these sporadically interspersed FM clusters.

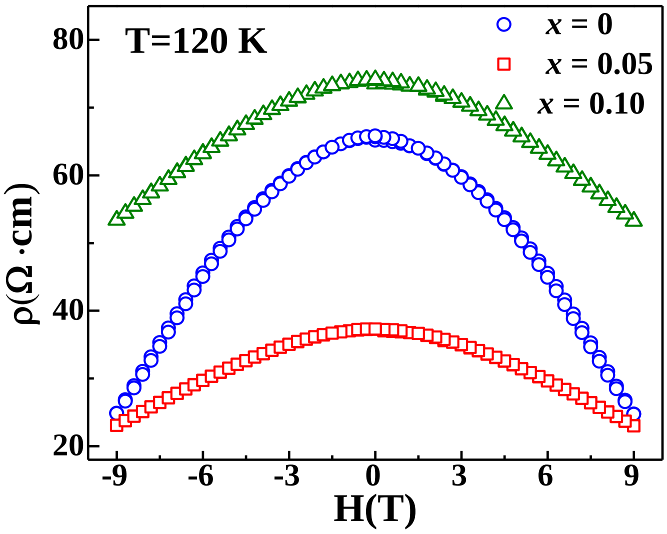

Figure 5.9: Resistivity versus magnetic field isotherms for $Pr_{0.5-x}Ce_xCa_{0.5}MnO_3$ ***(x=0, 0.05 and 0.1) /*** $LaAlO_3$ ***(001) thin films.***

Here, one can draw a correlation between the magnetic field dependent magnetization data (Figure 5.7) and the MR. Occurrence of FM clusters in major AFM matrix is simultaneous to induction of metallic clusters in major insulating matrix. Hence, a very low MR has direct relation with the weak FM order in these films.

5.5 Searching for Metamagnetism in $Pr_{0.5-x}Ce_xCa_{0.5}MnO_3$ (x=0.05)/$LaAlO_3$ *(001)* Thin Films

The occurrence of metamagnetism, and in particular a sharp step-like metamagnetism at low temperatures, *i.e.*, magnetic-field induced transition of AFM to FM and charge-ordered insulating to metallic transitions in a sharp step-like behaviour with a magnetic-field step of as small as 50 *Oe* in the transition region, triggered a lot of interest among scientists for primary reason of understanding fundamental physics leading to such exotic transitions. Initially, the sharp metamagnetic transitions were found to occur when Mn-site was diluted charge-ordered manganite. The reason behind such behaviour was understood in terms of formation of FM cluster in the AFM matrix by the magnetic/non-magnetic dopants at Mn-site. Later, it was shown by other groups that this property is not only a feature of Mn-site diluted charge-ordered manganites, but also of the manganites with large A-site cation disorder. Overall, a consensus was established that sharp metamagnetic steps occur in phase-separated charge-ordered manganites when a minor FM phase in the major AFM matrix may be induced either by Mn-site doping or by A-site cation disorder. Other observations of such phase-separated systems were simultaneous to the occurrence of field-induced sharp step-like transitions in the electrical resistivity and heat capacity, thus, indicating strong correlations and a determinant role of structure.

The present $Pr_{0.5-x}Ce_xCa_{0.5}MnO_3$ (x= 0.05)/$LaAlO_3$ *(001)* thin films under study have all the attributes of exhibiting ultra-sharp metamagnetic transitions, as the A-site of $Pr_{0.5}Ca_{0.5}MnO_3$ has been diluted by Ce-doping which induced large size-disorder at A-site. Some compositions of this series are known to exhibit metamagnetic transition in the bulk compounds. However, it is also known that slight structural deviations might induce major alterations in the physical properties of such manganites. Hence, it is interesting to explore the occurrence of metamagnetic transitions in the coherently compressive strained thin film of these compounds. In the bulk compounds, the *x*=0.05 sample, which is at the critical state of structural transition as *x* varies, exhibits the most pronounced metamagnetic transitions. Thus, we also chose *x* = 0.05 thin films of different thicknesses (250 *nm*, 500 *nm* and 650 *nm*) for studying the metamagnetic transitions. Figure 5.10 shows the magnetization versus field isotherms of all *x* = 0.05 thin films at T = 2 *K* and 10 *K*.

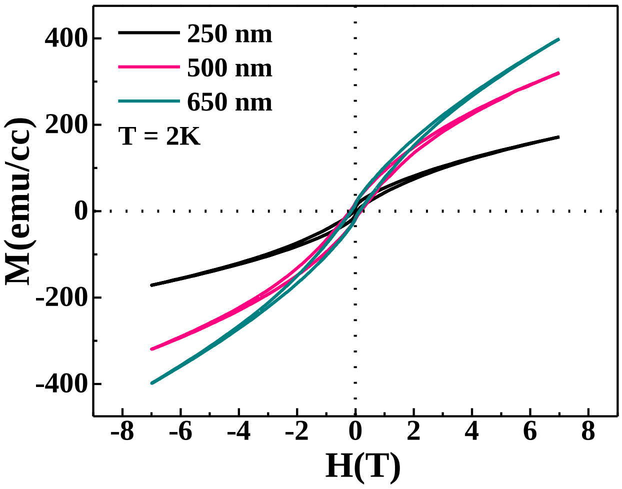

Figure 5.10: Magnetization versus magnetic field isotherms at 2 K for $Pr_{0.5-x}Ce_xCa_{0.5}MnO_3$ /LAO(001)(x= 0.05) 250, 500 and 650 nm thick films.

Magnetic hystereses with week saturation FM moment indicate the phase-separated state of these films. It may be noted that the FM moment increases with increasing thin film thickness. However, there is no discernible step-like metamagnetic transition in these thin film samples. To explore it further, the first-quadrant magnetization was magnified and plotted in Figure 5.11. Though small, yet authentic and reproducible step-like metamagnetic transitions were observed for 500 and 250 *nm* thin films. Till date, the occurrence of such metamagnetic transitions in coherently strained epitaxial films has eluded the scientists around the world. Lack of sharp step-like metamagnetic transitions was attributed to the structural modification induced by the strain. However, the present study suggests that it is important to choose i) coherently strained films and ii) the compressive strains, as conducive attributes for inducing the metamagnetic transitions.

Overall, these studies suggest that the metamagnetism is not only the property of bulk-like systems but of coherently strained epitaxial thin films as well. However, in case of thin films, the antiferromagnetic charge-ordered state is more stable as compared to bulk samples. Therefore, the metamagnetic transitions induce smaller changes in the magnetization.

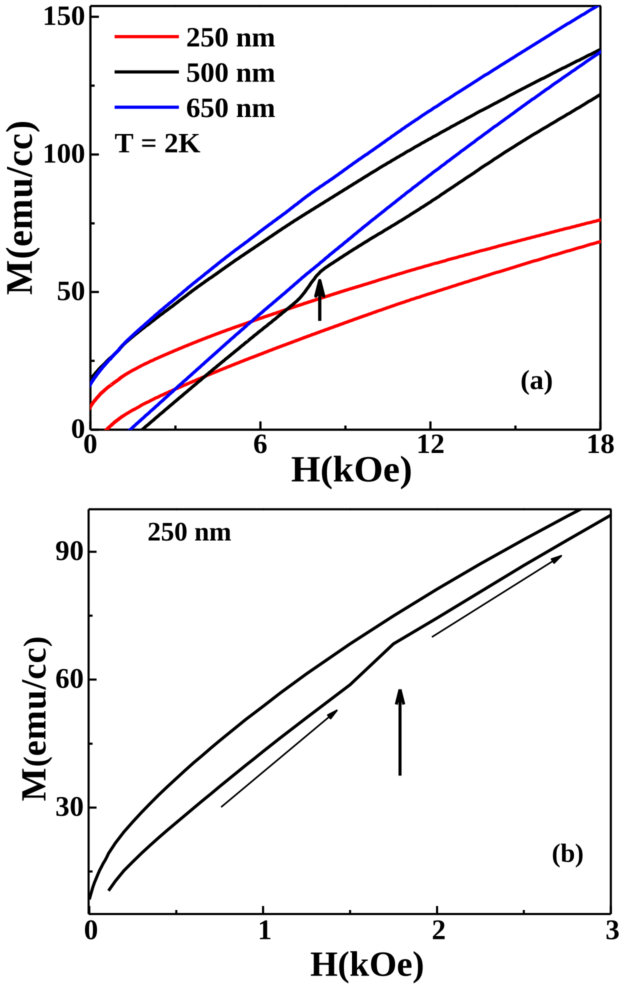

Figure 5.11: Magnetization versus magnetic field isotherms at 2 K for $Pr_{0.5-x}Ce_xCa_{0.5}MnO_3$ /LAO(001) (x= 0.05) 250, 500 and 650 nm thick films. Arrow in both the panels indicates the occurrence of a sharp metamagnetic step for a 500 nm and a 250 nm films.

5.6 Structural and Physical Properties of Tensile Strained $Pr_{0.5-x}Ce_xCa_{0.5}MnO_3$ (x=0, 0.05 and 0.1) / LSAT (001) Thin Films

5.6.1 Structure

The structure as determined using XRD technique suggests that all the $Pr_{0.5-x}Ce_xCa_{0.5}MnO_3$ (x=0, 0.05 and 0.1) / LSAT *(001)* thin films are single-phase and epitaxial. In this case, the lattice constant of film is less than that of the LSAT substrate, the films are said to be under tensile strain. Figure 5.12 shows 2θ versus intensity scan around *(002)* peak for these films. For x = 0 and 0.05, there exist only one *(002)* peak, however, at different 2θ angles, the x = 0.1 film depicts two *(002)* peaks corresponding to the peak position of x = 0 and 0.05. This trend is surprising as the structural phase transition that we observed for compressive strained films on $LaAlO_3$ is not smooth in this case. While there is clear difference in peak positions of x = 0 and 0.05 thin films, there is occurrence of both these phases in x = 0.1 film. This behaviour of x = 0.05 and 0.1 thin films has the reverse trend in case of compressive strained film.

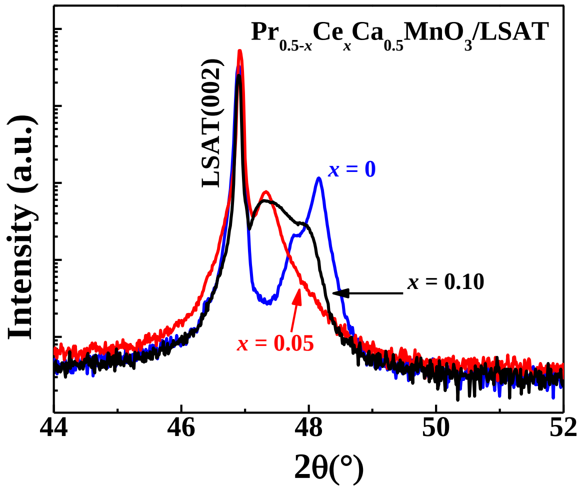

Figure 5.12: Intensity versus 2θ scans around (002) peak for all the $Pr_{0.5-x}Ce_xCa_{0.5}MnO_3$ (x=0, 0.05 and 0.1) / LSAT (001) thin films.

To explore it further, we deposited another thin film with slightly different thickness. Figure 5.13 shows 2θ versus intensity Surprisingly, both these films have different 2θ positions. To resolve this behaviour and to obtain the information on the strain and the in-plane parameters of the films, RSM around asymmetric *(301)* peak were recorded for all the films, as shown in Figure 5.14.

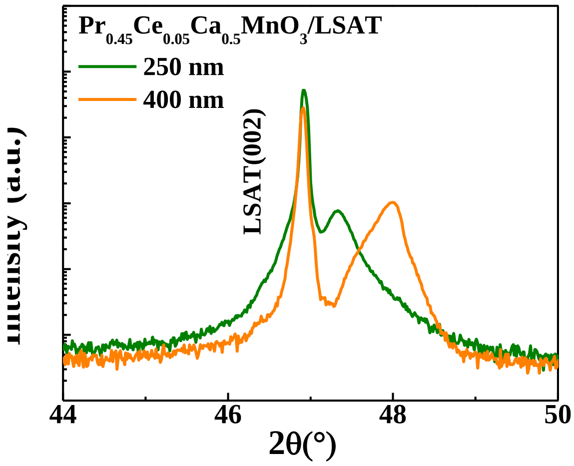

Figure 5.13: Intensity versus 2θ scans around (002) peak for x=0.05 sample for two films on LSAT substrate with different thickness.

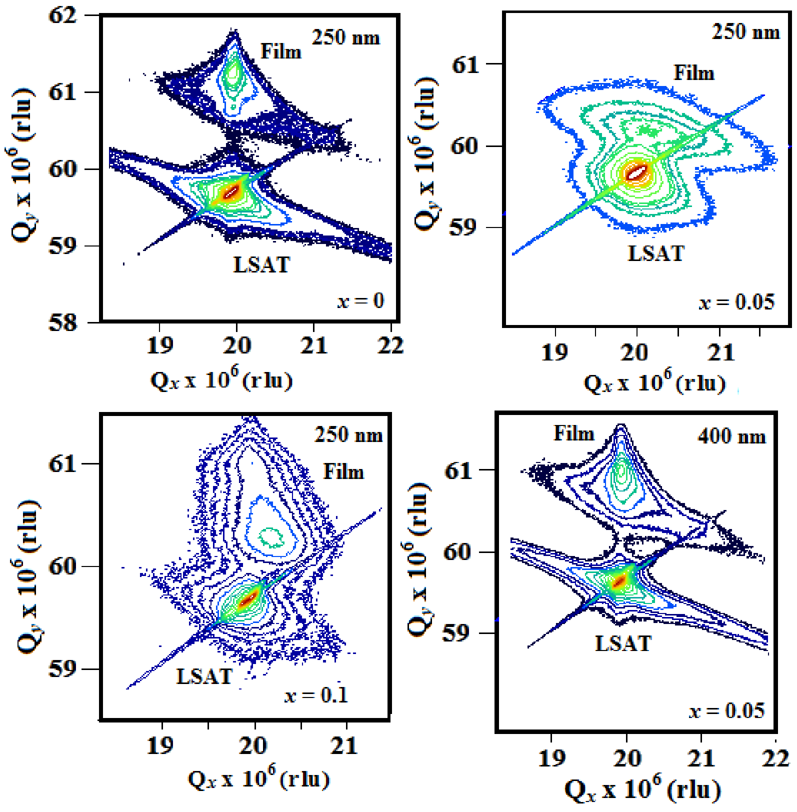

Figure 5.14: Reciprocal space maps around (301) asymmetric peak for 250 nm thick $Pr_{0.5-x}Ce_xCa_{0.5}MnO_3$ (x=0, 0.05 and 0.1) / LSAT (001) thin films. Figure also shows RSM for another thickness of 400 nm of x= 0.05 film.

The most important observation from these data is the existence of coherent tensile strain in all the films but not for 250 *nm* thick x = 0.05 film. Except for this film, the film peak of all other samples lies in the same pseudomorphic line as the substrate, which suggests formation coherently tensile strained films (Figure 5.14). It is noteworthy that structural phase transition which is indicated by occurrence of twin *(002)* peaks occurs at x = 0.1 in this series with tensile strain, indicating that the structure gets modified to shift this transition under the influence of tensile strain. A similar transition, in case of compressive strained films of $LaAlO_3$ substrates, occurred as x = 0.05. Also in case of tensile strained films on LSAT substrate for x = 0.1, the *(002)* peaks do not lie on the pseudomorphic line which suggests a partial strained film. Overall, these RSMs depict the following about the tensile strained films. The x = 0 and 0.05 films possess same structure and they are coherently strained. For x = 0.05 composition, both coherently- and partially-strained films were obtained by varying thickness. x = 0.1 films shows two peaks suggestive of structural phase transition. While the in-plane parameter for all these coherently strained films is 3.87 Å which is same as that of substrate, the out-of-plane parameter corresponding to two peaks is 3.78 Å. The relaxed x = 0.05 films has out-of-plane parameter of 3.82 Å and in-plane parameter of 3.84 Å.

5.6.2 Magnetic Properties

The ZFC and FC magnetization as a function of temperature was measured in an applied magnetic field of 500 *Oe* for all the $Pr_{0.5-x}Ce_xCa_{0.5}MnO_3$ (x=0, 0.05 and 0.1) / LSAT *(001)* thin films. These data for x = 0 and 0.1 are plotted in Figure 5.15. There seems no ferromagnetic transition for any thin film. However, an onset of a significant bifurcation of ZFC and FC magnetization at ~35 K indicates formation of weak cluster-glass like behaviour. This behaviour agrees well with those of the compressive strained films and of their bulk counterparts.

Figure 5.16 shows the magnetization versus magnetic field isotherms at temperatures 2 *K* and 10 *K*. All the samples show an unsaturated ferromagnetic hysteresis loop very low magnetic moment in the vicinity of 1μ_B/*f.u.* This suggests nearly long-range antiferromagnetic (AFM) order with interspersed ferromagnetic (FM) clusters, which is clear signature of phase-separated state for all the samples. Here, the difference in magnetic moment of x = 0.1 film and all other films is discernible. Overall, the magnetic properties of tensile strained films are not so significantly different from the compressive strained films.

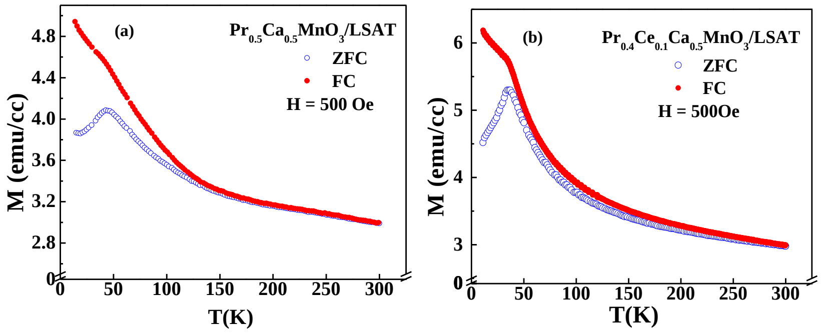

Figure 5.15: Zero-field-cooled (ZFC) and field-cooled (FC) magnetization (M) versus temperature for $Pr_{0.5-x}Ce_xCa_{0.5}MnO_3$ (x=0 and 0.1) / LSAT (001) thin films.

5.7 Searching for Metamagnetism in $Pr_{0.5-x}Ce_xCa_{0.5}MnO_3$ (x= 0.05)/LSAT (001) Thin Films

As mentioned in detail in the section of the compressive strained films, the x = 0.05 film is the most potential composition to exploring the metamagnetic transitions. In case of these tensile strained films on LSAT *(001)* substrate too, we explored in the detail possibility of occurrence of metamagnetic transitions in 250 *nm* and 400 *nm* thick x = 0.05 thin films. Figure 5.17 shows the magnetization versus field isotherms of these two films at T = 2 *K*. It is clearly seen that the FM content increases with increasing thickness; the magnetic moment of 400 *nm* thin film is substantially larger than that of the 250 *nm* film. This may be attributed to the enhanced tendency of the formation of large size FM cluster as larger thickness may enhance the cluster growth in third dimension of thickness. A careful investigation of these

M-H loops did not reveal any step-like feature in the magnetization. Hence, we may conclude the tensile strained films do not have tendency for the occurrence of metamagnetism in spite of higher magnetic moment achieved.

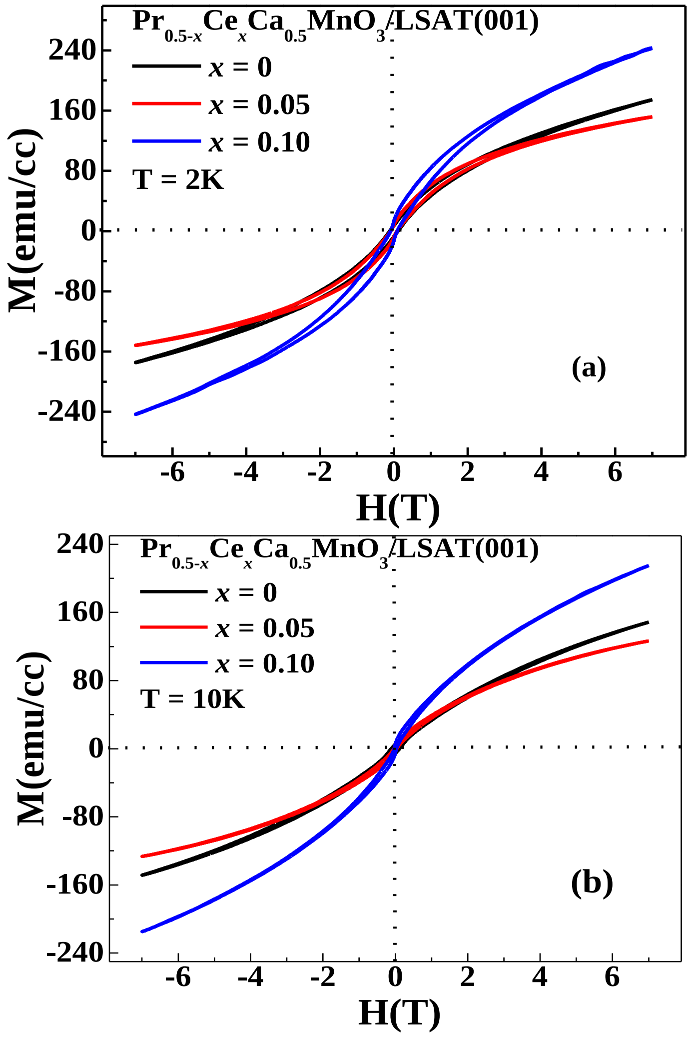

Figure 5.16: Magnetization versus magnetic field isotherms at 2 K and 10 K for $Pr_{0.5-x}Ce_xCa_{0.5}MnO_3$ (x=0, 0.05 and 0.1) / LSAT (001) thin films.

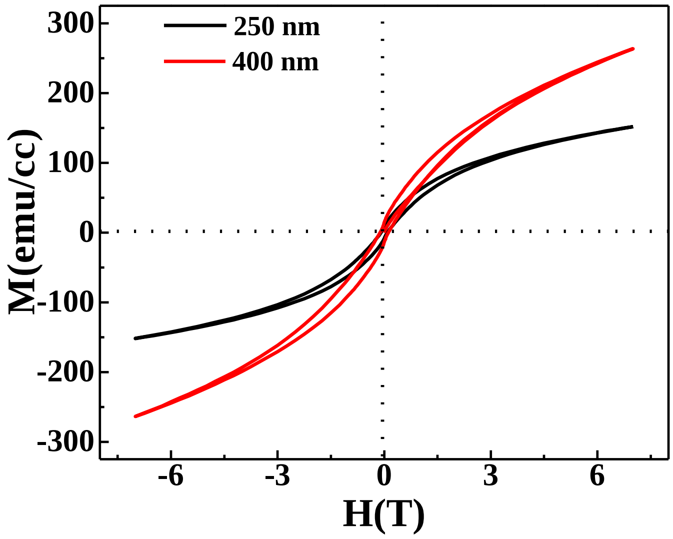

Figure5.17: Magnetization versus magnetic field isotherms at 2 K for $Pr_{0.5-x}Ce_xCa_{0.5}MnO_3$ /LSAT(001)(x= 0.05) 250 and 400 nm thick films.

5.8 Conclusions

One of the very important outcomes of the studies of $Pr_{0.5-x}Ce_xCa_{0.5}MnO_3$ (x=0, 0.05 and 0.1) thin films is the successful growth of coherently strained compressive and tensile strained films of thickness as large as 500 *nm*. Though there are quite a few similarities in two types of films, there are enough disparities which show the richness of physics that this class of charge-ordered manganites continue to reveal. Among similarities are the, i) coherent growth of thin films of all compositions up to a thickness of 500 *nm* under both compressive and tensile strain, ii) weak magnetic moment, iii) cluster-glass like behaviour, and iv) structural transition in films as a function of Ce-doping. There are few marked differences too, namely, i) the structural transition for compressive strained films occurs at x = 0.05 while for tensile strained films it occurs at x = 0.1, showing influence of strain, ii) tensile strained films exhibiting larger magnetic moment compared to the compressive strained films, iii) films of all the compositions for compressive strain grow coherently, whereas the higher Ce-doping compositions with tensile strain tend to get partially-strained, iv) the fascinating properties of metamagnetism is exhibited by compressive strained films, while tensile strain tend to suppress, despite inducing larger magnetic moment.

Overall, we would like to conclude that the structural and magnetic properties of compressive and tensile coherently strained $Pr_{0.5-x}Ce_xCa_{0.5}MnO_3$ (x=0, 0.05 and 0.1) thin films were studied. Both type of films exhibit structural transition while the metamagnetism is exhibited only by the compressive strained films.

References:

1. Baibich M. N. *et al* (1988), Giant Magnetoresistance of (001)Fe/(001)Cr Magnetic Superlattices, Phys. Rev. Lett., 61, 2472.
2. Binasch G. *et al* (1989), Enhanced magnetoresistance in layered magnetic structures with antiferromagnetic interlayer exchange, Phys. Rev. B, 39(7), 4828 (doi:10.1103/PhysRevB.39.4828).
3. Helmolt R. V. *et al* (1993), Giant negative magnetoresistance in perovskitelike, Phys. Rev. Lett., 71, 2331(doi/10.1103/PhysRevLett.71.2331).
4. Chahara K., *et al* (1993), Magnetoresistance in magnetic manganese oxide with intrinsic antiferromagnetic spin structure, Appl. Phys. Lett., 63, 1990 (doi.org/10.1063/1.110624).
5. Haghiri-Gosnet A. M., Renard J. P. (2003), CMR manganites: physics, thin films and devices, J. Phys. D: Appl. Phys., 36, R127–R150 (stacks.iop.org/JPhysD/36/R127).
6. Rao C. N. R. (2000), Charge, Spin, and Orbital Ordering in the Perovskite Manganates, $Ln_{1-x}A_xMnO_3$ (Ln = Rare Earth, A = Ca or Sr), J. Phys. Chem. B, 104, 5877 (doi/abs/10.1021/jp0004866).
7. Rao C. N. R., Cheetham A. K. (1997), Giant Magnetoresistance, Charge-Ordering, and Related Aspects of Manganates and Other Oxide Systems, Adv. Mater., 9, 1009 (DOI: 10.1002/adma.19970091304).

8. Tokura Y. *et al* (1996), Origins of colossal magnetoresistance in perovskitetype manganese oxides, J. Appl. Phys., 79, 5288 (doi: 10.1063/1.361353).
9. Motome Y. *et al* (2003), Competing orders and disorder-induced insulator to metal transition in manganites, Phys. Rev. Lett., 91,167204-1(doi: 10.1103/PhysRevLett.91.167204).
10. Rodriguez-Martinez L. M., Attfield J. P. (1996), Cation disorder and size effects in magnetoresistive manganese oxide perovskites, Phys. Rev. B, 54, R15622 (doi/10.1103/PhysRevB.54.R15622).
11. Rodriguez-Martinez L. M., Attfield J. P. (1998), Cation disorder and the metal-insulator transition temperature in manganese oxide perovskites, Phys. Rev. B, 58, 2426 (doi/10.1103/PhysRevB.58.2426).
12. Jin S. *et al* (1995), Thickness dependence of magnetoresistance in La–Ca–Mn–Oepitaxial films, Appl. Phys. Lett., 67, 557 (doi.org/10.1063/1.115168).
13. Liu, K. et al (1996), Charge ordering and magnetoresistance in Nd1-xCaxMnO3 due to reduced double exchange, Phys. Rev. B, 54, 3007 (doi/10.1103/PhysRevB.54.3007).
14. Kuwahara, H. et al (1995), A First-Order Phase Transition Induced by a Magnetic Field, Science, 270, 961 (doi: 10.1126/science.270.5238.961).
15. Kajimotoet et al (2002), Stripe-type charge ordering in the metallic A-type antiferromagnet Pr0.5Sr0.5 MnO3, Phys. Rev. B, 66 (R), 4253.
16. Tokunaga M. et al (1998), High-magnetic-field study of the phase transitions of R1-xCax MnO3 (R= Pr, Nd), Phys. Rev. B, 57, 5259 (doi/10.1103/PhysRevB.57.5259).
17. Hardy V. et al (2003), Staircase effect in metamagnetic transitions of charge and orbitallyorderedmanganites, J. Magn. Magn. Mater. 264, 183 (doi:10.1016/S0304-8853(03)00201-4).
18. Woodward F. M. et al (2004), Field-induced avalanche to the ferromagnetic state in the phase-separated ground state of

manganites, Phys. Rev. B, 70, 174433 (doi: 10.1103/PhysRevB.70.174433).

19. Mavani K. R., Paulose P. L. (2005), Influence of Ce substitution on structure, magnetism, and transport in $Pr_{0.5-x}Ce_xCa_{0.5}MnO_3$ ($0.03 \leq x \leq 0.20$): From metamagnetism to a spin-glass state, Phys. Rev. B, 72, 104421 (DOI: 10.1103/PhysRevB.72.104421).
20. Mavani K. R. *et al* (2012), Spin dynamics of $(Pr_{0.5-x}Ce_x)Ca_{0.5}MnO_3$ (x=0.05, 0.10, and 0.20) system studied by muon spin relaxation, J. Appl. Phys., 112, 073911 (doi: 10.1063/1.4754848).
21. Srivastava M. K *et al* (2013), Impact of strain on metamagnetic transitions in $Sm_{0.5}Sr_{0.5}MnO_3$ thin films, Appl. Phys. Lett. 102, 032402 (doi: 10.1063/1.4788745).
22. Srivastava M. K *et al* (2013), Comparative study of magnetic and magnetotransport properties of $Sm_{0.55}Sr_{0.45}MnO_3$ thin films grown on different substrates AIP Adv., 3, 052118 (doi: 10.1063/1.4805077).

~ End of Chapter 5 ~